1-1-2011

Applications Of Electronic Structure Theory To Problems In Unimolecular Dissociation And Inorganic And Biochemical Systems

Jia Zhou
Wayne State University

APPLICATIONS OF ELECTRONIC STRUCTURE THEORY TO PROBLEMS IN UNIMOLECULAR DISSOCIATION AND INORGANIC AND BIOCHEMICAL SYSTEMS

by

JIA ZHOU

DISSERTATION

Submitted to the Graduate School

of Wayne State University,

Detroit, Michigan

in partial fulfillment of the requirements

for the degree of

DOCTOR OF PHILOSOPHY

2011

MAJOR: CHEMISTRY (Physical)

Approved by:

_____

Advisor Date

_____

_____

_____

DEDICATION

To my parents, for always being there and supporting me in my entire endeavor. Without their love, advice, and support, none of this work would have been possible.

ACKNOWLEDGMENTS

There are a lot of people I would like to take this opportunity to acknowledge. This dissertation could not have been completed without their help and support.

First, I would like to thank my advisor, Professor H. B. Schlegel for his guidance, encouragement and patience during my entire graduate study.

Thanks are due to the members of my dissertation committee: Professor Andrés G. Cisneros, Professor Charles H. Winter, Professor Arthur Suits and Professor Caroline Morgan for their making my thesis research stronger by sharing their thoughtful comments and insightful questions during my five years at Wayne State University.

I am very grateful to my co-workers, Dr. Jason. L. Sonnenberg, Dr. Peng. Tao, Dr. Barbara. H. Munk, Dr. Suk Kyoung Lee, Dr. Richard Lord, Jason. A. Sonk, Brian. T. Psciuk, Adam. Birkholz, and Michael A. Cato for their support and assistance.

Melissa Barton, Mary Wood, Erin Scully, Nestor Ocampo, and Debbie McCreless are also gratefully acknowledged for all their help. Special thanks are also owed to my friends for their wonderful friendship.

Financial support during my graduate studies, provided by National Science Foundation, Department of Chemistry, and Wayne State University is always gratefully acknowledged.

TABLE OF CONTENTS

LIST OF TABLES

LIST OF FIGURES

LIST OF SCHEMES

CHAPTER 1

INTRODUCTION AND DISSERTATION OVERVIEW

Computational chemistry is a branch of chemistry which combines concepts from physics and mathematics in order to assist in solving chemical problems. With recent advances in computer engineering and software technology, this field has grown from the study of a few small molecules to much larger systems such as clusters, nanotubes, and biomolecules. Theoretical calculations are often used to help understand the details of chemical reactions and molecular properties that are difficult to study in the experiments. Therefore, computational chemistry is becoming more and more useful and widespread. Close collaborations between experimental chemists and theoreticians are becoming very common.

Potential energy surface (PES) plays an important role in computational chemistry.[1,2] Reaction energies and barriers can be obtained by locating the minima and transition states on the potential energy surface. The calculation of accurate energetics often requires high levels of theory, which sometimes can be too expensive to be practical. Some well-defined compound methods, such as G4,[3] W1U,[4] and CBS-APNO,[5] have been developed to achieve higher accuracy but with lower cost. However, for even larger systems, such as materials and biomolecules, molecular orbital (MO) methods become extremely expensive. New methodology which integrates molecular mechanics (MM) methods and quantum mechanics (QM), namely QM/MM, uses the strength of both methods and make it possible to study such a system.[6-8] These advances all have

provided a way to explore the mechanisms of chemical reactions at the molecular level.

Beyond searching for stationary points on the potential energy surface is modeling chemical kinetics and dynamics. Transition state theory has established a relationship between kinetics and the energetics and structures of the stationary points.[9,10] RRKM theory is a more detailed statistical method, and can be applied to a large variety of chemical reactions, particularly unimolecular reactions, to predict reaction rates and branching ratios.[10,11] However, this method can be a good approximation under certain assumptions, such as rapid redistribution of the available vibrational energy for RRKM. Recently, more and more reactions have been observed to break the traditional rules, such as the non-statistical unimolecular dissociation of acetone radical cation[12-15] and the "roaming" mechanism[16-22]. To study these kind of reactions, accurate simulation of reaction dynamics are needed.

Traditional classical trajectory calculations for chemical reactions were carried out primarily on analytical surfaces.[23-25] These surfaces are generally fitted to experimental or theoretical data. This makes the treatments limited to small systems and special to each system. However, with the advances in computer technology and theory improvements, it has become practical to compute classical trajectories directly from *ab initio* electronic structure calculations.

There are two approaches for *ab initio* molecular dynamics: extended Lagrangian and Born-Oppenheimer (BO). In the extended Lagrangian molecular

dynamics method, both nuclei and the wave function are propagated by the appropriate equations of motion. In the BO molecular dynamics, the wave function is converged at every step and the nuclei are propagated classically.[26] In the present work, the Hessian based predictor-corrector method, developed by Schlegel and co-workers,[27,28] is used to integrate the *ab initio* classical trajectory. This method enables the integration of trajectories with a much larger step size compared to the traditional Verlet algorithm. The trajectories are terminated when certain criteria are met. Once the trajectories are completed, the analysis of the final products can be carried out.

The research covered in this thesis is as follows:

In Chapter 2, the non-statistical dissociation of acetone radical cation has been studied by *ab initio* direct classical trajectory calculations at the MP2/6-31G(d) level of theory.[29] A bond additivity correction has been used to improve the MP2 potential energy surface (BAC-MP2). The energy dependence of the branching ratio, dissociation kinetics, and translational energy distribution for the two types of methyl groups have been investigated using a microcanonical ensemble and specific mode excitation. In each case, the dissociation favors the loss of the newly formed methyl group, in agreement with the experiments. For the microcanonical ensemble, the branching ratios for methyl loss are calculated to be 1.43, 1.88, 1.70, and 1.50 for 1, 2, 10, and 18 kcal/mol of excess energy, respectively. The energy dependence of the branching ratio is seen more dramatically in the excitation of individual modes involving C-C-O bending. For modes 3 and 6, the branching ratio rises to 1.6 and 1.8-2.3 when 1 or 2 kcal/mol

are added, respectively, but falls off when more energy is added. For mode 8, the branching ratio continues to rise monotonically from 1.5 to 2.76 when 1 to 8 kcal/mol of excess energy are added.

The dissociation of pentane-2,4-dione radical cation studied by *ab initio* direct classical trajectory calculations at the MP2/6-31G(d) level of theory is presented in Chapter 3.[30] A bond additivity correction has been used to improve the MP2 potential energy surface (BAC-MP2). A microcanonical ensemble using quasiclassical normal mode sampling was constructed by distributing 10 kcal/mol of excess energy above ZPE for the transition state for the tautomerization of the enol with a terminal double bond, 4-hydroxypent-4-en-2-one radical cation, to the diketo form. A total of 244 trajectories were run starting from this transition state, yielding pentane-2,4-dione radical cation and depositing energy in the terminal CC bond. As a result, the branching ratio for dissociation of the terminal CC bond versus the interior CC bonds is significantly larger than expected from RRKM theory. The branching ratio for the dissociation of the two interior CC bonds is ca 20:1, with the one closest to the activated methyl breaking more often. Since the two interior bonds are equivalent and should dissociate with equal probability, this branching ratio represents a very large deviation from statistical behavior. A simple kinetic scheme has been constructed to model the dissociation rates. The non-statistical behavior is seen because the rate of energy flow within the molecule is comparable to or slower than the rates of dissociation for the activated system. In addition to the expected dissociation products, some of the trajectories also

lead to the formation of an ester-like product, prop-1-en-2-yl acetate radical cation.

The research in Chapter 4 is the dissociation of 1,3-cyclobutanedione radical cation, which was studied by *ab initio* direct classical trajectory calculations at the BH&HLYP/6-31G(d) level of theory. A microcanonical ensemble using quasiclassical normal mode sampling was constructed by distributing 10 kcal/mol of excess energy above the transition state for the tautomerization of the enol to the diketo form. A total of 210 trajectories were run starting from this transition state, yielding chemically activated 1,3-cyclobutanedione radical cation. The majority of the trajectories resulted in $CH_2CO^{+\cdot}$ + CH_2CO, with the activated CC bond breaking nearly twice as often as the spectator CC bond. The non-statistical behavior is observed because the rate of energy redistribution within the molecule is comparable to or slower than the dissociation rates. In addition to the expected products, dissociation to $CH_2COCH_2^{+\cdot}$ + CO and formation a proton transferred product, $HCCO^{\cdot}$ + CH_3CO^{+} were also seen in some of the trajectories.

Chapter 5 describes a study of the dissociation of neutral and positively charged methanimine.[31] The structures and energetics of the reactants, intermediates, transition states and products for the dissociation of methanimine neutral, monocation, dication and trication were calculated at the CBS-APNO level of theory. The dissociations of the neutral, monocation and dication were studied by *ab initio* direct classical trajectory calculations at the B3LYP/6-311G(d,p) level of theory. A microcanonical ensemble using quasiclassical

normal mode sampling was constructed by distributing 200, 150 and 120 kcal/mol of excess energy above the local minima of the neutral, singly, and doubly charged species, respectively. Many of the trajectories dissociate directly to produce H^+, H atom or H_2. However, for a fraction of the cases, substantial migration of the hydrogen occurs within the molecule before dissociation. The preferred dissociation product for the neutral and the monocation is hydrogen atom. Elimination of H_2 was seen in 20% of the trajectories for the neutral and in 5% of the trajectories for the monocation. Dissociations of the dication and trication produced H^+ rather than H atom. $HCNH^+$ was formed in 85 – 90% of the dissociating trajectories for the monocation and dication.

In Chapter 6, the gas phase reaction of Th^+ with H_2O to produce $HThO^+$ + H and ThO^+ + H_2 was investigated by density functional theory and coupled cluster methods.[32] RRKM calculations of the branching ratio favor the H atomic elimination channel in disagreement with experiment. *Ab initio* classical trajectory calculations were carried out to obtain a better model of the molecular dynamics. The molecular dynamics simulations yield a branching ratio of ca 80% for the H_2 elimination channel to 20% for the H atomic elimination channel in qualitative agreement with the observed ratio of 65% to 35%.

Chapter 7 discusses the complexes of the form $An_2(C_8H_8)_2$ (An = Th, Pa, U and Np), which were investigated using density functional theory with scalar-relativistic effective core potentials.[33] For uranium, a coaxial isomer with D_{8h} symmetry is found to be more stable than a C_s isomer, in which the dimetal unit is perpendicular to the C_8 ring axis. Similar coaxial structures are predicted for

$Pa_2(C_8H_8)_2$ and $Np_2(C_8H_8)_2$, while in $Th_2(C_8H_8)_2$ the C_8H_8 rings tilt away from the An-An axis. Going from $Th_2(C_8H_8)_2$ to $Np_2(C_8H_8)_2$, the An-An bond length decreases from 2.81 Å to 2.19 Å and the An-An stretching frequency increases from 249 cm^{-1} to 354 cm^{-1}. This is a result of electrons populating An-An *5f* π- and δ-type bonding orbitals and φ non-bonding orbitals, thereby increasing in An-An bond order. $U_2(C_8H_8)_2$ is stable with respect to dissociation into $U(C_8H_8)$ monomers. Disproportionation of $U_2(C_8H_8)_2$ into uranocene and U atom is endothermic but is slightly exothermic for uranocene plus 1/2 U_2, suggesting that it might be possible to prepare double stuffed uranocene if suitable conditions can be found to avoid disproportionation.

Chapter 8 describes the collaboration with Dr. Mobashery on the inhibition of matrix metalloproteinases.[34] SB-3CT, (4-phenoxyphenylsulfonyl)methylthiirane is a potent, mechanism-based inhibitor of the gelatinase sub-class of the matrix metalloproteinase (MMP) family of zinc proteases. The gelatinase MMPs are unusual in that there are several examples where both enantiomers of a racemic inhibitor have comparable inhibitory abilities. SB-3CT is one such example. Here, the inhibition mechanism of the MMP2 gelatinase by the (*S*)-SB-3CT enantiomer and its oxirane analogue is examined computationally, and compared to the mechanism of (*R*)-SB-3CT. Inhibition of MMP2 by (*R*)-SB-3CT was shown previously to involve enzyme-catalyzed C–H deprotonation adjacent to the sulfone, with concomitant opening by β-elimination of the sulfur of the three-membered thiirane ring. Similarly to the *R* enantiomer, (*S*)-SB-3CT was docked into the active site of MMP2, followed by molecular dynamics simulation to

prepare the complex for combined quantum mechanics and molecular mechanics (QM/MM) calculations. QM/MM calculations with B3LYP/6-311+G(d,p) for the QM part (46 atoms) and the AMBER force field for the MM part were used to compare the reaction of (*S*)-SB-3CT and its oxirane analogue in the active site of MMP2 (9208 atoms). These calculations show that the barrier for the proton abstraction coupled ring opening reaction of (*S*)-SB-3CT in the MMP2 active site is 4.4 kcal/mol lower than its oxirane analogue, and the ring opening reaction energy of (*S*)-SB-3CT is only 1.6 kcal/mol less exothermic than its oxirane analogue. Calculations also show that the protonation of the ring-opened products by water is thermodynamically much more favorable for the alkoxide obtained from the oxirane, than for the thiolate obtained from the thiirane. In contrast to (*R*)-SB-3CT and the *R*-oxirane analogue, the double bonds of the ring-opened products of (*S*)-SB-3CT and its *S*-oxirane analogue have the *cis*-configuration. Vibrational frequency and intrinsic reaction path calculations on a reduced size QM/MM model (2747 atoms) provide additional insight into the mechanism. These calculations yield 5.9 and 6.7 for the deuterium kinetic isotope effect for C–H bond cleavage in the transition state for the *R* and *S* enantiomers of SB-3CT, in good agreement with the experimental results.

References

(1) Schlegel, H. B. *J. Comput. Chem.* **2003**, *24*, 1514-1527.

(2) Wales, D. J. *Energy landscapes*; Cambridge University Press: New York, 2003.

(3) Curtiss, L. A.; Redfern, P. C.; Raghavachari, K. *J. Chem. Phys.* **2007**, *126*, 084108.

(4) Barnes, E. C.; Petersson, G. A.; Montgomery, J. A.; Frisch, M. J.; Martin, J. M. L. *J. Chem. Theory. Comput.* **2009**, *5*, 2687-2693.

(5) Montgomery, J. A.; Ochterski, J. W.; Peterson, G. A. *J. Chem. Phys.* **1994**, *101*, 5900-5909.

(6) Gao, J. Methods and Applications of Combined Quantum Mechanical and Molecular Mechanical Potentials. In *Reviews in Computational Chemistry*; Lipkowitz, K. B., Boyd, D. B., Eds. New York, 1996; Vol. 7, p 119-195.

(7) Froese, R. D. J.; Morokuma, K. Hybrid Method. The ONIOM Method. Integration of Different Levels of Molecular Orbital Methods and/or Molecular Mechanics Methods for Large Molecular Systems and Its Applications to Structures, Energies and Chemical Reactions. In *Encyclopedia of Computational Chemistry*; Schleyer, P. v. R., Allinger, N. L., Clark, T., Gasteiger, J., Kollman, P. A., Schaefer III, H. F., Schreiner, P. R., Eds.; John Wiley: Chichester, 1998; Vol. 2, p 1245-1257.

(8) Monard, G.; Merz, K. M. *Acc. Chem. Res.* **1999**, *32*, 904-911.

(9) Garrett, B. C.; Truhlar, D. G. Transition State Theory. In *Encyclopedia of Computational Chemistry*; Schleyer, P. v. R., Allinger, N. L., Clark, T., Gasteiger, J., Kollman, P. A., Schaefer III, H. F., Eds.; John Wiley: Chichester, 1998; Vol. 5, p 3094-3104.

(10) Steinfeld, J. I.; Francisco, J. S.; Hase, W. L. *Chemical kinetics and dynamics*; 2nd ed.; Prentice Hall: Upper Saddle River, N.J., 1999.

(11) Marcus, R. A.; Rice, O. K. *J. Phys. Chem.* **1951**, *55*, 894-908.

(12) Depke , G.; Lifshitz , C.; Schwarz, H.; Tzidony, E. *Angew. Chem., Int. Ed. Engl.* **1981**, *20*, 792-793.

(13) McAdoo, D. J.; Hudson, C. E. *Int. J. Mass Spectrom. Ion Processes* **1984**, *59*, 77-83.

(14) Turecek, F.; Hanus, V. *Org. Mass Spectrom.* **1984**, *19*, 631-638.

(15) Osterheld, T. H.; Brauman, J. I. *J. Am. Chem. Soc* **1993**, *115*, 10311-10316.

(16) Suits, A. G. *Acc. Chem. Res.* **2008**, *41*, 873-881.

(17) Lahankar, S. A.; Chambreau, S. D.; Townsend, D.; Suits, F.; Farnum, J.; Zhang, X. B.; Bowman, J. M.; Suits, A. G. *J. Chem. Phys.* **2006**, *125*, 10.

(18) Lahankar, S. A.; Chambreau, S. D.; Zhang, X. B.; Bowman, J. M.; Suits, A. G. *J. Chem. Phys.* **2007**, *126*, 8.

(19) Townsend, D.; Lahankar, S. A.; Lee, S. K.; Chambreau, S. D.; Suits, A. G.; Zhang, X.; Rheinecker, J.; Harding, L. B.; Bowman, J. M. *Science* **2004**, *306*, 1158-1161.

(20) Chambreau, S. D.; Townsend, D.; Lahankar, S. A.; Lee, S. K.; Suits, A. G.; Royal Swedish Acad Sciences: 2006, p C89-C93.

(21) Rubio-Lago, L.; Amaral, G. A.; Arregui, A.; Izquierdo, J. G.; Wang, F.; Zaouris, D.; Kitsopoulos, T. N.; Banares, L. *Phys. Chem. Chem. Phys.* **2007**, *9*, 6123-6127.

(22) Houston, P. L.; Kable, S. H. *Proc. Natl. Acad. Sci. U. S. A.* **2006**, *103*, 16079-16082.

(23) Bunker, D. L. *Methods Comput. Phys.* **1971**, *10*, 287.

(24) Raff, L. M.; Thompson, D. L. The Classical Trajectory Approach to Reactive Scattering. In *Theory of Chemical Dynamics*; Baer, M., Ed.; CRC Press: Boca Raton, 1985; Vol. III, p 1.

(25) Thompson, D. L. Trajectory Simulations of Molecular Collisions: Classical treatment. In *Encyclopedia of Computational Chemistry*; Schleyer, P. v. R., Allinger, N. L., Clark, T., Gasteiger, J., Kollman, P. A., Schaefer III, H. F., Eds.; John Wiley: Chichester, 1998; Vol. 5, p 3056-3073.

(26) Hase, W. L.; Song, K. H.; Gordon, M. S. *Comput. Sci. Eng.* **2003**, *5*, 36-44.

(27) Millam, J. M.; Bakken, V.; Chen, W.; Hase, W. L.; Schlegel, H. B. *J. Chem. Phys.* **1999**, *111*, 3800-3805.

(28) Bakken, V.; Millam, J. M.; Schlegel, H. B. *J. Chem. Phys.* **1999**, *111*, 8773-8777.

(29) Zhou, J.; Schlegel, H. B. *J. Phys. Chem. A* **2008**, *112*, 13121-13127.

(30) Zhou, J.; Schlegel, H. B. *J. Phys. Chem. A* **2009**, *113*, 1453-1458.

(31) Zhou, J.; Schlegel, H. B. *J. Phys. Chem. A* **2009**, *113*, 9958-9964.

(32) Zhou, J.; Schlegel, H. B. *J. Phys. Chem. A* **2010**, *114*, 8613-8617.

(33) Zhou, J.; Sonnenberg, J. L.; Schlegel, H. B. *Inorg. Chem.* **2010**, *49*, 6545-6551.

(34) Zhou, J.; Tao, P.; Fisher, J. F.; Shi, Q.; Mobashery, S.; Schlegel, H. B. *J. Chem. Theory Comput.* **2010**, *6*, 3580-3587.

CHAPTER 2

DISSOCIATION OF ACETONE RADICAL CATION ($CH_3COCH_3^{+\cdot} \rightarrow CH_3CO^+ + CH_3^{\cdot}$): AN *AB INITIO* DIRECT CLASSICAL TRAJECTORY STUDY OF THE ENERGY DEPENDENCE OF THE BRANCHING RATIO

2.1 Introduction:

The non-statistical dissociation of acetone radical cation has been the subject of a number of experimental and theoretical studies over the past 35 years. Isomerization from the more stable enol form to the keto isomer leads to chemical activation of the newly formed methyl group which dissociates preferentially. The gas phase chemistry and non-ergodic behavior of $C_3H_6O^{\cdot+}$ ions has been reviewed by McAdoo.[1] The enol form of acetone radical cation can be generated from higher aliphatic ketones via the McLafferty rearrangement or by cycloreversion of 1-methlcyclobutanol (Scheme 2.1).[2]

The enol form of the acetone cation can isomerize to the keto form and then dissociate to produce acetyl cation and methyl radical (Scheme 2.2). The dissociation reaction proceeds non-ergodically, favoring the departure of the newly formed methyl group.

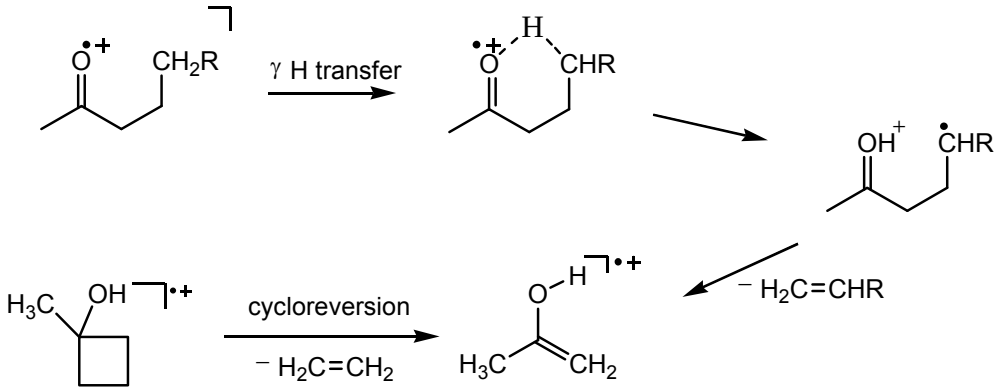

Scheme 2.1

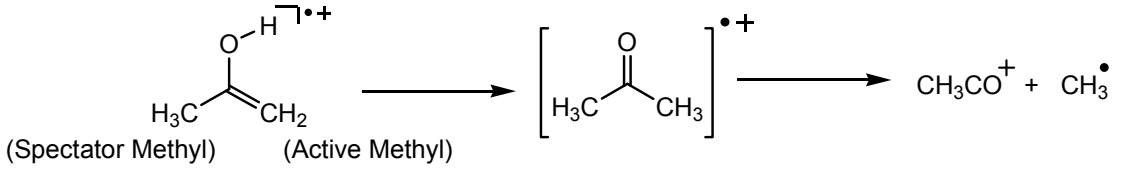

Scheme 2.2

The average ratio for the loss of the active methyl versus loss of the spectator methyl was observed to be ca 1.4:1,[3-6] whereas RRKM theory would predict that the two methyl groups should dissociate at equal rates.[2,3,7-9,10] This indicates that randomization of the internal energy is incomplete before dissociation occurs.

Preferential loss of the active methyl group has been seen in collisional activation, electron impact and metastable ion experiments.[1] The energy dependence of the non-statistical dissociation was studied by Osterheld and Brauman by infrared multiphoton dissociation of acetone enol cation.[6] A branching ratio of 1.16 was found at ca. 0 – 3 kcal mol^{-1} above threshold and increased to 1.55 at an estimated energy of 8 – 12 kcal/mol above the barrier. They attribute the increase in branching ratio to the excitation of a mode other

than the reaction coordinate, possibly the C-C-O bending involving the spectator methyl group.

Recent photoionizantion[11] and TPEPICO[12] experiments yield 18.5±0.5 kcal/mol for the energy difference between $CH_3COCH_3^{\cdot+}$ and $CH_3CO^+ + CH_3^{\cdot}$ at 0 K. This is slightly lower than the previous experimental value 19.8±0.3 kcal/mol.[13] A number of groups have used *ab initio* calculations to explore the potential energy surface for $CH_3COCH_3^{\cdot+}$.[11,14,15] The experimental values for $CH_3COCH_3^{\cdot+} \rightarrow CH_3CO^+ + CH_3^{\cdot}$ fall in between the best calculated values, 17.7, 17.9, 21.1 and 20.6 kcal/mol for G2MP2,[14] G3,[11] CBS-QB3[15] and CBS-APNO,[15] respectively. The best estimates for the keto to enol isomerization barrier $CH_3COCH_3^{\cdot+}$ at 0 K are 36.0, 36.6, 35.8 and 34.7 kcal/mol for G2MP2,[14] G3,[11] CBS-QB3[15] and CBS-APNO,[15] respectively.

The non-statistical dynamics of acetone radical cation dissociation has been studied by quasiclassical trajectory calculations. Nummela and Carpenter[16] used semi-empirical AM1 calculations with specific reaction parameters (AM1-SRP) and obtained a branching ratio of 1.13±0.09 for dissociation of the active versus the spectator methyl group. The trajectories were started at the transition state for keto-enol tautomeriztion and were sampled from a microcanonical distribution with 10 kcal/mol energy in excess of the zero point energy of the transition state. Anand and Schlegel[15] found a branching ratio of 1.53±0.20 at the MP2/6-31G(d) level of theory using the same starting conditions. In the present work, we used quasiclassical trajectory calculations at the MP2/6-31G(d) level of

theory with bond additivity corrections[17-21] to study the energy dependence of the branching ratio.

2.2 Computational Methods:

The Gaussian[22] suite of programs was employed to carry out the *ab initio* electronic structure and molecular dynamics calculations. The geometries of the minima and the transition states have been optimized previously[15] by Hartree-Fock theory (HF), density functional theory (DFT), second order Møller-Plesset perturbation theory (MP2) and quadratic configuration interaction with single and double excitations (QCISD).[23] The density functionals used in this work include two hybrid GGA (generalized gradient approximation) functionals, B3LYP[24,25] and PBE1PBE,[26] and a meta-GGA, TPSSTPSS[27]. The complete basis set extrapolation methods (CBS-QB3 and CBS-APNO) of Petersson and co-workers[28] were used to compute accurate energy differences. The CBS-APNO calculations have a mean absolute deviation of 0.5 kcal/mol for heats of reaction.

Accurate methods such as CBS-APNO are not practical for molecular dynamics corrections, but more affordable methods such as DFT and MP2 may not yield sufficiently accurate energetics. However, the errors are often systematic, e.g. arising from the making and breaking of bonds. The empirical corrections that have been used to correct computed thermochemistry[17-21] can also be employed to improve potential energy surfaces for molecular dynamics calculations.[29] As in the BAC-MP4 method[21], a simple exponential is used to correct the potential for bond dissociations. In the present case, the bond

additivity correction (BAC) is applied only to the C-C bonds for the dissociation of the active and spectator methyl groups:

$$\Delta E_{BAC} = A\exp(-\alpha R_{CC1}) + A\exp(-\alpha R_{CC2}) \quad (1)$$

The parameters $A = -0.028$ and $\alpha = 0.196$ are obtained by fitting the MP2/6-31G(d) energetics to the CBS-APNO level of theory. The structures used in the fit include the transition state (TS) for enol-keto isomerization, the keto isomer, and the methyl dissociation products. The corresponding first and second derivatives of E_{BAC} are added to MP2 gradient and Hessian. This BAC approach has been used previously to study the branching ratios in $CH_2O^{\cdot-} + CH_3Cl \rightarrow CH_3CH_2O^{\cdot} + Cl^-$, $CH_2O + CH_3^{\cdot} + Cl^-$.[29]

Ab initio classical trajectories were computed at the BAC-MP2/6-31G(d) level of theory using a Hessian-based predictor-corrector method.[30,31] A predictor step is taken on the quadratic surface obtained from the energy, gradient and Hessian from the beginning point. A fifth order polynomial is then fitted to the energies, gradients and Hessians at the beginning and end points of the predictor step, and the Bulirsch Stoer algorithm[32] is used to take a corrector step on this fitted surface with the angular forces projected out. The Hessians are updated for 5 steps before being recalculated analytically.[30] The trajectories were terminated when the centers of mass of the fragments were 8 bohr apart and the gradient between the fragments was less than 1×10^{-5} hartree/bohr. A step size of 0.25 amu$^{1/2}$ bohr was used for integrating the trajectories. The energy was conserved to better than 1×10^{-5} hartree and the angular momentum was conserved to 1×10^{-8} ħ.

Trajectories were initiated at the transition state for the keto-enol tautomerization. For the first part of the study, a microcannonical ensemble of initial states was constructed using quasi-classical normal mode sampling.[33,34] A total energy of 1, 2, 10, and 18 kcal/mol above the zero point energy of the transition state was distributed among the 23 vibrational modes and translation along the transition vector. The total angular momentum was set to zero corresponding to a rotationally cold distribution and the phases of the vibrational modes were chosen randomly. For each initial condition, the momentum and displacement were scaled so that the desired total energy was the sum of the vibrational kinetic energy and the potential energy obtained from the ab initio surface. The initial conditions are similar to those chosen by Nummela and Carpenter.[16] For each case, a total of 200 - 300 trajectories were integrated for up to 400 *fs* starting at the transition state and ending when the products were well separated. In the second part of the study, 1, 2, 4 and 8 kcal/mol was added to each of 3 selected vibrational modes and 0.5 kcal/mol of translational energy was added to the transition vector, while the remaining modes were given only zero point energy. The remaining conditions were the same as in the first part of the study, and 110 trajectories were integrated for each case. A total of ca 2500 trajectories were calculated for the 17 different ensembles (200 – 300 trajectories for each of 4 microcanonical ensembles and 110 trajectories for each of the 13 ensembles for specific mode excitation).

2.3 Results and Discussion

Structures and Energetics

Figure 2.1 shows the optimized geometries of the key structures on the potential energy surface for acetone radical cation dissociation at the TPSSTPSS, MP2, BAC-MP2 and QCISD levels of theory. The largest differences are the monomer separations in the ion-neutral complexes, (**3**) and (**4**). The transition states calculated by TPSS are somewhat earlier than those calculated by MP2 or QCISD. The bond additivity corrections produce only minor changes in the MP2 geometry. The bond lengths between heavy atoms at TPSS, MP2 and BAC-MP2 have similar mean absolute deviations (ca 0.01 Å) when compared to the QCISD structures.

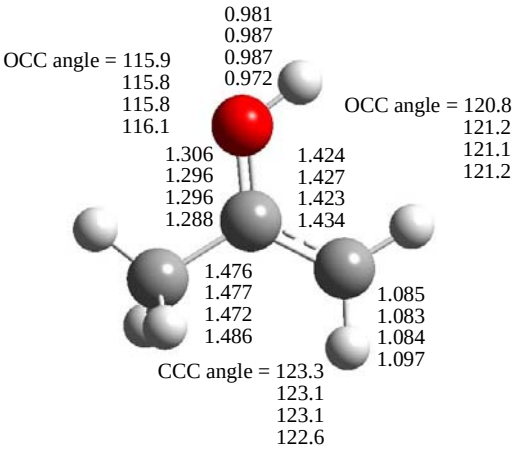

Enol Isomer (**1**)

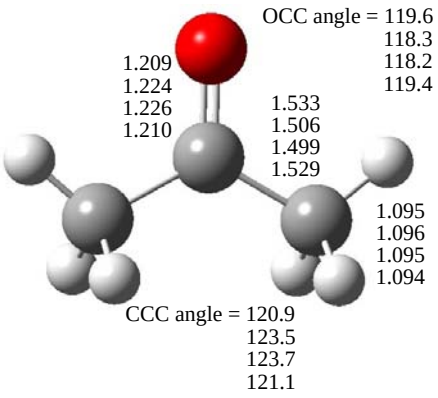

Keto Isomer (**2**)

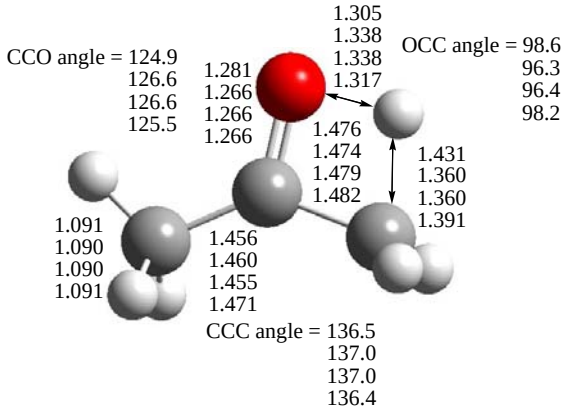

TS for Isomerization (**TS1**)

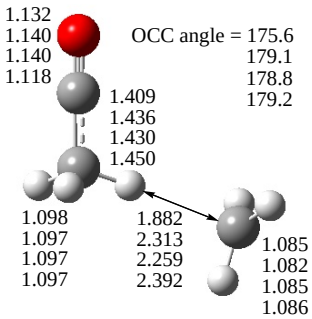

Ion-Neutral Complex (**3**)

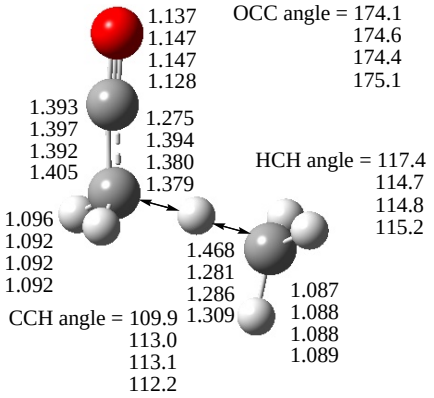

TS for Methane Elimination (**TS3**)

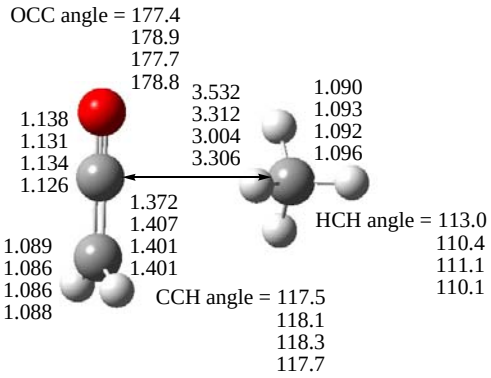

Ketene-Methane Complex (**4**)

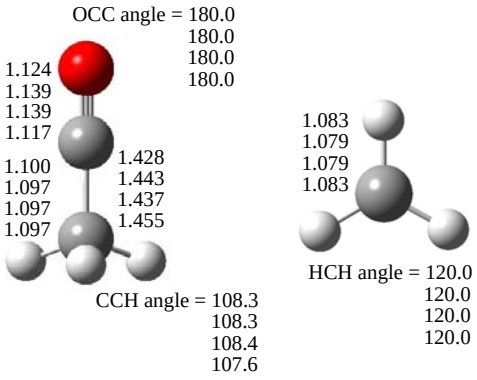

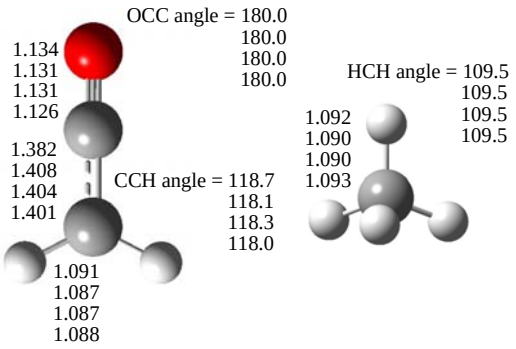

Separated Acetyl Cation and Methyl Radical (**5**) Separated Ketene and Methane (**6**)

Figure 2.1 Structures and selected geometric parameters of stationary points on the acetone radical cation potential energy surface optimized at the TPSSTPSS/cc-pVTZ, MP2/6-31G(d), BAC-MP2/6-31G(d), and QCISD/6-311G(d,p) levels of theory (top row to bottom, respectively). Bond distances are in Å, and angles are in degree.

The relative energies are collected in Table 2.1. As can be judged from the mean absolute deviations, the QCISD(T) and CBS-QB3 calculations are in very good agreement with the CBS-APNO calculations. However, ab initio trajectory calculations are not feasible with CBS, QCI or MP3 methods. The methyl dissociation energy is too low at the MP2 level, but is much improved at the BAC-MP2 level. The TPSS calculations with a large basis set perform significantly better than B3LYP or PBE. However, trajectory calculations with the TPSS/cc-pVTZ level of theory are estimated to be ca 10 times more expensive than the BAC-MP2 trajectories. The B3LYP/6-31G(d) is comparable in cost to BAC-MP2/6-31G(d). However, B3LYP/6-31G(d) places the $CH_2CO^+ + CH_4$ channel (**6**) substantially below the $CH_3CO^+ + CH_3$ channel (**5**). This cannot be fixed with a simple bond additivity correction involving only the two C-C bonds. Although higher levels of theory would provide a more accurate description of the potential energy surface, the BAC-MP2 level is a reasonable compromise between accuracy and affordability that allows us to calculate the ca 2500 trajectories needed to explore the energy dependence of the branching ratio.

Table 2.1 Energies of the various points on the acetone radical cation PES[a]

	1	**TS1**	**2**	**3**	**TS3**	**4**	**5**	**6**	**MAD[b]**
B3LYP/6-31G(d)	-4.5	37.8	0.0	19.3	19.3	18.3	26.4	22.3	3.2
B3LYP/cc-pVTZ[c]	-10.2	38.1	0.0	--	--	--	24.4	--	
PBE1PBE/cc-pVTZ	-8.6	33.5	0.0	19.5	19.3	19.9	25.7	24.1	3.1
TPSSTPSS/cc-pVTZ	-5.1	33.3	0.0	15.5	14.9	14.3	23.2	20.3	1.8
MP2/6-31G(d)	-12.2	36.0	0.0	4.6	12.5	9.0	8.5	11.1	5.7
MP2/6-311+G(d,p)	-13.9	34.0	0.0	2.3	8.5	6.4	5.7	9.0	7.7
BAC-MP2/6-31G(d)	-12.6	35.7	0.0	10.4	13.5	13.0	16.2	21.6	2.9
MP3/6-31G(d,p)[d]	-12.0	39.4	0.0	16.1	24.0	16.8	21.0	20.6	2.6
QCISD/6-311G(d,p)[e]	-6.1	40.1	0.0	13.1	20.2	14.5	16.1	16.7	2.1
QCISD(T)/6-311++G(2df,p)[f]	-7.6	36.6	0.0	14.0	18.4	15.0	17.3	17.9	0.8
CBS-QB3	-7.8	35.8	0.0	16.1	18.9	15.4	19.4	18.5	0.3
CBS-APNO	-8.0	35.2	0.0	15.3	18.1	15.1	19.3	18.5	

[a] In kcal/mol at 0 K, relative to **2** (keto isomer).
[b] Mean absolute deviation from the CBS-APNO level of theory.
[c] Ref. 16.
[d] Ref. 10.
[e] with MP2/6-31G(d) zero point energies.
[f] QCISD/6-311G(d,p) geometry with MP2/6-31G(d) zero point energies

Dynamics

Microcanonical Ensemble

Four sets of initial conditions were constructed with 1, 2, 10, and 18 kcal/mol above the zero point energy of the transition state. The results of the trajectory calculations for the dissociation of acetone radical cation are listed in Table 2.2. For the 300 trajectories of with 1 kcal/mol extra energy, 109 resulted in the loss of the active methyl and 76 finished with the loss of the spectator methyl. The remaining 115 trajectories either went to the enol isomer (63 trajectories), or stayed near the keto minimum (52 trajectories), not meeting the stopping criteria within 400 *fs*. Of the 300 trajectories integrated with 2 kcal/mol extra energy, 150 resulted in the loss of the active methyl and 80 finished with the loss of the spectator methyl. Integration of 250 trajectories of with 10 kcal/mol extra energy yielded 126 active methyl dissociations and 74 spectator methyl dissociations. The 237 trajectories with 18 kcal/mol extra energy resulted in 120 active methyl loses and 80 spectator methyl loses. As the energy of the microcanonical ensemble is increased from 1 to 2 kcal/mol, the branching ratio for active to spectator methyl group increases from 1.43 to 1.88. However, when the energy of the microcanonical ensemble continues to increase from 2 to 10 to 18 kcal/mol, the branching ratio for active to spectator methyl group decreases from 1.88 to 1.70 to 1.50. By contrast, in the experiments of Osterheld and Brauman[6] the branching ratio increases with increasing laser intensity and then seems to reach a plateau. This suggests that energy may be deposited preferentially in

specific modes, rather than uniformly in all of the vibrational modes. This will be examined in the second part of the study (see below).

Table 2.2 Number of trajectories for the dissociation of acetone radical cation

Ensemble Energy (kcal/mol)	Nonreactive (enol/keto)	Active Methyl	Spectator Methyl	Ratio (Active:Spectator)
1	63/52	109	76	1.43:1
2	36/34	150	80	1.88:1
10	11/39	126	74	1.70:1
18	9/28	120	80	1.50:1

At each energy in the microcanonical simulations on the BAC-MP2 surface, a number of trajectories stayed in the keto minimum, while in the previous study at the MP2 level without bond additivity corrections, none of the trajectories remained in the keto minimum. The MP2/6-31G(d) level of theory underestimates C-C bond energy of keto isomer in comparison to CBS-APNO, permitting the methyl group to dissociate more easily. The BAC-MP2/6-31G(d) calculations yield a higher methyl dissociation energy, and some trajectories cannot overcome the barrier for dissociation to the products within the simulation time. The higher barrier at the BAC-MP2/6-31G(d) level is much closer to experiment and the CBS-APNO calculations, and hence the dynamics should be more realistic at this level of theory.

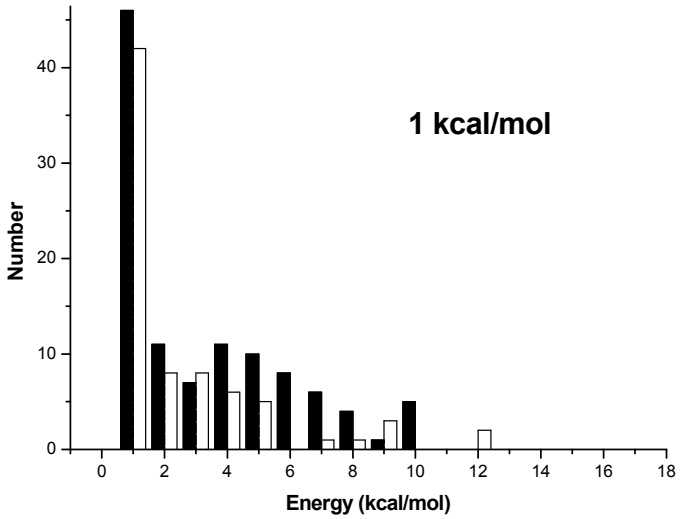
1 kcal/mol
Number
Energy (kcal/mol)
0
10
20
30
40
0
2
4
6
8
10
12
14
16
18

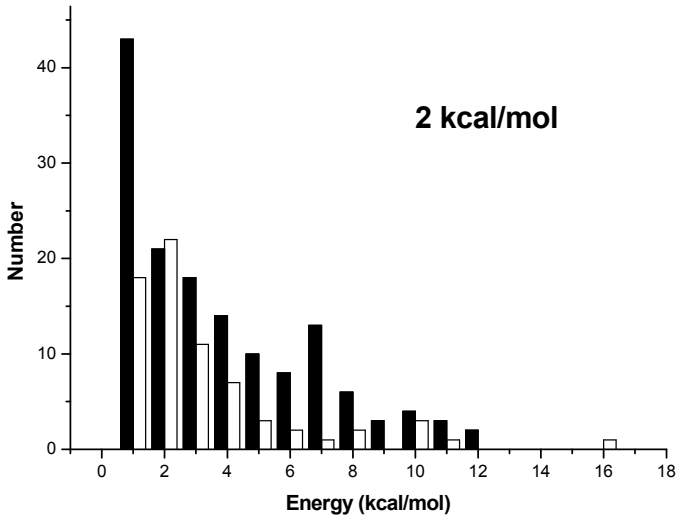
2 kcal/mol
Number
Energy (kcal/mol)
0
10
20
30
40
0
2
4
6
8
10
12
14
16
18

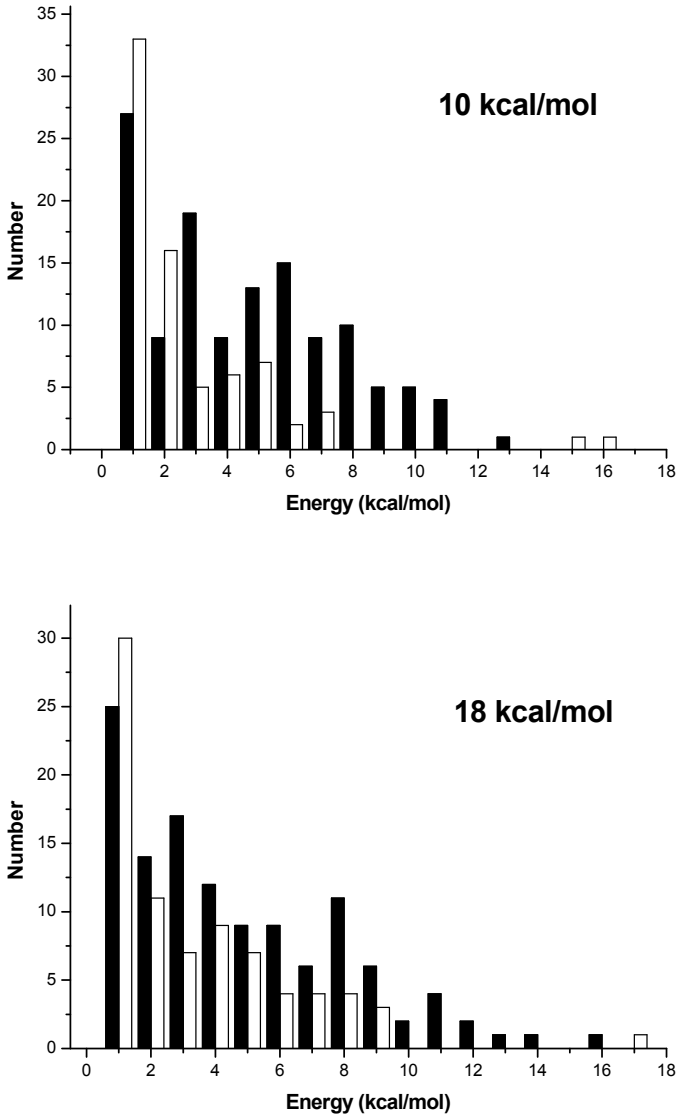

Figure 2.2 Translational energy distributions of the methyl fragments derived from the active (filled) and spectator (empty) methyl fragments with 1, 2, 10, and 18 kcal/mol excess energies.

The calculated translational energy distributions are plotted in Figure 2.2. The majority of methyl groups have a translational energy less than 4 kcal/mol. Of the methyl groups with larger translational energies, many come from dissociation of the active methyl. As indicated in Table 2.3, the active methyl has a larger average translational energy than spectator methyl. Experimentally, the kinetic energy releases for the active and spectator methyl groups are 5.0 and 4.3 kcal/mol, respectively.[8] As the total extra energy increases, the average translational energy of the active methyl group increases more than that of the spectator methyl group. Table 2.3 also lists the average dissociation times. The dissociation time is taken as the time when the C-C bond reaches 3.0 Å, provided that the methyl group does not return to form the C-C bond again. The average dissociation times generally decrease with increasing energy, and the average time for the active methyl dissociation time is always shorter than for the spectator methyl. Just as the branching ratio increases first and then decreases with increasing energy, the ratio of the spectator to active methyl group average dissociation times also has the same trend with increasing energy.

Figure 2.3 plots the logarithm of the number of undissociated acetone radical cations versus time. The nearly linear plots are indicative of first-order kinetics as expected for unimolecular dissociation. The spectator methyl groups generally needed more time to dissociate than the active methyl, validating the result of average dissociation time listed in Table 2.3.

Table 2.3 Average translational energies E (in kcal/mol) and dissociation time T (in *fs*)

Ensemble Energy (kcal/mol)	Active Methyl		Spectator Methyl	
	E	T	E	T
1	2.737	181.09	1.996	224.39
2	3.306	177.14	2.705	240.22
10	4.177	147.47	2.256	185.69
18	4.204	139.91	2.833	167.40

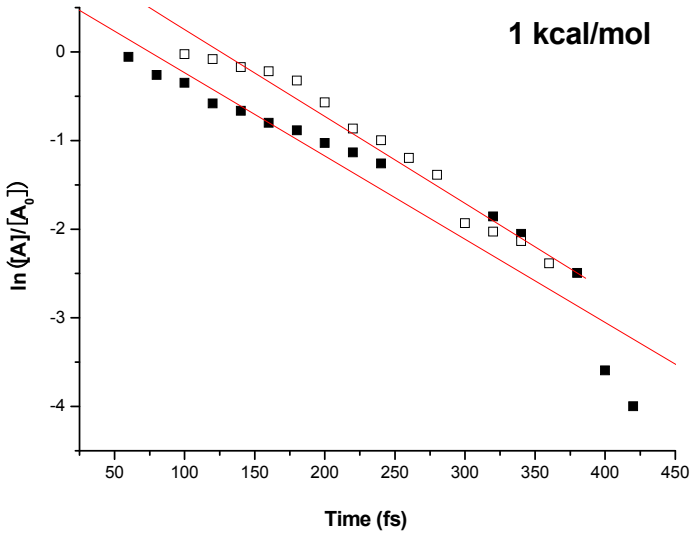
1 kcal/mol
ln ([A]/[A0])
Time (fs)
0
-1
-2
-3
-4
50
100
150
200
250
300
350
400
450

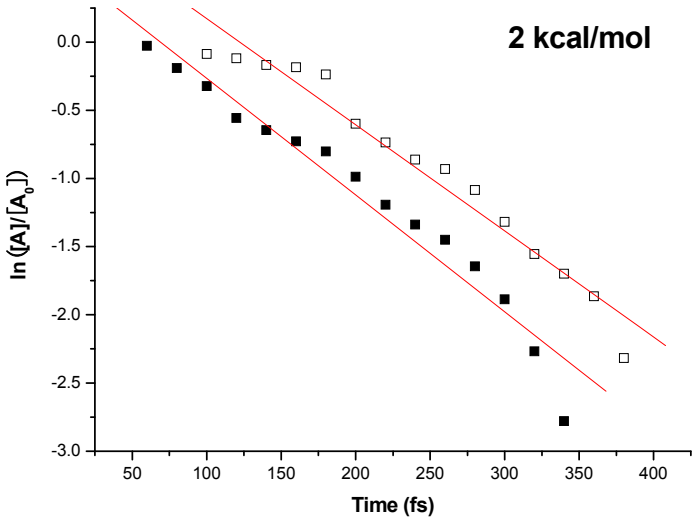
2 kcal/mol
ln ([A]/[A0])
Time (fs)
0.0
-0.5
-1.0
-1.5
-2.0
-2.5
-3.0
50
100
150
200
250
300
350
400

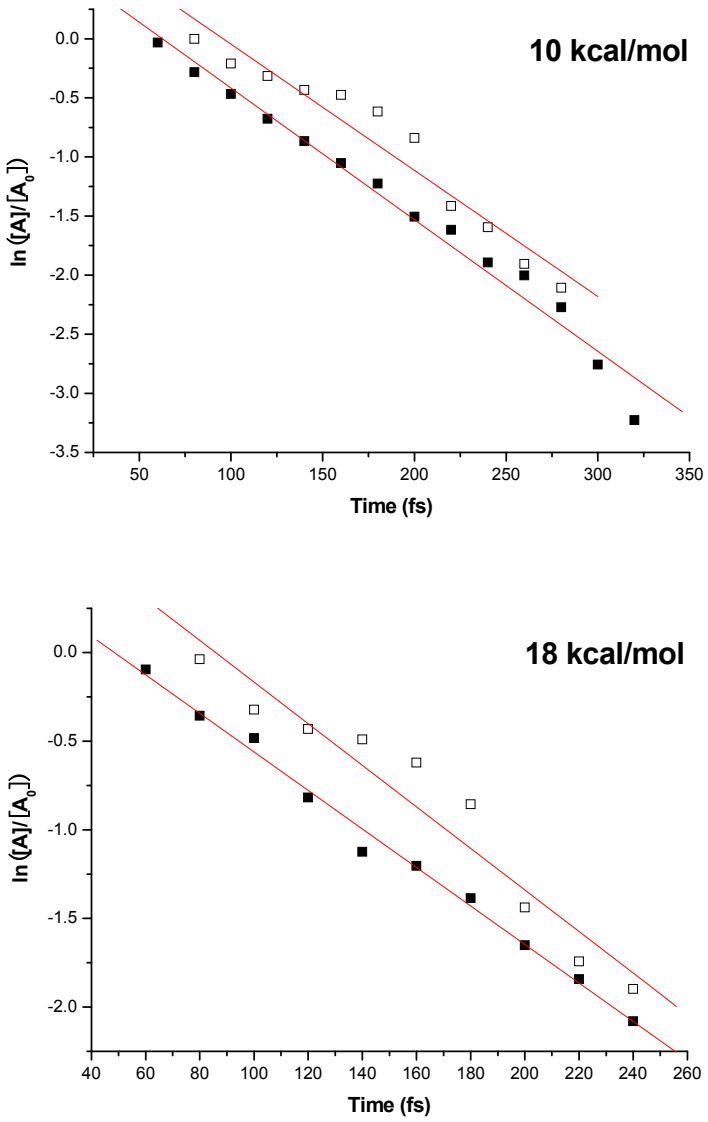

Figure 2.3 Plot showing the first-order kinetics for active (filled) and spectator (empty) methyl fragments dissociation with 1, 2, 10, and 18 kcal/mol excess energies.

Excitation of Specific Modes

Osterheld and Brauman suggested that the increase in branching ratio with laser intensity was due to the excitation of specific vibrational modes. In particular, they indicated that the C-C-O bending modes may be suitable candidates. An examination of the vibrations of TS for enol-keto isomerization yields three modes involved C-C-O bending, as shown in Figure 2.4. For each mode, four ensembles were constructed with 1, 2, 4, and 8 kcal/mol excess amount of energy in the specific mode, 0.5 kcal/mol in the transition vector, and zero point energy in all modes. For comparison, one ensemble was also constructed without specific mode excitation, having only 0.5 kcal/mol in the transition vector and zero point energy in each of the vibrational modes. For each set, a total of 110 trajectories were integrated.

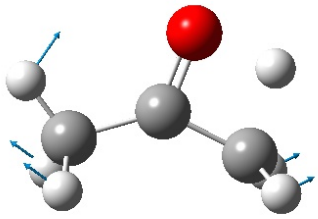

Mode 3, 374 cm^{-1}

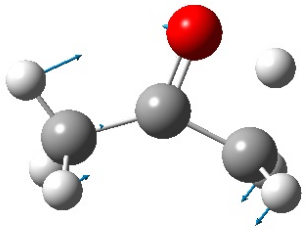

Mode 6, 706 cm^{-1}

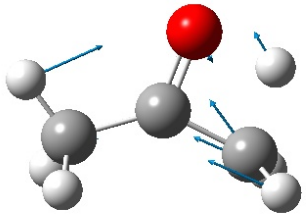

Mode 8, 952 cm^{-1}

Figure 2.4 Displacement vectors for vibrational modes 3, 6, and 8, along with corresponding vibrational frequencies.

Table 2.4 Branching ratio for exciting specific modes[b]

Ensemble Energy (kcal/mol)	Mode 3	Mode 6	Mode 8
0	1.10:1	1.10:1	1.10:1
1	1.59:1	1.58:1	1.54:1
2	1.84:1	2.31:1	1.82:1
4	1.46:1	1.85:1	2.36:1
8	1.55:1	2.03:1	2.76:1

[b] Zero point energy in the remaining vibrational modes and 0.5 kcal/mol in the transition vector.

The branching ratio for the various cases of specific mode excitation can be found in Table 2.4. If only 0.5 kcal/mol is added in the transition vector, the branching ratio is 1.10:1. This indicates that the energy released in descending from the transition state to the keto minimum is not deposited efficiently in the modes favoring the dissociation of the active methyl group. For each of the three modes involving C-C-O bending, the branching ratio increases to 1.5:1 when as little as 1 kcal/mol extra energy is in the mode. Adding 2 kcal/mol to any of the three modes increases the branching ratio to 1.8 – 2.3. Depositing energy in mode 8 is the most effective of the three modes examined. Adding more energy to mode 3 and 6 actually decreases the branching ratio. This parallels the study using a microcanonical ensemble, in which the branching ratio decreases when more than 2 kcal/mol extra energy is added. Most likely, specific excitation of other vibrational mode will alter the branching ratio as well.

2.4 Conclusions:

The energy dependence of the branching ratio for acetone radical cation has been investigated by *ab initio* direct classical trajectory calculations. The MP2/6-31G(d) level of theory with bond additivity corrections gives a better potential energy surface than the MP2 and B3LYP levels of theory when compared to the CBS-APNO results. The non-statistical dissociation of acetone radical cation has been studied using microcanonical ensembles and specific mode excitation. For microcanonical ensembles, the ratios of methyl radical production from the newly formed (active) methyl to the existing (spectator) methyl are 1.43, 1.88, 1.70, and 1.50 for 1, 2, 10, and 18 kcal/mol of excess

energy, respectively. The dissociations generally obey first-order unimolecular kinetics. The active methyl usually carries more kinetic energy than spectator methyl, and average dissociation time of active methyl is less than that of spectator methyl. Three vibrations involving C-C-O bending were chosen for the specific mode excitation. In each case, the branching ratio increases when 1 or 2 kcal/mol was added. For two of the modes, the branching ratio decreased when more than 2 kcal/mol energy was added, similar to the study of microcanonical ensembles. However, for mode 8, the branching ratio continued to increase with added energy, reaching a ratio of 2.76:1 with 8 kcal/mol of excess energy.

2.5 References

(1) McAdoo, D. J. *Mass Spectrom. Rev.* **2000**, *19*, 38-61.

(2) McLafferty, F. W.; McAdoo, D. J.; Smith, J. S.; Kornfeld, R. *J. Am. Chem. Soc.* **1971**, *93*, 3720-30.

(3) Depke , G.; Lifshitz , C.; Schwarz, H.; Tzidony, E. *Angew. Chem. Int. Ed.* **1981**, *20*, 792-793.

(4) McAdoo, D. J.; Hudson, C. E. *Int. J. Mass Spectrom. Ion Processes* **1984**, *59*, 77-83.

(5) Turecek, F.; Hanus, V. *Org. Mass Spectrom.* **1984**, *19*, 631-638.

(6) Osterheld, T. H.; Brauman, J. I. *J. Am. Chem. Soc.* **1993**, *115*, 10311-16.

(7) Lifshitz, C.; Berger, P.; Tzidony, E. *Chem. Phys. Lett.* **1983**, *95*, 109-113.

(8) Lifshitz, C.; Tzidony, E. *Int. J. Mass Spectrom. Ion Processes Phys.* **1981**, *39*, 181-95.

(9) Lifshitz, C.; Tzidony, E.; Terwilliger, D. T.; Hudson, C. E. *Adv. Mass Spectrom.* **1980**, *8A*, 859-66.

(10) Heinrich, N.; Louage, F.; Lifshitz, C.; Schwarz, H. *J. Am. Chem. Soc.* **1988**, *110*, 8183-8192.

(11) Wei, L. X.; Yang, B.; Yang, R.; Huang, C. Q.; Wang, J.; Shan, X. B.; Sheng, L. S.; Zhang, Y. W.; Qi, F.; Lam, C. S.; Li, W. K. *J. Phys. Chem. A* **2005**, *109*, 4231-4241.

(12) Rennie, E. E.; Boulanger, A. M.; Mayer, P. M.; Holland, D. M. P.; Shaw, D. A.; Cooper, L.; Shpinkova, L. G. *J. Phys. Chem. A* **2006**, *110*, 8663-8675.

(13) Fogleman, E. A.; Koizumi, H.; Kercher, J. P.; Sztaray, B.; Baer, T. *J. Phys. Chem. A* **2004**, *108*, 5288-5294.

(14) Mishima, K.; Hayashi, M.; Lin, S. H. *Int. J. Mass Spectrom.* **2004**, *238*, 1-15.

(15) Anand, S.; Schlegel, H. B. *Phys. Chem. Chem. Phys.* **2004**, *6*, 5166-5171.

(16) Nummela, J. A.; Carpenter, B. K. *J. Am. Chem. Soc.* **2002**, *124*, 8512-8513.

(17) Allendorf, M. D.; Melius, C. F. *J. Phys. Chem. A* **2005**, *109*, 4939-4949.

(18) Anantharaman, B.; Melius, C. F. *J. Phys. Chem. A* **2005**, *109*, 1734-1747.

(19) Ho, P.; Coltrin, M. E.; Binkley, J. S.; Melius, C. F. *J. Phys. Chem.* **1985**, *89*, 4647-4654.

(20) Melius, C. F.; Allendorf, M. D. *J. Phys. Chem. A* **2000**, *104*, 2168-2177.

(21) Ho, P.; Melius, C. F. *J. Phys. Chem.* **1990**, *94*, 5120-5127.

(22) Frisch, M. J.; Trucks, G. W.; Schlegel, H. B.; Scuseria, G. E.; Robb, M. A.; Cheeseman, J. R.; Montgomery, J. A., Jr.; Vreven, T.; Scalmani, G.; Mennucci, B.; Barone, V.; Petersson, G. A.; Caricato, M.; Nakatsuji, H.; Hada, M.; Ehara, M.; Toyota, K.; Fukuda, R.; Hasegawa, J.; Ishida, M.; Nakajima, T.; Honda, Y.; Kitao, O.; Nakai, H.; Li, X.; Hratchian, H. P.; Peralta, J. E.; Izmaylov, A. F.; Kudin, K. N.; Heyd, J. J.; Brothers, E.; Staroverov, V.; Zheng, G.; Kobayashi, R.; Normand, J.; Sonnenberg, J. L.; Iyengar, S. S.; Tomasi, J.; Cossi, M.; Rega, N.; Burant, J. C.; Millam, J. M.; Klene, M.; Knox, J. E.; Cross, J. B.; Bakken, V.; Adamo, C.; Jaramillo, J.; Gomperts, R.; Stratmann, R. E.; Yazyev, O.; Austin, A. J.; Cammi, R.; Pomelli, C.; Ochterski, J. W.; Ayala, P. Y.; Morokuma, K.; Voth, G. A.; Salvador, P.; Dannenberg, J. J.; Zakrzewski, V. G.; Dapprich, S.; Daniels, A. D.; Strain, M. C.; Farkas, O.; Malick, D. K.; Rabuck, A. D.; Raghavachari, K.; Foresman, J. B.; Ortiz, J. V.; Cui, Q.; Baboul, A. G.; Clifford, S.; Cioslowski, J.; Stefanov, B. B.; Liu, G.; Liashenko, A.; Piskorz, P.; Komaromi, I.; Martin, R. L.; Fox, D. J.; Keith, T.; Al-Laham, M. A.; Peng, C. Y.; Nanayakkara, A.; Challacombe, M.; Chen, W.; Wong, M. W.; Pople, J. A.; Revision F.02 ed.; Gaussian, Inc.: Wallingford, CT, 2007.

(23) Pople, J. A.; Head-Gordon, M.; Raghavachari, K. *J. Chem. Phys.* **1987**, *87*, 5968-5975.

(24) Becke, A. D. *J. Chem. Phys.* **1993**, *98*, 1372-1377.

(25) Lee, C.; Yang, W.; Parr, R. D. *Phys. Rev. B* **1988**, *37*, 785-789.

(26) Perdew, J. P.; Burke, K.; Ernzerhof, M. *Phys. Rev. Lett.* **1996**, *77*, 3865-3868.

(27) Tao, J. M.; Perdew, J. P.; Staroverov, V. N.; Scuseria, G. E. *Phys. Rev. Lett.* **2003**, *91*, 146401.

(28) Montgomery, J. A.; Ochterski, J. W.; Peterson, G. A. *J. Chem. Phys.* **1994**, *101*, 5900-5909.

(29) Li, J.; Shaik, S.; Schlegel, H. B. *J. Phys. Chem. A* **2006**, *110*, 2801-2806.

(30) Bakken, V.; Millam, J. M.; Schlegel, H. B. *J. Chem. Phys.* **1999**, *111*, 8773-8777.

(31) Millam, J. M.; Bakken, V.; Chen, W.; Hase, W. L.; Schlegel, H. B. *J. Chem. Phys.* **1999**, *111*, 3800-3805.

(32) Stoer, J.; Bulirsch, R. *Introduction to Numerical Analysis*; Springer-Verlag: New York, 1980.

(33) Hase, W. L. In *Encyclopedia of Computational Chemistry*; Schleyer, P. v. R., Allinger, N. L., Clark, T., Gasteiger, J., Kollman, P. A., Schaefer III, H. F., Schreiner, P. R., Eds.; Wiley: Chichester, 1998; pp 402-407.

(34) Peslherbe, G. H.; Wang, H.; Hase, W. L. *Adv. Chem. Phys.* **1999**, *105*, 171-201.

CHAPTER 3

LARGE NON-STATISTICAL BRANCHING RATIO IN THE DISSOCIATION OF PENTANE-2,4-DIONE RADICAL CATION: AN AB INITIO DIRECT CLASSICAL TRAJECTORY STUDY

3.1 Introduction:

A chemically activated species can dissociate in a non-statistical manner if the rate for dissociation is faster than the rate for intramolecular energy redistribution. Acetone radical cation is an archetypal example of this process and has been studied experimentally and theoretically over the past 35 years.[1-12] Isomerization from the enol form to the keto form activates the newly formed methyl group which dissociates preferentially. Energy also flows to the other methyl group resulting in its dissociation at a slower rate and with a different energy distribution. The observed branching ratio is ca 1.5 in favor of the newly formed methyl group.[1-9,11,12] Similar to acetone radical cation, it can be anticipated that pentane-2,4-dione radical cation will also show non-statistical behavior in its dissociation. The enol form with a terminal double bond can be generated by the McLafferty rearrangement[13,14] from longer chain 2,4 diones, as shown in Scheme 3.1. Upon isomerization to the diketo form, the energy from the activated CC bond can flow sequentially to three other CC bonds, potentially resulting in greater non-statistical behavior than acetone radical cation.

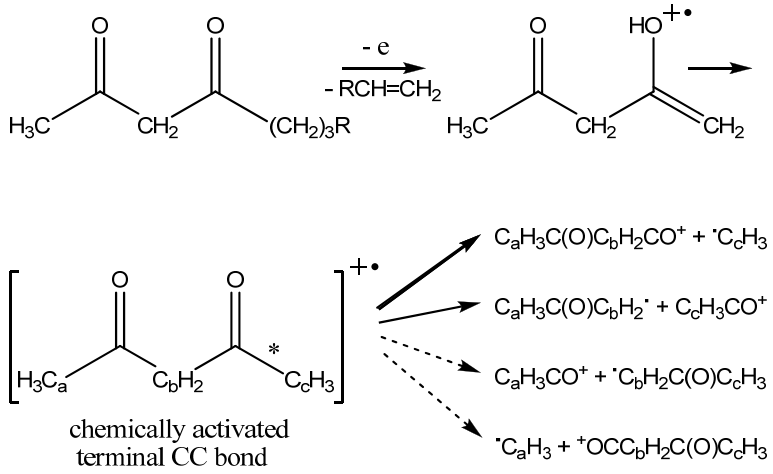

Scheme 3.1

The formation of pentane-2,4-dione radical cation has been studied experimentally[15,16], but its dissociation has not been investigated. Similar to our previous studies on acetone radical cation,[11,12] we have used ab initio classical trajectory calculations to study the non-statistical dissociation of 2,4-pentanedione radical cation. The Born-Oppenheimer molecular dynamics calculations were carried out at the MP2/6-31G(d) level of theory with bond additivity corrections fitted to the CBS-APNO energies.

3.2 Computational Methods:

The Gaussian suite of programs[17] was used for the ab initio electronic structure and molecular dynamics calculations. The geometries of the minima and the transition states were optimized by Hartree-Fock (HF), hybrid density functional theory (B3LYP),[18-20] second order Møller-Plesset perturbation theory (MP2) and quadratic configuration interaction (QCISD)[21] methods. The complete basis set extrapolation methods (CBS-QB3 and CBS-APNO) of Petersson and co-workers[22] were used to compute accurate energy differences. The CBS-

APNO calculations have a mean absolute deviation of 0.5 kcal/mol for heats of reaction.

Accurate methods such as CBS-APNO are not practical for molecular dynamics corrections. However, our calculations on the analogous dissociation of acetone radical cation[12] showed that more affordable methods such as density functional theory and MP2 do not yield sufficiently accurate energetics. The errors in such cases are often systematic, arising primarily from the making and breaking of bonds. The empirical corrections that have been used to correct computed thermochemistry[23-27] can also be employed to improve potential energy surfaces for molecular dynamics calculations.[28] As in the BAC-MP4 method,[27] a simple exponential is used to correct the potential for bond dissociations. In the present case, the bond additivity correction (BAC) is applied only to the CC bonds for the dissociation of the methyl and acetyl groups (the terminal and interior bonds, respectively):

$$\Delta E = \sum_{i=1}^{2} A_{CCinterior} \exp(-\alpha R_{CCinterior}) + \sum_{i=1}^{2} A_{CCterminal} \exp(-\alpha R_{CCterminal}) \qquad (1)$$

The parameters $A_{CCinterior}$ =0.0092 , $A_{CCterminal}$ = -0.0287 and α=0.3604 are obtained by fitting the MP2/6-31G(d) energetics to the CBS-APNO level of theory. The structures used in the fit include the diketo isomer, the enol isomer, the diketo-enol transition state, and the methyl and acetyl dissociation products (structure **1**, **7**, **TS8**, **9**, **10**). The corresponding first and second derivatives of E_{BAC} are added to gradient and Hessian. This BAC approach has been used previously to study the branching ratios in $CH_2O^{\cdot -} + CH_3Cl \rightarrow CH_3CH_2O^{\cdot} + Cl^-$, $CH_2O + CH_3^{\cdot} + Cl^-$ [28] and $CH_3COCH_3^{\cdot +} \rightarrow CH_3CO^+ + CH_3^{\cdot}$.[11,12]

Ab initio classical trajectories were computed at the BAC-MP2/6-31G(d) level of theory using a Hessian-based predictor-corrector method.[29,30] A predictor step is taken on the quadratic surface obtained from the energy, gradient and Hessian from the beginning point. A fifth order polynomial is then fitted to the energies, gradients and Hessians at the beginning and end points of the predictor step, and the Bulirsch-Stoer algorithm[31] is used to take a corrector step on this fitted surface with the angular forces projected out. The Hessians are updated for 10 steps before being recalculated analytically. The trajectories were terminated when the centers of mass of the fragments were 8 bohr apart and the gradient between the fragments was less than 1×10^{-5} hartree/bohr. A step size of 0.5 $amu^{1/2}$ bohr was used for integrating the trajectories. The energy was conserved to better than 1×10^{-5} hartree and the angular momentum was conserved to 1×10^{-8} ħ.

Trajectories were initiated at the transition state for the enol to diketo tautomerization. A microcanonical ensemble of initial states was constructed using the quasi-classical normal mode sampling.[32,33] A total energy of 10 kcal/mol above the zero point energy of the transition state was distributed among the 38 vibrational modes and translation along the transition vector toward the product. The total angular momentum was set to zero (corresponding to a rotationally cold distribution) and the phases of the vibrational modes were chosen randomly. The momentum and displacement were scaled so that the desired total energy was the sum of the vibrational kinetic energy and the potential energy obtained from the ab initio surface. The initial condition is similar

to those used previously for acetone radical cation.[11,12] A total of 244 trajectories were integrated for up to 600 *fs* starting from the transition state and ending when the products were well separated.

RRKM[34,35] calculations were used to obtain a statistical estimate of the ratio of the dissociation rates for the terminal and interior CC bonds. Variational transition states for bond breaking were approximated by extending the CC bonds and optimizing the remaining coordinates at the BAC-MP2/6-31G(d) level of theory. For the conditions corresponding to the trajectory calculations, the RRKM calculations yield ratios of 0.10 and 0.11 for the dissociation of the terminal versus interior CC bonds using bond extensions of 2.5 and 3.0 Å, respectively.

3.3 Results and Discussion

Structures and Energetics

The optimized geometries of diketo and enol forms of pentanedione radical cation, various intermediates, transition states and products are shown in Figure 3.1 for a number of levels of theory. The relative energies of these structures at the CBS-APNO level of theory are included in the figure and are summarized in Figure 3.2. In its diketo form, pentane-2,4-dione radical cation, **1**, has a planar heavy atom skeleton and belongs to the C_{2v} point group. A second diketo structure, **2**, with both carbonyl groups *syn* to the central C-H bonds lies 6.0 kcal/mol higher. A third conformer, **3**, with one carbonyl *syn* to a CC bond and the other carbonyl *syn* to a central C-H bond is 11.5 kcal/mol higher. There are two enolic forms that differ by the location of the CC double bond. The one

with an interior CC double bond, **4** (4-hydroxypent-3-en-2-one), is significantly more stable than **1** because of a very strong hydrogen bond between the OH and the carbonyl, and conjugation between the double bond and the carbonyl. At lower levels of theory, this structure is symmetrical and there is no barrier for proton transfer between the oxygens. At the QCISD/6-311G(d,p) level, the proton transfer barrier (without zero point energy) is 2.5 kcal/mol. Transition state **TS5** for tautomerization from **1** to **4** lies 43 kcal/mol above pentanedione. For the enol isomer with the terminal CC double bond (4-hydroxypent-4-en-2-one), there are two major conformers to be considered. The conformer with the OH *anti* to the CC double bond, **6**, is 11 kcal/mol more stable than the *syn* conformer, **7**, because of a strong hydrogen bond between the OH and the carbonyl. However, it is the *syn* conformer, **7**, that is connected to **1** through transition state **TS8**, which is 48 kcal/mol above pentanedione. **TS8** closely resembles the transition state for keto-enol tautomerism in acetone radical cation, both in geometry and barrier height.[11,12] The enol to diketo tautomerization of **7** via **TS8** to **1** produces a chemically activated pentanedione radical cation that can dissociate to two different sets of products. Breaking the terminal CC bond requires 33 kcal/mol and produces $CH_3C(O)CH_2CO^+$ + $CH_3^{\cdot}$, **9**. Breaking an interior CC bond cost only 27 kcal/mol and produces $CH_3C(O)CH_2^{\cdot}$ + CH_3CO^+, **10**. The $CH_3C(O)CH_2CO^+$ cation has an unusually long CC bond (1.597 Å) that is rather weak (23 kcal/mol). Breaking this bond leads to the triple dissociation product of ketene, acetyl cation and methyl radical, **11**. The triple dissociation product can also be reached by breaking the CC bond in $CH_3C(O)CH_2^{\cdot}$ radical in **10** to yield

ketene and methyl radical. The weakness of the CC bonds in pentanedione radical cation can be attributed to the stability of the cationic products, RCH_2CO^+, which are isoelectronic to $RCH_2C{\equiv}N$.

<table>
<tr>
<td> 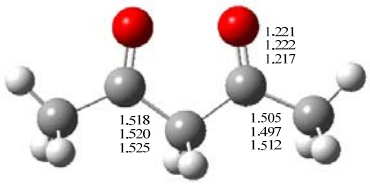

1, (0.0 kcal/mol)</td>
<td> 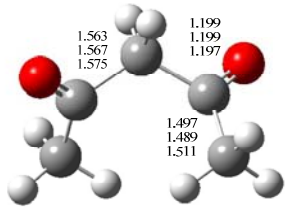

2, (6.0 kcal/mol)</td>
<td> 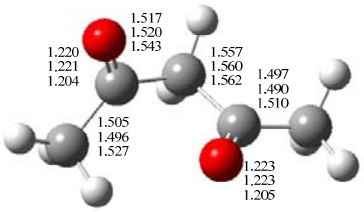

3, (11.5 kcal/mol)</td>
</tr>
<tr>
<td> 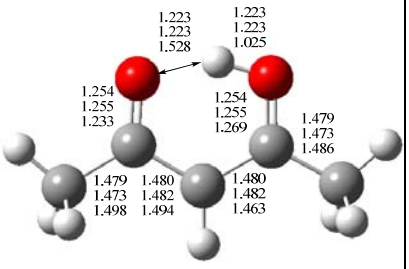

4, (-9.1 kcal/mol)</td>
<td> 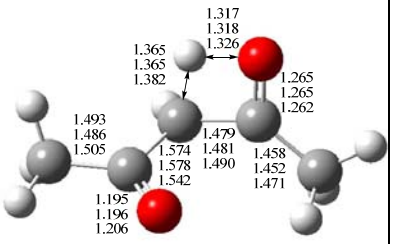

TS5, (42.8 kcal/mol)</td>
<td> 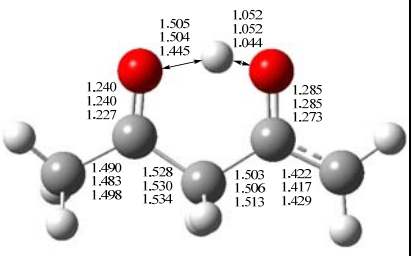

6, (-6.8 kcal/mol)</td>
</tr>
<tr>
<td> 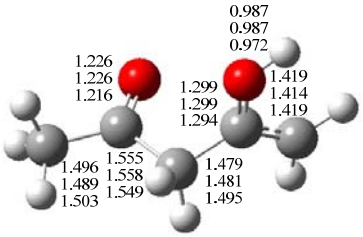

7, (3.8 kcal/mol)</td>
<td colspan="2"> 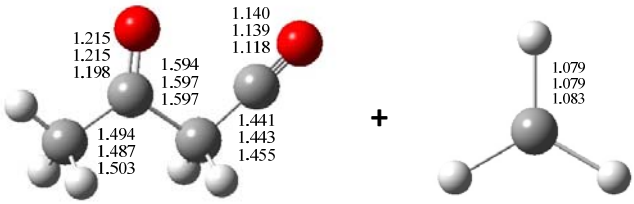

9, (33.4 kcal/mol)</td>
</tr>
</table>

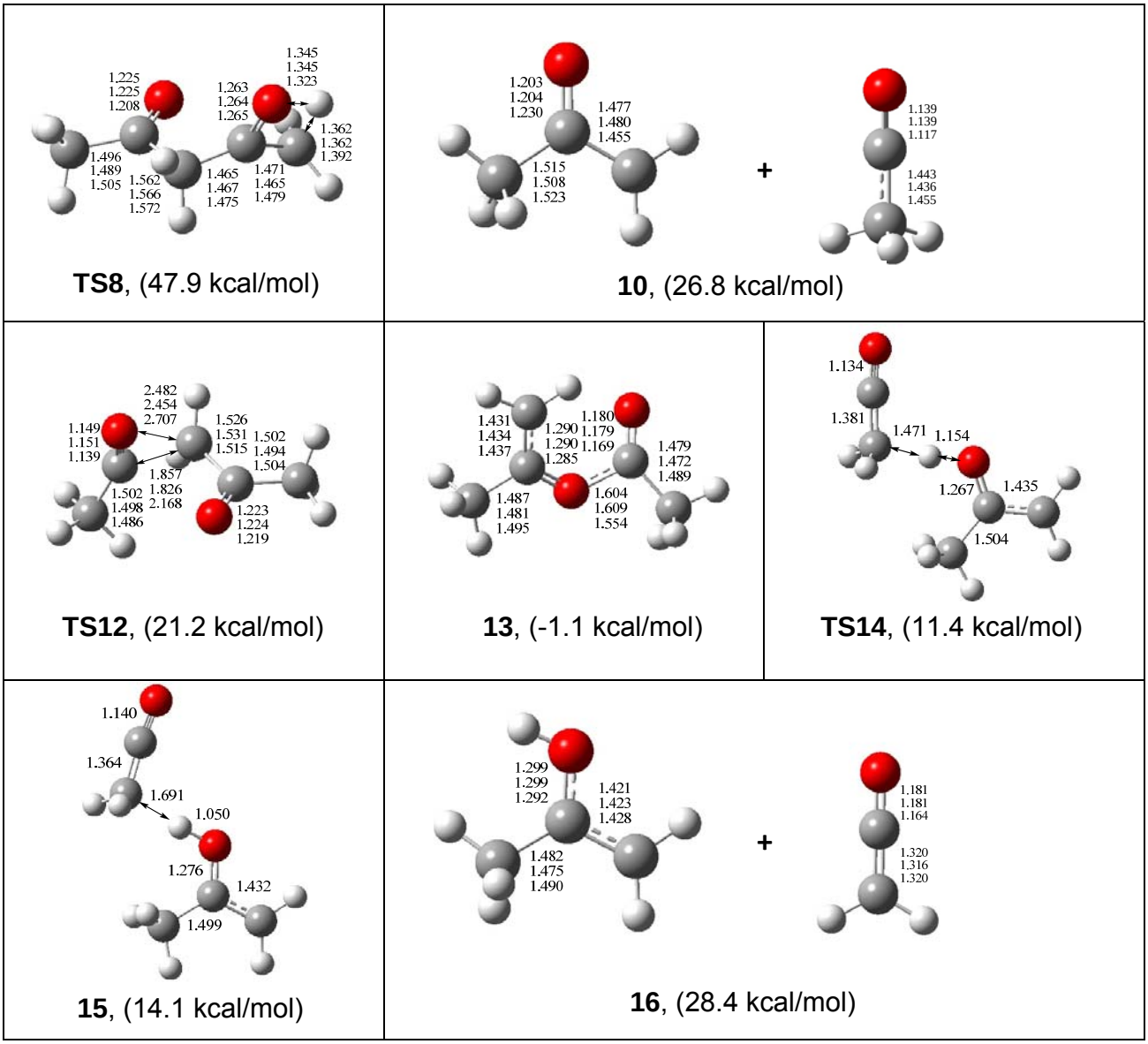

Figure 3.1 Translational energy distributions of the methyl fragments derived from the active Structures and selected geometric parameters of stationary points on the pentanedione radical cation potential energy surface optimized at the MP2/6-31G(d), BAC-MP2/6-31G(d), and QCISD/6-311G(d,p) levels of theory (top, middle and bottom rows, respectively). For **TS14** and **15**, only the QCISD/6-311G(d,p) values are listed. Bond distances are in Å. Relative energies are calculated at the CBS-APNO level of theory.

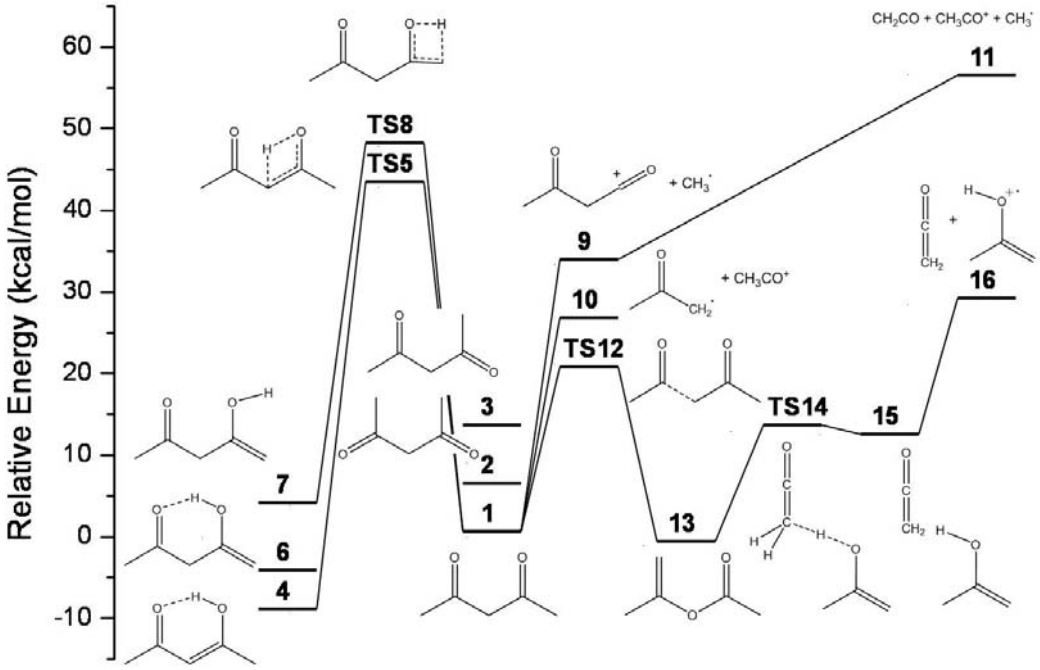

Figure 3.2 Potential energy profile for the isomerization and dissociation of the pentanedione radical cation computed at the CBS-APNO level of theory. For **TS14** and **15**, the relative energies are calculated by QCISD/6-311G(d,p) without ZPE (see text for details).

The trajectory calculations revealed a number of additional interesting structures on the pentanedione radical cation potential energy surface. Pentanedione radical cation can rearrange via **TS12** to an ester-like product, $CH_3C(CH_2)OC(O)CH_3$, **13**. This product is slightly more stable than **1** and the transition state is lower than the CC bond dissociation energies of pentanedione radical cation. A second channel revealed by the trajectory calculations involves a proton transfer via **TS14** between $CH_3C(O)CH_2^{\cdot}$ and CH_3CO^+ before they have separate completely. This produces a product complex, **15**, which dissociates to the enol of acetone radical cation and ketene, $CH_3C(OH)CH_2^{+\cdot}$ + CH_2CO, **16**. **TS14** can be optimized at QCISD/6-311G(d,p) and has an electronic energy 0.4 kcal/mol higher than **15**; however, **TS14** cannot be located at the MP2 level. When zero point energy is included, **15** is higher than **TS14**, suggesting this feature may be only a shoulder on the potential energy surface.

Table 3.1 Relative energies (in kcal/mol) of the various points on the pentanedione radical cation potential energy surface

	HF/6-31G(d)	B3LYP/6-31G(d)	MP2/6-31G(d)	CBS-QB3	CBS-APNO	BAC-MP2/6-31G(d)
1	0.0	0.0	0.0	0.0	0.0	0.0
2	14.0	10.2	8.9	9.7	6.0	8.7
3	-9.6	9.9	15.5	14.0	11.5	15.4
4	-24.2	-2.7	-7.2	-8.9	-9.1	-7.4
TS5	42.7	47.1	52.4	44.2	42.8	52.0
6	-20.7	-0.4	-8.1	-6.6	-6.8	-8.6
7	-12.3	8.6	3.5	11.3	3.8	3.0
TS8	45.4	55.4	51.2	50.8	47.9	50.9
9	11.6	43.0	25.0	34.8	33.4	31.4
10	2.2	35.7	27.7	26.9	26.8	25.5
11	33.6	66.6	51.2	56.9	56.6	46.0
TS12	10.5	25.6	19.7	22.0	21.2	19.0
13	-20.8	1.6	-6.2	-0.7	-1.1	-7.7
TS14	0.2	9.5[a]	b	12.9	11.4	b
15	0.2	10.9[a]	b	14.1	14.1	b
16	9.4	34.3	29.3	28.6	28.4	26.4

[a] using B3LYP/6-311G(d,p) geometries

[b] could not be located (see text)

The relative energies of selected stationary points on the potential energy surface have been calculated at a number of levels of theory and are compared in Table 3.1. Energies are calculated relative to pentanedione radical cation, **1**, and the CBS-APNO relative energies are taken as reference values in the comparisons. The CBS-QB3 relative energies agree quite well with the CBS-APNO values, except for the enol isomer, **7**. The CBS-QB3 calculatios are based on the B3LYP/6-311G(d,p) optimized geometries, while CBS-APNO uses QCISD/6-311G(d,p) optimized geometries. The B3LYP is relatively poor at predicting the enol geometry, while MP2 and QCISD give similar structures. If the MP2 structure is used for CBS-QB3 calculation, the relative energy of enol **7** is 4.7 kcal/mol, in better agreement with the CBS-APNO value. The Hartree-Fock calculations greatly overestimate the stability of both the enol and ester conformations, while B3LYP underestimates their stabilities compared to the CBS calculations. The barrier height for **7** $\rightarrow$ **TS8** $\rightarrow$ **1** is approximately 50 kcal/mol for all of the levels of theory. The CC bond dissociation energies (**1** $\rightarrow$ **9** and **1** $\rightarrow$ **10**) are ca 20 kcal/mol too low by Hartree-Fock and 10 kcal/mol too high by B3LYP. A variety of other density functional methods were tested for the dissociation of acetone radical cation and none was found to provide dramatically superior performance.[12] The MP2 dissociation energy for the interior CC bond is in good agreement with the CBS values, but the dissociation energy of the terminal CC bond is 8 – 10 kcal/mol too low. The MP2 values with the bond additivity correction are in good agreement with the CBS calculations for both

bonds individually. However, the rare event where both bonds break (**1** → **11**) was not included in the calibration of the bond additivity corrections, and the BAC-MP2 values are ca 10 kcal/mol too low.

Dynamics

The foregoing discussion has shown that the BAC-MP2/6-31G(d) level of theory is suitable and practical for simulating the molecular dynamics of the pentanedione radical cation dissociation. The trajectories were started at the enol to diketo transition state, **TS8**. As described in the Methods section, the initial conditions were chosen from a microcanonical ensemble with 10 kcal/mol extra energy above the zero point energy of the transition state. Of the 244 trajectories that were integrated, 6 had to be discarded because the energy was not conserved or the integration failed. Excluding these 6 trajectories, the distribution of products is shown in Table 3.2. There were 44 trajectories that returned to the enol isomer, and 9 that remained in the diketo minimum. The activated terminal CC bond dissociated in 70 trajectories producing a methyl radical. The interior CC bond adjacent to the activated terminal CC bond dissociated in 103 trajectories, leading to the loss of an acetyl cation. Only one trajectory produced dissociation of the other interior CC bond. No trajectories showed dissociation of the unactivated terminal CC bond. Two of the trajectories resulted in triple dissociation via **9**, first by losing the active methyl and then losing ketene. This fraction is probably too high because the BAC-MP2 energy is 10 kcal/mol too low for this channel. Of the 9 remaining trajectories, 5 yielded the proton transfer products, **16**, and 4 formed the ester-like product, **13**.

Table 3.2 Summary of the ab initio molecular dynamics calculations for the dissociation of pentanedione radical cation[a]

Product Structure	Description	Branching Ratio
10	loss of active acetyl	43.3%
9	loss of active methyl	29.4%
7	enol isomer	18.5%
1	diketo isomer	3.8%
16	proton transfer	2.1%
13	ester-like product	1.6%
11	triple dissociation	0.8%
10	loss of spectator acetyl	0.4%

[a] 238 trajectories integrated at the BAC-MP2/6-31G(d) level of theory starting from the diketo-enol transition state with 10 kcal/mol excess energy above ZPE in a microcannonical ensemble constructed using quasi-classical normal mode sampling

In acetone radical cation, the two CC bonds have equal bond energies and are expected to dissociate at equal rates. The observed branching ratio of ca 1.5 to 1 thus indicates significant non-statistical behavior. In pentanedione, the dissociation energy of the interior CC bond is ca 6 kcal/mol lower than the terminal CC bond. RRKM calculations indicate a ratio 0.10 – 0.11 for terminal to interior CC bond dissociation. Thus the ratio of 70:103 (0.68) for terminal to interior CC bond dissociation obtained from the trajectory calculations represents a significant deviation from statistical behavior. As in acetone radical cation, it is the result of competition between the rate of dissociation and the rate of intramolecular energy flow. An even greater deviation from statistical behavior is seen when the dissociations of the two interior CC bonds are compared. While 103 trajectories produced dissociation of the CC bond adjacent to the activated terminal CC bond, only 1 trajectory resulted in dissociation of the other interior CC bond. This gives a non-statistical branching ratio of ca 100:1. If the 9 trajectories that remained in the pentanedione minimum at the end of the simulation are assumed to dissociate via the interior CC bonds in equal proportions, the branching ratio is ca 20:1 (Scheme 3.2). This represents a very large deviation from statistical behavior, and will hopefully stimulate some experimental studies.

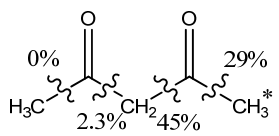

Scheme 3.2

Some additional understanding of the dissociation behavior of pentanedione radical cation can be obtained by examining the number of molecules dissociating versus time. For the purpose of this analysis, we consider a trajectory to be dissociated when the CC bond exceeds 3.0 Å and continues to lengthen. For the 70 trajectories leading to dissociation of the activated terminal CC bond within 600 *fs*, Figure 3.3 shows the logarithm of the fraction of undissociated trajectories versus time. The corresponding data is also shown for the 103 trajectories leading to dissociation of the adjacent interior CC bond. For unimolecular dissociations obeying first order kinetics, these plots should be straight lines. In the first ca. 50 *fs*, the hydrogen moves from its position in the transition state to form a C-H bond, activating the terminal methyl group, but not yet causing any CC bond dissociations. By the end of the next 50 *fs*, energy has flowed into the terminal CC bond and 50% of the trajectories leading to methyl loss have already dissociated. By contrast, only 20% of the trajectories leading to acetyl loss have dissociated. Energy continues to flow through the molecule and by 150 *fs*, 50% of the trajectories leading to acetyl loss have dissociated. Additional time is needed for energy to flow into the other interior CC bond, but the energy also flows into the remaining vibrational coordinates, approaching a statistical distribution and further reducing the dissociation probability. The average dissociated times are 152 *fs* for the active methyl group and 205 *fs* for the active acetyl group. The dissociation time for the single trajectory leading to loss of the spectator acetyl is ca 250 *fs*.

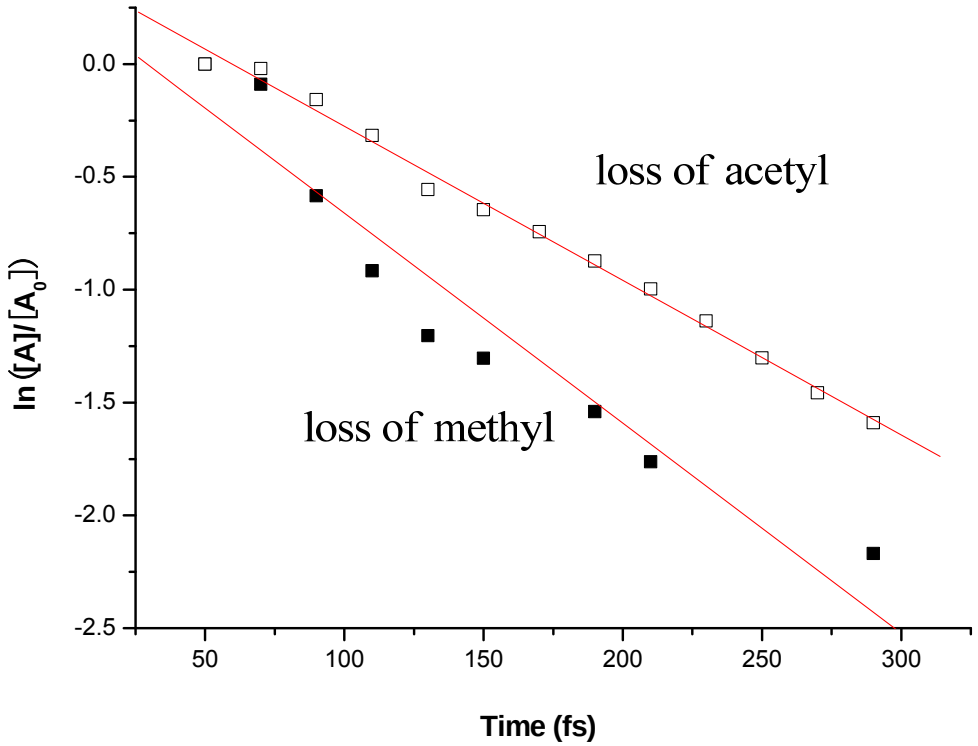

Figure 3.3 Translational Fraction of undissociated trajectories versus for loss of the active methyl group (filled symbols) and active acetyl group (open symbols).

Figure 3.3 also shows that the dissociation rate (i.e. the negative of the slope) is higher for the methyl group at earlier times than at later times. The number of methyl groups lost versus time can be fit by two exponentials starting at t_0 = 60 *fs*. The loss of acetyl is also biexponential but the effect is less pronounced. This suggests that it may be possible to model pentanedione radical cation by assuming a portion of the population dissociates rapidly, losing the active methyl and acetyl groups, and that the rest of the population responds more slowly leading to the remaining products as well as additional methyl and acetyl dissociations. A simple kinetic scheme is given in Scheme 3.3.

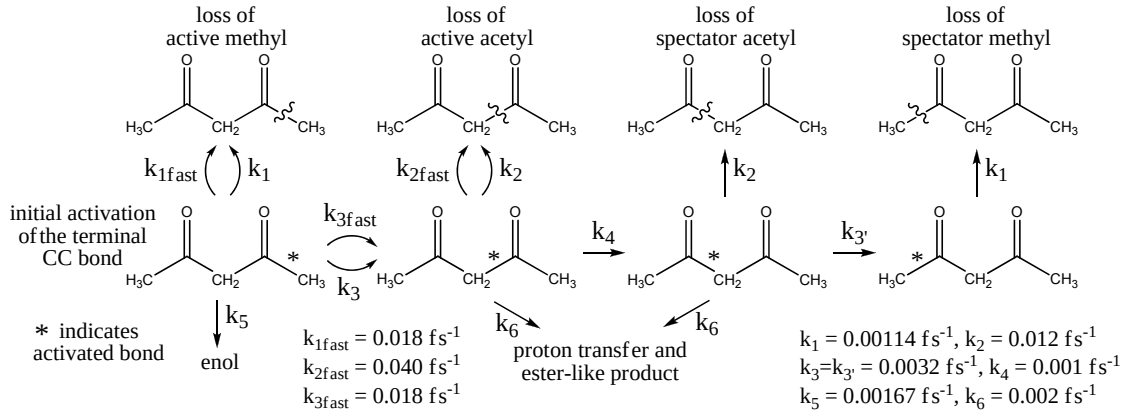

Scheme 3.3

After some testing, we assumed that 40 methyl dissociations and 40 acetyl dissociations arose from the fast mechanism and the remainders were produced by the slow mechanism. The total number of trajectories leading to each of the products imposes various constraints on the ratios of rate constants. This left four degrees of freedom which were adjusted to give the best fit to the data shown in Figure 3.4. Since other kinetic schemes and rate constants may

give equally good fits, qualitative relations among the rate constants are more relevant than their numerical values.

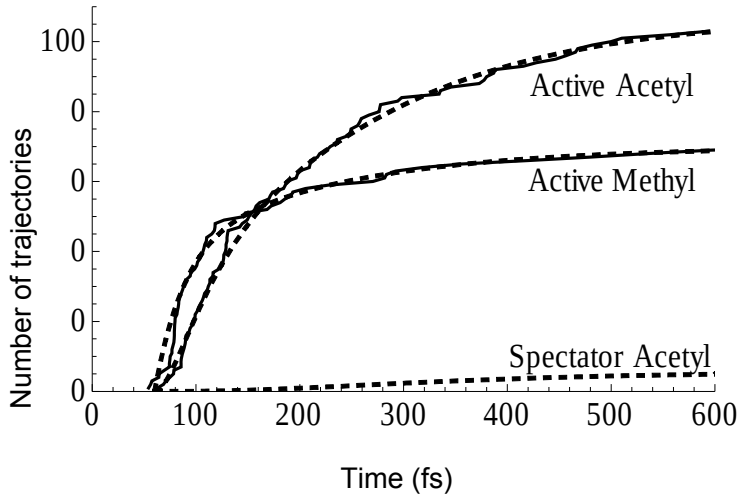

Figure 3.4 Number of dissociations of the active methyl and acetyl groups versus time obtained from the trajectory calculations (solid lines) and from the simple kinetic model (dashed lines).

Figure 3.4 shows that the data can be modeled well if one assumes a partitioning of the problem into fast and slow populations. If this assumption is not made, then the data at short times (< 150 *fs*) and longer times (> 200 *fs*) cannot both be fit by the same set of rate constants. This suggests that only some of the molecules are highly activated for dissociation by the tautomerization from enol to diketo. Both the terminal and interior bonds of the highly activated diketo species dissociate rapidly. Energy flows rapidly between the terminal and interior CC bonds, possibly mediated by CCO bending as suggested by work on the acetone radical cation system.[9,12] The rate constants for the dissociation of the slower population are governed by the behavior at longer times (> 200 *fs*). It is

satisfying to note that the ratio of the rate constants for methyl and acetyl dissociation (k_1/k_2 = 0.095) is very close to the ratio predicted by the RRKM calculations (0.10 – 0.11). The rate for energy transfer between the interior CC bonds (k_4 = 0.001) is an order of magnitude smaller than the dissociation rate for an interior CC bond. This provides a rationalization for the large non-statistical branching ratio seen for the active versus spectator acetyl group.

3.4 Conclusions:

The energetics of pentanedione radical cation dissociation have been studied by electronic structure calculations at a variety of levels of theory up to CBS-APNO. The relative energies calculated at BAC-MP2/6-31G(d) gave a better fit to the CBS-APNO results than the MP2 and B3LYP levels of theory. The dissociation of pentanedione radical cation with 10 kcal/mol extra energy above the diketo-enol transition state has been simulated by *ab initio* classical trajectories at the BAC-MP2/6-31G(d) level of theory. This produces pentanedione with chemical activation of a terminal CC bond. Dissociation of this bond yields $CH_3C(O)CH_2CO^+$ + $CH_3^{\cdot}$, but energy also flows quickly to the adjacent interior CC bond, which dissociates to give $CH_3C(O)CH_2^{\cdot}$ + CH_3CO^+. The trajectory calculations also reveal some additional products that were not anticipated. The interior CC bonds are 6 kcal/mol weaker than the terminal CC bonds, and RRKM theory predicts a branching ratio of 0.10 – 0.11 for the breaking of the terminal CC versus the interior CC bond. However, the simulations yield a branching ratio of 0.68, indicating a substantial deviation from statistical behavior. An even larger deviation from statistical behavior is seen for

the dissociation of the two equivalent interior CC bonds, with a branching ratio of ca. 20:1 or greater. The biexponential behavior of the dissociations indicates that a fraction of the activated pentanedione radical cations reacts more rapidly. A simple kinetic scheme has been constructed to model the dissociation rates. The non-statistical behavior is seen in the dissociations because the rate of energy flow within the molecule is comparable to or slower than the rates of dissociation.

3.5 References

(1) Depke , G.; Lifshitz , C.; Schwarz, H.; Tzidony, E. *Angew. Chem. Int. Edit.* **1981**, *20*, 792-793.

(2) McAdoo, D. J.; Hudson, C. E. *Int. J. Mass Spectrom. Ion Proc.* **1984**, *59*, 77-83.

(3) McAdoo, D. J.; McLafferty, F. W.; Smith, J. S. *J. Am. Chem. Soc.* **1970**, *92*, 6343-6345.

(4) Turecek, F.; Hanus, V. *Org. Mass Spectom.* **1984**, *19*, 631-638.

(5) Heinrich, N.; Louage, F.; Lifshitz, C.; Schwarz, H. *J. Am. Chem. Soc.* **1988**, *110*, 8183-92.

(6) Lifshitz , C. *J. Phys. Chem.* **1983**, *87*, 2304-2313.

(7) Lifshitz, C.; Tzidony, E. *Int. J. Mass Spectrom. Ion Phys.* **1981**, *39*, 181-95.

(8) Lifshitz, C.; Tzidony, E.; Terwilliger, D. T.; Hudson, C. E. *Adv. Mass Spectrom.* **1980**, *8A*, 859-66.

(9) Osterheld, T. H.; Brauman, J. I. *J. Am. Chem. Soc.* **1993**, *115*, 10311-16.

(10) Nummela, J. A.; Carpenter, B. K. *J. Am. Chem. Soc.* **2002**, *124*, 8512-8513.

(11) Anand, S.; Schlegel, H. B. *Phys. Chem. Chem. Phys.* **2004**, *6*, 5166-5171.

(12) Zhou, J.; Schlegel, H. B. *J. Phys. Chem. A* **2008**, *112*, 13121–13127.

(13) Gilpin, J. A., McLafferty, F. W. *Anal. Chem.* **1957**, *29*, 990-994.

(14) McLafferty, F. W. *Anal. Chem.* **1959**, *31*, 82-87.

(15) Nuzhdin, K. B.; Feldman, V. I.; Kobzarenko, A. V. *J. Phys. Chem. A* **2007**, *111*, 3294-3301.

(16) Hush, N. S.; Livett, M. K.; Peel, J. B.; Willett, G. D. *Aust. J. Chem.* **1987**, *40*, 599-609.

(17) Frisch, M. J.; Trucks, G. W.; Schlegel, H. B.; Scuseria, G. E.; Robb, M. A.; et al.; Revision F.02 ed.; Gaussian, Inc.: Wallingford, CT, 2007.

(18) Becke, A. D. *J. Chem. Phys.* **1993**, *98*, 1372-1377.

(19) Becke, A. D. *J. Chem. Phys.* **1993**, *98*, 5648-5652.

(20) Lee, C.; Yang, W.; Parr, R. D. *Phys. Rev. B* **1988**, *37*, 785-789.

(21) Pople, J. A.; Head-Gordon, M.; Raghavachari, K. *J. Chem. Phys.* **1987**, *87*, 5968-5975.

(22) Montgomery, J. A.; Ochterski, J. W.; Peterson, G. A. *J. Chem. Phys.* **1994**, *101*, 5900-5909.

(23) Allendorf, M. D.; Melius, C. F. *J. Phys. Chem. A* **2005**, *109*, 4939-4949.

(24) Anantharaman, B.; Melius, C. F. *J. Phys. Chem. A* **2005**, *109*, 1734-1747.

(25) Ho, P.; Coltrin, M. E.; Binkley, J. S.; Melius, C. F. *J. Phys. Chem.* **1985**, *89*, 4647-4654.

(26) Melius, C. F.; Allendorf, M. D. *J. Phys. Chem. A* **2000**, *104*, 2168-2177.

(27) Ho, P.; Melius, C. F. *J. Phys. Chem.* **1990**, *94*, 5120-5127.

(28) Li, J.; Shaik, S.; Schlegel, H. B. *J. Phys. Chem. A* **2006**, *110*, 2801-2806.

(29) Bakken, V.; Millam, J. M.; Schlegel, H. B. *J. Chem. Phys.* **1999**, *111*, 8773-8777.

(30) Millam, J. M.; Bakken, V.; Chen, W.; Hase, W. L.; Schlegel, H. B. *J. Chem. Phys.* **1999**, *111*, 3800-3805.

(31) Stoer, J.; Bulirsch, R. *Introduction to Numerical Analysis*; Springer-Verlag: New York, 1980.

(32) Hase, W. L. In *Encyclopedia of Computational Chemistry*; Schleyer, P. v. R., Allinger, N. L., Clark, T., Gasteiger, J., Kollman, P. A., Schaefer III, H. F., Schreiner, P. R., Eds.; Wiley: Chichester, 1998, p 402-407.

(33) Peslherbe, G. H.; Wang, H.; Hase, W. L. *Adv. Chem. Phys.* **1999**, *105*, 171-201.

(34) Marcus, R. A.; Rice, O. K. *J. Phys. Chem.* **1951**, *55*, 894-908.

(35) Steinfeld, J. I.; Francisco, J. S.; Hase, W. L. In *Chemical Kinetics and Dynamics*; Prentice-Hall: Upper Saddle River, NJ, 1999.

CHAPTER 4

AB INITIO CLASSICAL TRAJECTORY CALCULATIONS OF 1,3-CYCLOBUTANEDIONE RADICAL CATION DISSOCIATION

4.1 Introduction:

A chemically activated species can dissociate in a non-statistical manner if the rate for dissociation is faster than the rate for intramolecular energy redistribution. Acetone radical cation is an archetypal example of this process and has been studied experimentally and theoretically over the past 35 years.[1-12] Isomerization from the enol form to the keto form activates the newly formed methyl group which dissociates preferentially. Energy also flows to the other methyl group resulting in its dissociation at a slower rate and with a different energy distribution. The observed branching ratio is ca 1.5:1 in favor of the newly formed methyl group.[1-9,11,12] Similar to acetone radical cation, in our ab initio MD study of pentane-2,4-dione radical cation,[13] we saw a competition between thermodynamics and non-statistical behavior in C-C bond dissociation. The activated terminal C-C bond had a lower dissociation probability than the weaker neighboring C-C bond. The two interior C-C bonds are equal in strength, but the one closer to the activated bond dissociates ca 20 times more frequently. Based on the above studies, it would be interesting to design a chemically activated system that would allow the flow of energy through several bonds of equal strength, thereby avoiding any thermodynamic bias. 1,3-cyclobutanedione radical cation could be a good candidate. The enol form with a C-C double bond can be generated by the McLafferty rearrangement,[14,15] as shown in Scheme 4.1. Upon isomerization to the

diketo form, the energy from the activated C-C bond can flow sequentially to three other C-C bonds, potentially resulting in greater variety of non-statistical behavior than acetone radical cation.

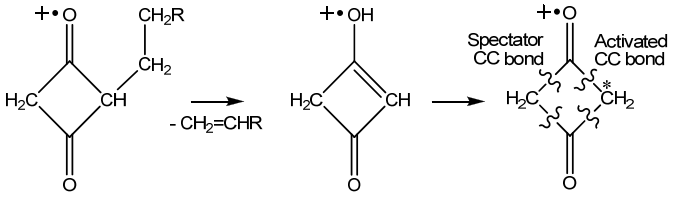

Scheme 4.1

4.2 Computational Methods:

Similar to our previous studies on acetone radical cation[11,12] and pentanedione radical cation,[13] we have used ab initio classical trajectory calculations to study the non-statistical dissociation of 1,3-cyclobutanedione radical cation. The Gaussian suite of programs[16] was used for the ab initio electronic structure and molecular dynamics calculations. The geometries of the minima and transition states were optimized by Hartree-Fock (HF), hybrid density functional theory (B3LYP and BH&HLYP),[17-19] and second order Møller-Plesset perturbation theory (MP2).[20] Higher accurate energy differences were calculated by the CBS-QB3[21] and G4[22] methods. The G4 calculations have a mean absolute deviation of 0.83 kcal/mol for heats of reaction and thus will be used as a standard.

Ab initio classical trajectories were computed at the BH&HLYP/6-31G(d) level of theory using a Hessian-based predictor-corrector method.[23,24] The trajectories were terminated when the centers of mass of the fragments were 8 bohr apart and the gradient between the fragments was less than 1×10^{-5} hartree/bohr. A step size of 0.25 amu$^{1/2}$ bohr was used for integrating the

trajectories. The energy was conserved to better than 1×10^{-5} hartree and the angular momentum was conserved to 1×10^{-8} ħ. Trajectories were initiated at the transition state for the enol to diketo tautomerization. A microcannonical ensemble of initial states was constructed using quasi-classical normal mode sampling.[26,27] A total energy of 10 kcal/mol above the zero point energy of the transition state was distributed among the 23 vibrational modes and translation along the transition vector toward the product. The total angular momentum was set to zero (corresponding to a rotationally cold distribution) and the phases of the vibrational modes were chosen randomly. The initial conditions are similar to those used previously for acetone radical cation[11,12] and pentanedione radical cation[13]. A total of 210 trajectories were integrated for up to 400 *fs* starting from the transition state and ending when the products were well separated.

4.3 Results and Discussion

Structures and Energetics

The optimized geometries of the diketo and enol forms of cyclobutanedione radical cation, various intermediates, transition states and products are available in Figure 4.1 for a number of levels of theory. The relative energies of these structures at the G4 level of theory are summarized in Figure 4.2. In its diketo form, 1,3-cyclobutanedione radical cation, **1**, has D_{2h} symmetry with a planar heavy atom skeleton. The enolic form, **3**, also has a planar heavy atom skeleton, and lies 4.1 kcal/mol higher in energy than **1**. The enol to diketo tautomerization of **3** via **TS2** to **1** produces a chemically activated cyclobutanedione radical cation. Breaking one CC bond requires only 6.6

kcal/mol and produces $CH_2C(O)CH_2CO^{+\cdot}$, **5**. Because of the release of ring strain, **5** is 14.6 kcal/mol more stable than **1**. Two CC dissociation paths lead from **5** to products with similar energies. One path yields $CH_2C(O)CH_2^{+\cdot}$ + CO, **6**, and requires 33.4 kcal/mol. The other path produces $CH_2CO^{+\cdot}$ + CH_2CO, **9**, via transition state **TS7** and intermediate **8**, and requires 30.6 kcal/mol. The central CC bond in complex **8** is a 3 electron bond and is very long (ca 2.4 Å). Nevertheless, it has a dissociation energy of 20.7 kcal/mol. Similar to our previous study on pentanedione radical cation[13], a proton transfer can occur between the products. This process happens via complex **10**, transition state **TS11** and complex **12**. The product CH_3CO^{+} + $HCCO^{\cdot}$, **13**, is only 2 kcal/mol higher than **9**.

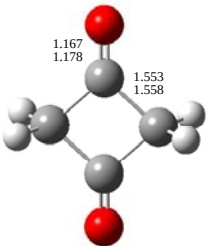

1, (-16.0)

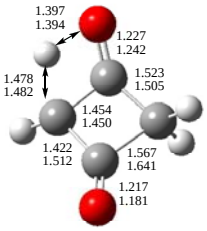

TS2, (56.8)

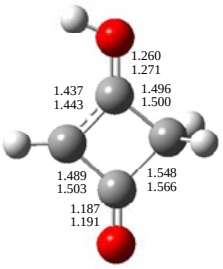

3, (-11.19)

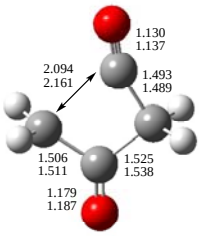

TS4, (-9.4)

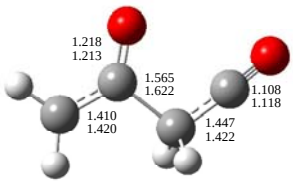

5, (-30.6)

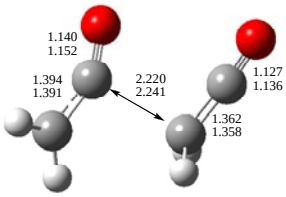

TS7, (-13.5)

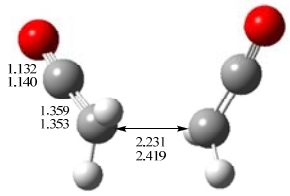

8, (-20.7)

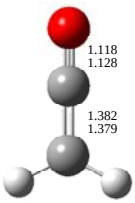

+

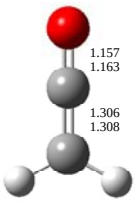

9, (0.0)

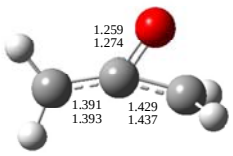

+

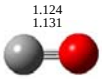

6, (2.8)

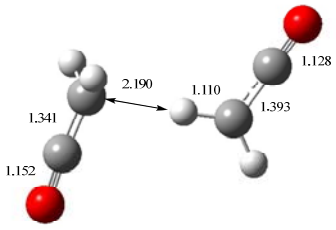

10, (-7.5)

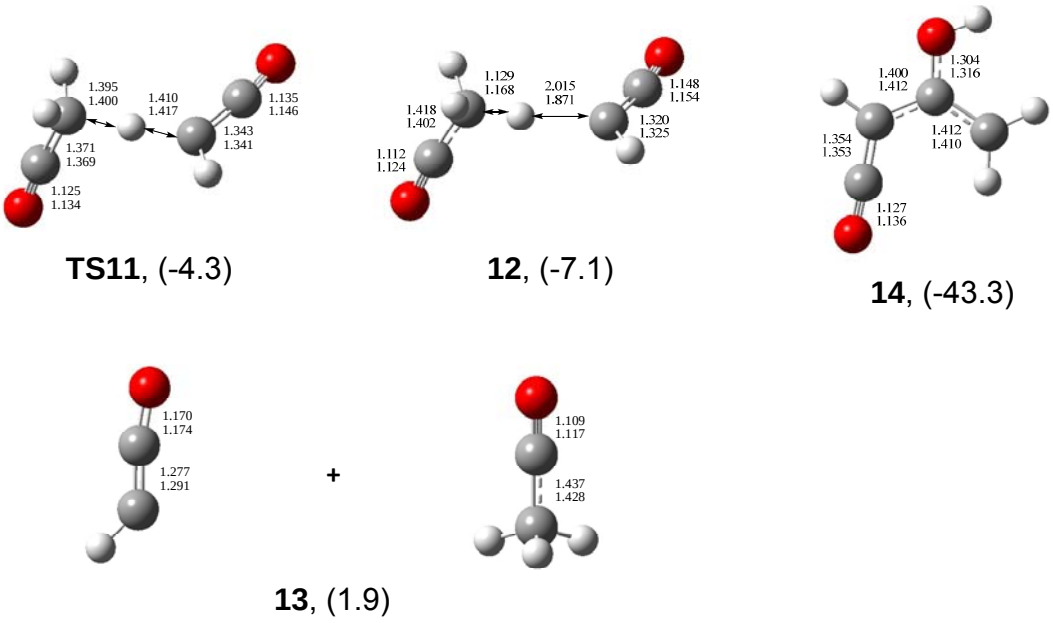

Figure 4.1 Structures and selected geometric parameters of stationary points on the cyclobutanedione radical cation potential energy surface optimized at the BH&HLYP/6-31G(d) and G4 (B3LYP/6-31G(2df,p)) levels of theory (top and bottom rows, respectively). For structure **10**, QCISD/6-311G(d) value is listed. Bond distances are in angstroms. Relative energies in kcal/mol (given in parentheses) were calculated at the G4 level of theory.

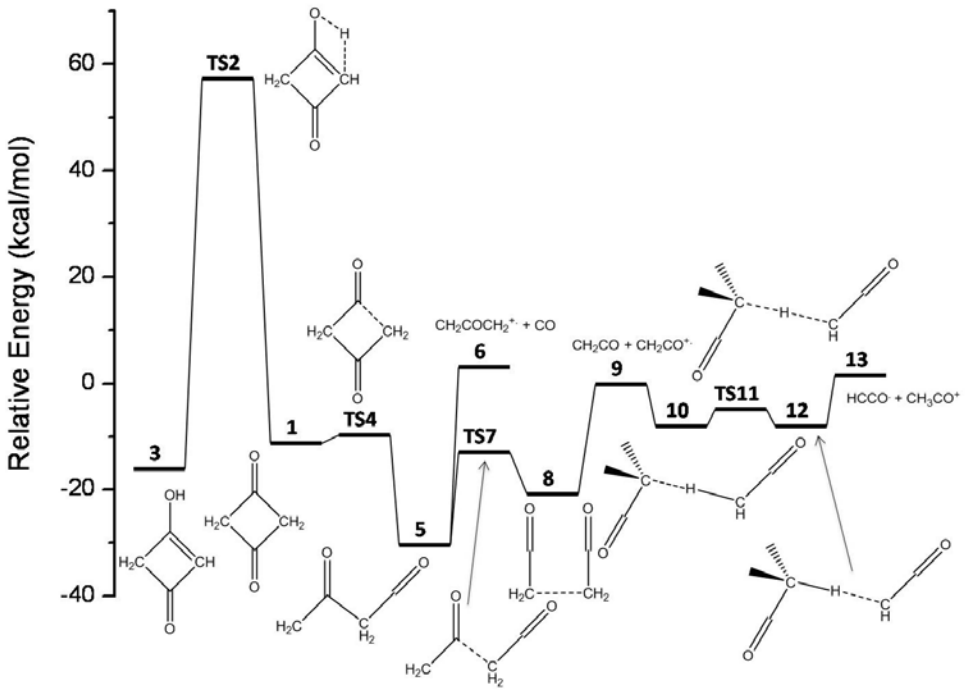

Figure 4.2 Potential energy profile for the isomerization and dissociation of cyclobutanedione radical cation computed at the G4 level of theory.

The relative energies of selected stationary points on the potential energy surface have been computed at a number of levels of theory and are compared in Table 4.1. Energies are calculated relative to $CH_2CO^{+\cdot}$ + CH_2CO, **9**, and the G4 relative energies are taken as reference values in the comparisons. As expected, the CBS-QB3 relative energies agree well with the G4 values, with mean average deviation (MAD) of 1.0 kcal/mol. The B3LYP and MP2 perform similarly at predicting the relative energies (4 kcal/mol MAD) except that MP2 fails to locate the **TS4** structure. The Hartree-Fock calculations greatly underestimate the stability of **1**, **TS2** and **8** relative to **9**, and fail to locate structure **12**. Since the DFT methods were not able to locate structure **10**, QCISD geometries were used instead. The BH&HLYP values are in excellent agreement with the G4 values (MAD of 1.9 kcal/mol) and are used for the molecular dynamics simulations.

Table 4.1 Relative Energies (kcal/mol) of Various Points on the Cyclobutanedione Radical Cation Potential Energy Surface

	HF/ 6-31G(d)	B3LYP/ 6-31G(d)	MP2/ 6-31G(d)	BH&HLYP/ 6-31G(d)	CBS-QB3	G4
1	7.8	-24.4	-21.3	-18.6	-20.0	-16.0
TS2	75.7	51.4	72.3	60.3	54.3	56.8
3	-10	-13.6	-3.5	-18.3	-12.6	-11.9
TS4	1.8	-11.9	-9.7[a]	-10.8	-8.3	-9.4
5	-31.9	-30	-28.3	-33.3	-30.2	-30.6
6	-1.9	4.1	-0.4	1.2	3.6	2.8
TS7	-4.4	-18.7	-18.2	-14.7	-12.1	-13.5
8	-6.0	-27.9	-25.9	-21.9	-21.5	-20.7
9	0.0	0.0	0.0	0.0	0.0	0.0
10	-4.1	-13.4[a]	-8.6	-8.4[a]	-6.5[b]	-7.5[b]
TS11	6.5	-11.1	-6.5	-5.2	-3.5	-4.3
12	[c]	-10.4	-8.6	-6.8	-6.4	-7.1
13	5.1	2.6	2.8	3.8	2.1	1.9
14	-36.9	-44.3	-42.2	-45.6	-43.2	-43.3
MAD	8.4	3.6	3.7	1.9	1.0	

[a] Single point energy at QCISD/6-311G(d) geometry plus QCISD/6-311(d) ZPE

[b] Using QCISD/6-311G(d) geometry

[c] Stationary point could not be located

Dynamics

The trajectories were started at the enol to diketo transition state, **TS2** with initial conditions chosen from a microcanonical ensemble with 10 kcal/mol extra energy above the zero point energy of the transition state. Of the 210 trajectories that were integrated, 7 had to be discarded because the energy was not conserved or the integration failed. Excluding these 7 trajectories, the distribution of products is shown in Table 4.2. The enol to diketo reaction produces cyclobutanedione radical cation with an activated CC bond. To be consistent with acetone radical cation, we designate the CC bond separated from the activated bond by a carbonyl group as the spectator CC bond. The activated CC bond, along with the CC bond opposite to it, dissociated in 93 trajectories producing $CH_2CO^{+\cdot}$ + CH_2CO, **9**. The spectator CC bond and the CC bond opposite it dissociated in 50 trajectories. Four trajectories remained in the diketo minimum. There were 20 trajectories that did not reach the diketo minimum but crossed back to the enol isomer; 15 of these trajectories ended with breaking of a CC bond to form $CH_2C(OH)CHCO^{+\cdot}$, **14**. Two trajectories yielded proton transfer products, **13**. Another two trajectories lost CO producing $CH_2COCH_2^{+\cdot}$ + CO, **6** (one for each carbonyl group). Several trajectories stop after one CC bond breaking, yielding $CH_2COCH_2CO^{+\cdot}$, **5**. Of the four possibilities for breaking one CC bond, the activated CC bond broke most frequently (17 trajectories), followed by the spectator CC bond (7 trajectories) and the other two bonds (4 trajectories each).

Table 4.2 Branching Ratios for Cyclobutanedione Radical Cation Dissociation from Molecular Dynamics at the BH&HLYP/6-31G(d) Level of Theory

Product Structure	Description	Number of Trajectories	Percentages (%)
9	active bond dissociation	93	45.8
9	spectator bond dissociation	50	24.6
5	active bond dissociation	17	8.4
5	spectator bond dissociation	7	3.4
5	opposite bond dissociation	8	4.0
6	CO elimination	2	1.0
13	proton transfer	2	1.0
14	$CH_2C(OH)CHCO^{+\cdot}$	15	7.5
1	cyclobutanedione radical cation	4	2.0
3	enol isomer	5	2.5

In acetone radical cation, the two CC bonds have equal bond energies and are expected to dissociate at equal rates. The observed branching ratio of ca 1.5 to 1 thus indicates significant non-statistical behavior. In pentanedione, the active versus spectator bond dissociation ratio is complicated by differences in the bond strengths. Nevertheless, comparison with RRKM calculation indicates significant non-statistical behavior. The situation is simpler for cyclobutanedione radical cation, since all of the CC bonds have the same dissociation energy. There are two ways to produce $CH_2CO^{+\cdot}$ + CH_2CO, **9**, depending on whether the active CC bond or spectator CC bond breaks. Statistically they would be expected to have the same dissociate rate, but the molecular dynamics calculations yield a ratio of 93:50 = 1.86 for active versus spectator CC bond dissociation. This is a greater deviation from statistical behavior than for acetone radical cation with the same initial conditions. As in acetone radical cation, it is the result of competition between the rate of dissociation and the rate of intramolecular energy flow. Hopefully, these calculations will stimulate experimental studies on the non-statistical behavior of cyclobutanedione radical cation and related systems such as pentanedione radical cation.

4.4 Conclusions:

The dissociation of 1,3-cyclobutanedione radical cation was studied by ab initio direct classical trajectory calculations at the BH&HLYP/6-31G(d) level of theory. A microcanonical ensemble using quasiclassical normal mode sampling was constructed by distributing 10 kcal/mol of excess energy above the transition state for the tautomerization of the enol to the diketo form. A total of 210

trajectories were run starting from this transition state, yielding chemically activated 1,3-cyclobutanedione radical cation. The majority of the trajectories resulted in $CH_2CO^{+\cdot}$ + CH_2CO, with the activated CC bond breaking nearly twice as often as the spectator CC bond. The non-statistical behavior is observed because the rate of energy redistribution within the molecule is comparable to or slower than the dissociation rates. In addition to the expected products, dissociation to $CH_2COCH_2^{+\cdot}$ + CO and formation a proton transferred product, $HCCO^{\cdot}$ + CH_3CO^{+} were also seen in some of the trajectories.

4.5 References

(1) Depke , G.; Lifshitz , C.; Schwarz, H.; Tzidony, E. Non-Ergodic Behavior of Excited Radical Cations in the Gas Phase. *Angew. Chem. Int. Ed.* **1981**, 20, 792-793.

(2) McAdoo, D. J.; Hudson, C. E. Non-ergodic dissociation of the acetone/enol ion. *Int. J. Mass Spectrom. Ion Processes* **1984**, 59, 77-83.

(3) McAdoo, D. J.; McLafferty, F. W.; Smith, J. S. Ketonization of Gaseous enol ions. *J. Am. Chem. Soc.* **1970**, 92, 6343-6345.

(4) Turecek, F.; Hanus, V. Loss of methyl from $[H_2C{:}C(OH){-}CH_3]^{+\cdot}$ ions prepared by electron impact ionization of unstable 2-hydroxypropene. *Organ. Mass Spectom.* **1984**, 19, 631-638.

(5) Heinrich, N.; Louage, F.; Lifshitz, C.; Schwarz, H. Competing reactions of the acetone cation radical: RRKM-QET calculations on an ab initio potential-energy surface. *J. Am. Chem. Soc.* **1988**, 110, 8183-8192.

(6) Lifshitz, C.; Tzidony, E. Kinetic energy release distributions for $C_3H_6O^{+\cdot}$ ion dissociations: a further test of the applicability of the energy-randomization hypothesis to unimolecular fragmentations. *Int. J. Mass Spectrom. Ion Physics* **1981**, 39, 181-195.

(7) Lifshitz , C. Intramolecular energy redistribution in polyatomic ions. *J. Phys. Chem.* **1983**, 87, 2304-2313.

(8) Lifshitz, C.; Tzidony, E.; Terwilliger, D. T.; Hudson, C. E. MIKE spectra of the McLafferty rearrangement ion from 2-ketones. *Adv. Mass Spectrom.* **1980**, 8A, 859-866.

(9) Osterheld, T. H.; Brauman, J. I. Infrared multiple-photon dissociation of the acetone enol radical cation. Dependence of nonstatistical dissociation on internal energy. *J. Am. Chem. Soc.* **1993**, 115, 10311-10316.

(10) Nummela, J. A.; Carpenter, B. K. Nonstatistical Dynamics in Deep Potential Wells: A Quasiclassical Trajectory Study of Methyl Loss from the Acetone Radical Cation. *J. Am. Chem. Soc.* **2002**, 124, 8512-8513.

(11) Anand, S.; Schlegel, H. B. Dissociation of acetone radical cation ($CH_3COCH_3^{+\cdot} \rightarrow CH_3CO^+ + CH_3^{\cdot}$): An ab initio direct classical trajectory study. *Phys. Chem. Chem. Phys.* **2004**, 6, 5166-5171.

(12) Zhou, J.; Schlegel, H. B. Dissociation of Acetone Radical Cation ($CH_3COCH_3^{+\cdot} \rightarrow CH_3CO^+ + CH_3^{\cdot}$): An Ab Initio Direct Classical Trajectory Study of the Energy Dependence of the Branching Ratio. *J. Phys. Chem. A* **2008**, 112, 13121-13127.

(13) Zhou, J.; Schlegel, H. B. Large Nonstatistical Branching Ratio in the Dissociation of Pentane-2,4-dione Radical Cation: An Ab Initio Direct Classical Trajectory Study. *J. Phys. Chem. A* **2009**, 113, 1453-1458.

(14) Gilpin, J. A., McLafferty, F. W. Mass spectrometric analysis of aliphatic aldehydes. *Anal. Chem.* **1957**, 29, 990-994.

(15) McLafferty, F. W. Mass Spectrometric Analysis. Molecular Rearrangements. *Anal. Chem.* **1959**, 31, 82-87.

(16) Frisch, M. J.; Trucks, G. W.; Schlegel, H. B.; Scuseria, G. E.; Robb, M. A.; Cheeseman, J. R.; Montgomery, J. A., Jr.; Vreven, T.; Scalmani, G.; Mennucci, B.; Barone, V.; Petersson, G. A.; Caricato, M.; Nakatsuji, H.; Hada, M.; Ehara, M.; Toyota, K.; Fukuda, R.; Hasegawa, J.; Ishida, M.; Nakajima, T.; Honda, Y.; Kitao, O.; Nakai, H.; Li, X.; Hratchian, H. P.; Peralta, J. E.; Izmaylov, A. F.; Kudin, K. N.; Heyd, J. J.; Brothers, E.; Staroverov, V.; Zheng, G.; Kobayashi, R.; Normand, J.; Sonnenberg, J. L.; Iyengar, S. S.; Tomasi, J.; Cossi, M.; Rega, N.; Burant, J. C.; Millam, J. M.; Klene, M.; Knox, J. E.; Cross, J. B.; Bakken, V.; Adamo, C.; Jaramillo, J.; Gomperts, R.; Stratmann, R. E.; Yazyev, O.; Austin, A. J.; Cammi, R.; Pomelli, C.; Ochterski, J. W.; Ayala, P. Y.; Morokuma, K.; Voth, G. A.; Salvador, P.; Dannenberg, J. J.; Zakrzewski, V. G.; Dapprich, S.; Daniels, A. D.; Strain, M. C.; Farkas, O.; Malick, D. K.; Rabuck, A. D.; Raghavachari, K.; Foresman, J. B.; Ortiz, J. V.; Cui, Q.; Baboul, A. G.; Clifford, S.; Cioslowski, J.; Stefanov, B. B.; Liu, G.; Liashenko, A.; Piskorz, P.; Komaromi, I.; Martin, R. L.; Fox, D. J.; Keith, T.; Al-Laham, M. A.; Peng, C. Y.; Nanayakkara, A.; Challacombe, M.; Chen, W.; Wong, M. W.; Pople, J. A.; Revision F.02 ed.; Gaussian, Inc.: Wallingford, CT, 2007.

(17) Becke, A. D. A new mixing of Hartree-Fock and local density-functional theories. *J. Chem. Phys.* **1993**, 98, 1372-1377.

(18) Becke, A. D. Density functional theory. III. The role of exact exchange. *J. Chem. Phys.* **1993**, 98, 5648-5652.

(19) Lee, C.; Yang, W.; Parr, R. D. Development of the Colle-Salvetti correlation energy formula into a functional of the electron density. *Phys. Rev. B* **1988**, 37, 785-789.

(20) Moller, C.; Plesset, M. S. Note on an Approximation Treatment for Many-Electron Systems. *Phys. Rev.* **1934**, 46, 618-622.

(21) Montgomery, J. A.; Ochterski, J. W.; Peterson, G. A. A complete basis set model chemistry. IV. An improved atomic pair natural orbital method. *J. Chem. Phys.* **1994**, 101, 5900-5909.

(22) Larry, A. C.; Paul, C. R.; Krishnan, R. Gaussian-4 theory. *J. Chem. Phys.* **2007**, 126, 084108.

(23) Bakken, V.; Millam, J. M.; Schlegel, H. B. Ab Initio classical trajectories on the Born-Oppenheimer surface: Updating methods for Hessian-based integrators. *J. Chem. Phys.* **1999**, 111, 8773-8777.

(24) Millam, J. M.; Bakken, V.; Chen, W.; Hase, W. L.; Schlegel, H. B. Ab Initio classical trajectories on the Born-Oppenheimer surface: Hessian-based integrators using fifth-order polynomial and rational function fits. *J. Chem. Phys.* **1999**, 111, 3800-3805.

(25) Stoer, J.; Bulirsch, R. Introduction to Numerical Analysis; Springer-Verlag: New York, 1980.

(26) Hase, W. L. In Encyclopedia of Computational Chemistry; Schleyer, P. v. R., Allinger, N. L., Clark, T., Gasteiger, J., Kollman, P. A., Schaefer III, H. F., Schreiner, P. R., Eds.; Wiley: Chichester, 1998, p 402-407.

(27) Peslherbe, G. H.; Wang, H.; Hase, W. L. Monte Carlo sampling for classical trajectory simulations. *Adv. Chem. Phys.* **1999**, 105, 171-201

CHAPTER 5

AB INITIO CLASSICAL TRAJECTORY STUDY OF THE DISSOCIATION OF NEUTRAL AND POSITIVELY CHARGED METHANIMINE (CH_2NH^{n+} n=0,1,2)

5.1 Introduction:

The simplest example of a molecule with a carbon-nitrogen double bond is H_2C=NH, known variously as methanimine, methyleneimine and formaldimine. Similar to ethylene and formaldehyde, the simplest examples of CC and CO double bonds, the low energy dissociation channels of H_2CNH are loss of hydrogen atom and elimination of molecular H_2. Ionization to form the monocation simplifies the potential energy surface and reduces the barriers to rearrangement and dissociation. Formation of the dication favors dissociation into two monocations and should reduce the barriers further. When a third electron is removed, the barriers are less than 5 kcal/mol (see below) and the molecule dissociates via a Coulomb explosion. In the present paper we use accurate computational methods to explore the potential energy surfaces of H_2CNH and its cations and use ab initio classical trajectory calculations to examine the molecular dynamics of these systems.

Neutral H_2CNH is a reactive intermediate that can be produced by pyrolysis of amines and azides.[1-5] It has also been observed in interstellar dust clouds.[6] The gas phase structure has been determined by microwave spectroscopy.[1] The infrared spectrum has been observed in early matrix isolation

experiments[7,8] and later in the gas phase.[3,9-12] The electronic spectrum of H_2CNH has been reported only recently.[13] The best values for heat of formation of H_2CNH obtained experimental (22±3 kcal/mol[14]) and computationally (21.1±0.5 kcal/mol[15]) are in good agreement. In the numerous computational studies,[16-25] the aminocarbene isomer, $HCNH_2$, is found to be 35-39 kcal/mol higher than H_2CNH, and singlet methylnitrene, CH_3N, is calculated to be ca 89 kcal/mol above H_2CNH. Aminocarbene can be produced by pyrolysis of aminocyclopropane.[26] Singlet methylnitrene can be generated by pyrolysis of methyl azide, CH_3N_3,[27] but calculations show that there is little or no barrier for singlet CH_3N to rearrange to H_2CNH.[16-19,21-25] Dissociation of H_2CNH has been studied experimentally and computationally.[17-20,24,27] It can occur by loss of hydrogen atom from either the carbon or the nitrogen with barriers of 85 – 95 kcal/mol to form HCNH and H_2CN, which can lose another hydrogen atom with barriers of 30 – 35 kcal/mol to produce HCN.[18,28-30] Alternatively, H_2CNH, $HCNH_2$ and CH_3N can dissociate by 1,1- or 1,2-H_2 eliminations with barriers of 85 – 100 kcal/mol above H_2CNH.[18-20,24]

Various isomers of H_2CNH monocation can be generated from the decomposition of methylamine, cyclopropylamine, azetidine, and aminocarbenium ion, and by the reaction of C^+ with NH_3.[20,26,31-33] Ab initio calculations show that the $HCNH_2^+$ isomer is ca 4 kcal/mol more stable than H_2CNH^+ and separated from the latter by a barrier of ca 57 kcal/mol.[17,34-36] The lowest energy dissociation channels involve loss of hydrogen atom.[34,35] Of the three possible singlet products resulting from H dissociation, $HCNH^+$ is the most

stable, CNH_2^+ is a minimum lying ca 52 kcal/mol higher, and H_2CN^+ is a saddle point ca 74 kcal/mol above $HCNH^+$.[37-41] Loss of H_2 from H_2CNH^+ / $HCNH_2^+$ leads to HNC^+ and HCN^+, with the former being 23 kcal/mol more stable than the latter.[42-46]

By comparison to neutral H_2CNH and the monocation, very few papers have examined the potential energy surface of the dication.[47,48] The most stable singlet dication isomer is $HCNH_2^{2+}$. CNH_3^{2+} is 48 kcal/mol higher and has a barrier of ca 30 kcal/mol for conversion to $HCNH_2^{2+}$. H_2CNH^{2+} is either a saddle point or a very shallow minimum ca 45 kcal/mol above $HCNH_2^{2+}$. H_3CN^{2+} dissociates to HCN^{2+} + H_2. Barriers of 40 – 65 kcal/mol separate $HCNH_2^{2+}$ and CNH_3^{2+} from dissociation products H^+ plus $HCNH^+$ and CNH_2^+. No studies appear to have been published on the potential energy surface of the trication.

The potential energy surfaces for the dissociation of H_2CNH and its positively charged ions that have been published over the past three decades involve a wide variety of computational methods. The differing accuracies of these methods make comparisons somewhat difficult. In the present paper, we use high level ab initio calculations to provide a consistent and accurate description of the structures and energetics of neutral H_2CNH and its cations on the ground state potential energy surfaces, and employ Born-Oppenheimer classical trajectory calculations at the B3LYP/6-311G(d,p) level to examine the dynamics of the dissociation of these species.

5.2 Computational Methods:

The GAUSSIAN suite of programs[49] was used for the ab initio electronic structure and molecular dynamics calculations. The geometries of the minima and the transition states were optimized by hybrid density functional theory (B3LYP[50-52]), second order Møller-Plesset perturbation theory (MP2[53]) and quadratic configuration interaction (QCISD[54]) methods. The SCF stability of each structure was tested using standard methods[55] (see Table 5.5 at the end of the text). The CBS-APNO complete basis set extrapolation method of Petersson and co-workers[56] was used to compute accurate energy differences. The CBS-APNO calculations have a mean absolute deviation of 0.5 kcal/mol for heats of reaction. Because singlet CH_3N requires a multi-reference treatment, its energy was estimated by adding the singlet-triplet energy difference calculated at the CASPT2/cc-pVTZ level of theory[25] to the triplet energy calculated by CBS-APNO.

Ab initio classical trajectories were computed at the B3LYP/6-311G(d,p) level of theory using a Hessian-based predictor-corrector method.[57,58] A predictor step is taken on the quadratic surface obtained from the energy, gradient and Hessian from the beginning point. A fifth order polynomial is then fitted to the energies, gradients and Hessians at the beginning and end points of the predictor step, and the Bulirsch-Stoer algorithm[59] is used to take a corrector step on this fitted surface with the angular forces projected out. The Hessians are updated for 5 steps before being recalculated analytically. The trajectories were terminated when the centers of mass of the fragments were 10 bohr apart and the gradient between the fragments was less than 1×10^{-5} hartree/bohr. A step

size of 0.25 $amu^{1/2}$ bohr was used for integrating the trajectories. Each SCF calculation was started with an unrestricted initial guess (using the GUESS=MIX keyword in GAUSSIAN) to permit homolytic bond dissociation. The energy was conserved to better than 1×10^{-5} hartree and the angular momentum was conserved to 1×10^{-8} ħ.

Trajectories were initiated at the local minima, H_2CNH, H_2CNH^+ and H_2NCH^{2+} (note that for the dication H_2CNH^{2+} is a first order saddle point while H_2NCH^{2+} is local minimum). A microcannonical ensemble of initial states was constructed using the quasi-classical normal mode sampling[60,61]. A total energy of 200, 150, and 120 kcal/mol above the zero point energy of H_2CNH, H_2CNH^+, and H_2NCH^{2+} was distributed among the 9 vibrational modes. The total angular momentum was set to zero corresponding to a rotationally cold distribution and the phases of the vibrational modes were chosen randomly. For each initial condition, the momentum and displacement were scaled so that the desired total energy was the sum of the vibrational kinetic energy and the potential energy obtained from the ab initio surface. A total of about 200 trajectories for each case were integrated for up to 400 *fs* starting from the local minima and ending when the products were well separated.

5.3 Results and Discussion

Structures and Energetics

The structures, selected geometrical parameters and CBS-APNO relative energies of reactants, intermediates, transition states and products for the dissociation of H_2CNH^{n+} are collected in Figures 5.1 – 5.8. The neutral, monocation,

dication and trication structures numbers have prefixes of N, C, D and T, respectively; the numbering of the structures is according to the potential energy profiles in Figures 5.2, 5.4, 5.6 and 5.8 (top to bottom in each column, left column to right column). Relative energies at the B3LYP/6-311G(d,p), MP2/6-311G(d,p) and CBS-APNO levels of theory are compared in Table 5.1. Generally, B3LYP gives better agreement with the CBS-APNO energies than MP2 (mean absolute deviation of 3.0 and 4.7 kcal/mol, respectively). Adiabatic ionization energies are compared in Table 5.2. The CBS-APNO values for H_2CNH and HCN are within 0.05 eV of the experimental values (9.97 and 13.60 eV, respectively).

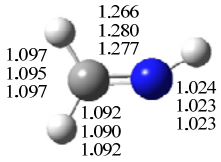

N-1 0.0

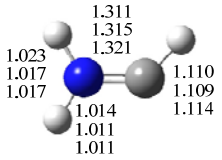

N-7, 35.6

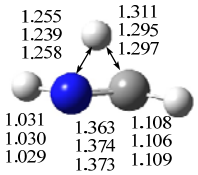

N-TS2, 88.9

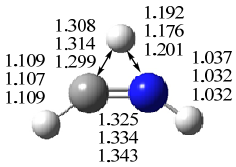

N-TS3, 81.8

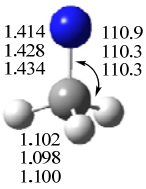

Triplet N-4, 54.0

(estimated singlet energy 86.0)

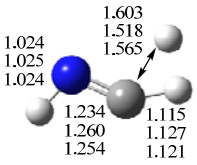

N-TS5, 85.8

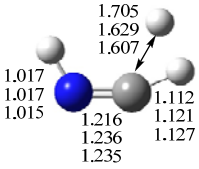

N-TS6, 84.6

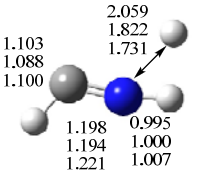

N-TS8, 106.7

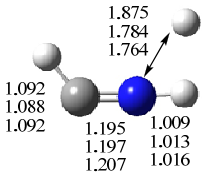

N-TS9, 100.5

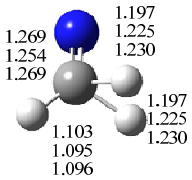

N-TS10, 95.7

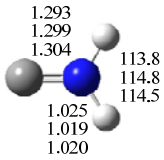

N-11, 117.6

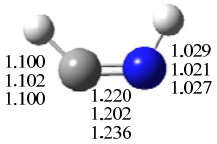

N-12, 99.1

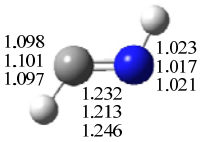

N-13, 94.4

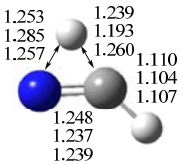

N-TS14, 131.1

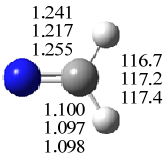

N-15, 86.7

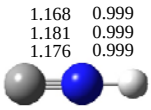

N-16, 22.5 (N-22, 126.3)

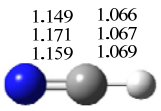

N-17, 8.2 (N-23, 111.9)

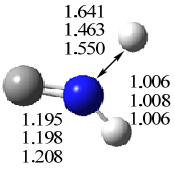

N-TS18, 140.3

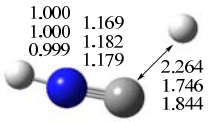

N-TS19, 128.7

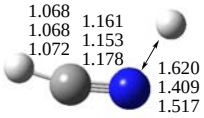

N-TS20, 121.2

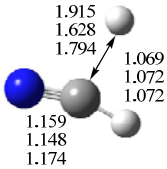

N-TS21, 117.5

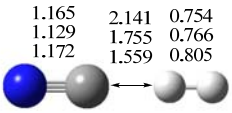

N-TS24, 136.6

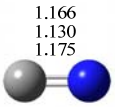

N-25, 133.2

Figure 5.1 Structures and selected geometric parameters of stationary points on the H_2CNH potential energy surface optimized at the B3LYP/6-311G(d,p), MP2/6-311G(d,p), and QCISD/6-311G(d,p) levels of theory (top, middle and bottom rows, respectively). The structure for CH_3N is constrained to be C_{3v} symmetry; all other structures are unconstrained. Bond distances are in Å, and angles are in degree. Relative energies are calculated at the CBS-APNO level of theory.

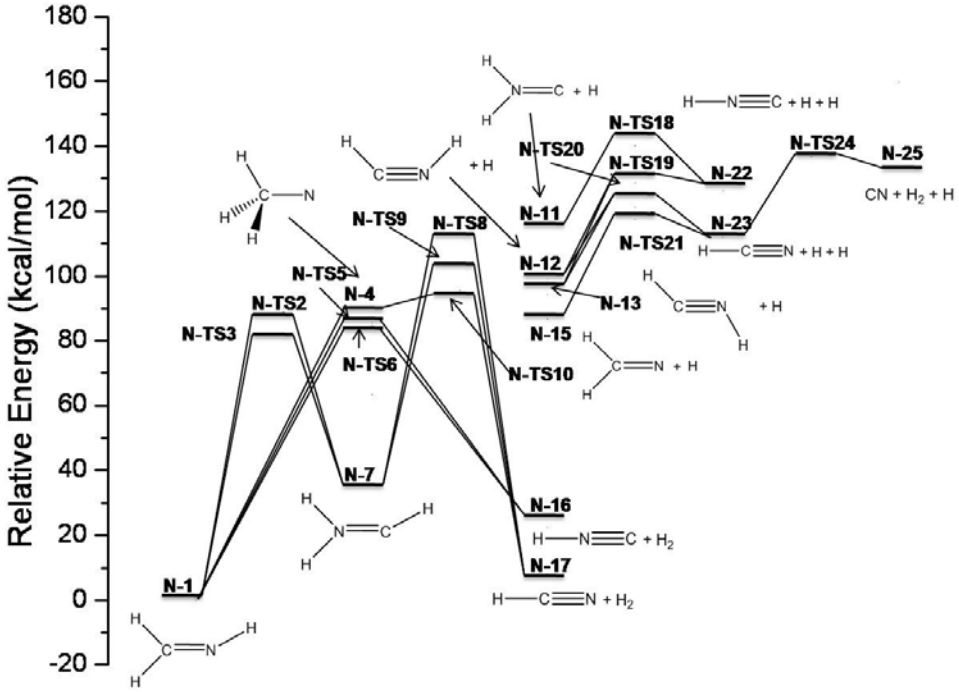

Figure 5.2 Potential energy profile for the isomerization and dissociation of neutral H_2CNH computed at the CBS-APNO level of theory.

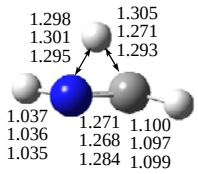

C-TS3, 54.7

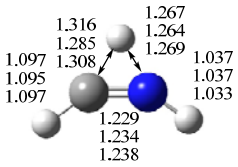

C-TS4, 42.2

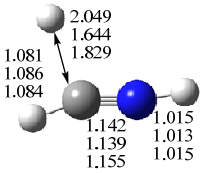

C-TS5, 31.2

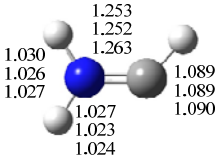

C-6, -3.8

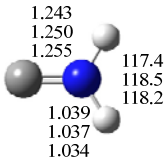

C-7, 78.7 (D-6, -7.9)

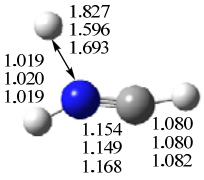

C-TS8, 39.0

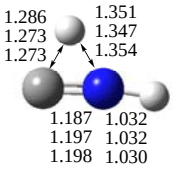

C-TS9, 97.8 (D-TS8, 11.2)

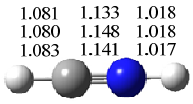

C-10,26.9 (D-10, -59.7)

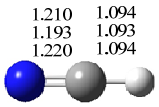

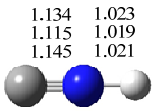

C-11, 93.6 (T-10, -285.2) C-12, 70.9 (T-7, -307.9)

Figure 5.3 Structures and selected geometric parameters of stationary points on the $H_2CNH^{+\cdot}$ potential energy surface optimized at the B3LYP/6-311G(d,p), MP2/6-311G(d,p), and QCISD/6-311G(d,p) levels of theory (top, middle and bottom rows, respectively). Bond distances are in Å, and angles are in degree. Relative energies are calculated at the CBS-APNO level of theory.

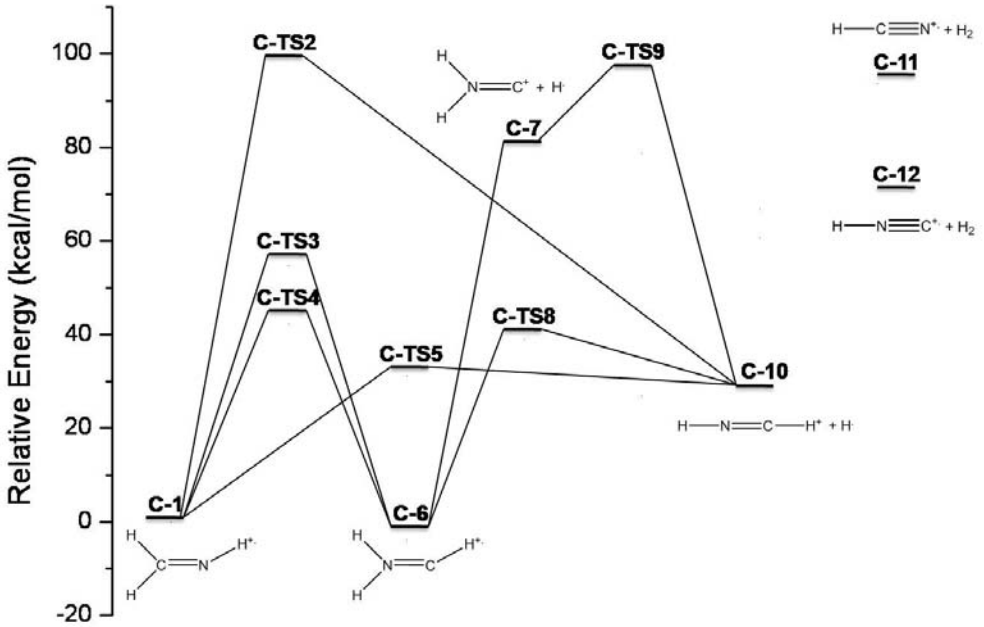

Figure 5.4 Potential energy profile for the isomerization and dissociation of $H_2CNH^{+\cdot}$ computed at the CBS-APNO level of theory.

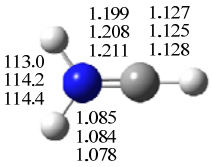

D-1, 0.0

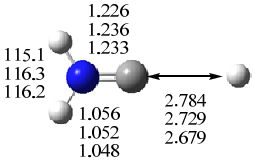

D-TS3, 64.5

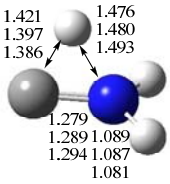

D-TS2, 73.1

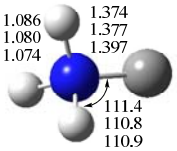

D-4, 50.6

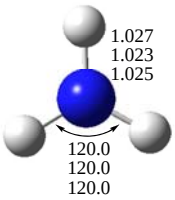

D-9, 2.0

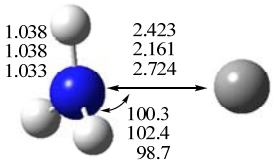

D-TS7, 99.2

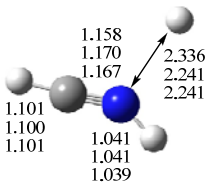

D-TS5, 41.5

Figure 5.5 Structures and selected geometric parameters of stationary points on the $HCNH_2^{2+}$ potential energy surface optimized at the B3LYP/6-311G(d,p), MP2/6-311G(d,p), and QCISD/6-311G(d,p) levels of theory (top, middle and bottom rows, respectively). Bond distances are in Å, and angles are in degree. Relative energies are calculated at the CBS-APNO level of theory.

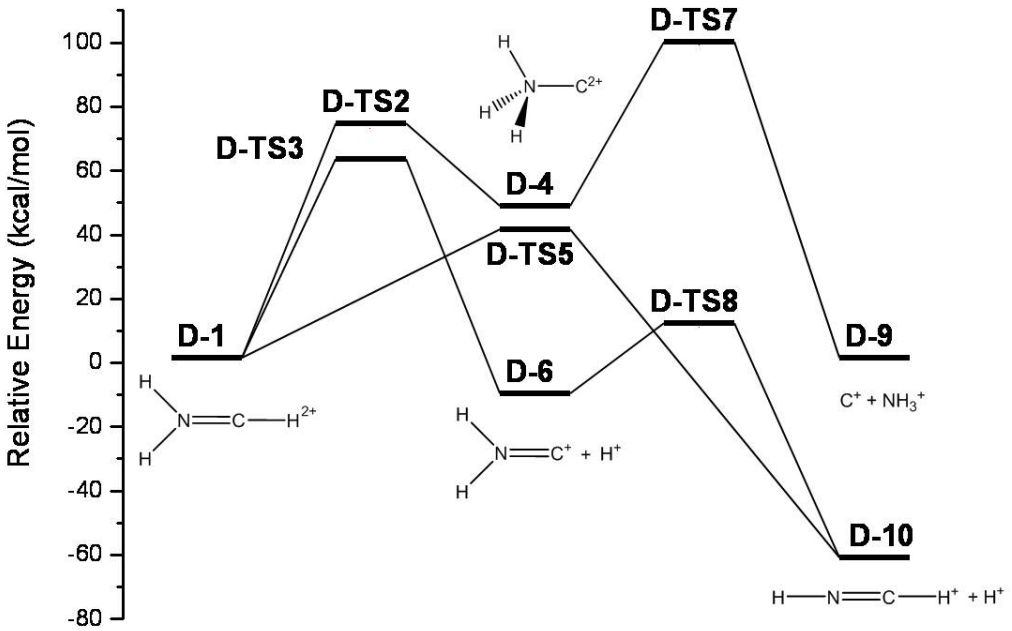

Figure 5.6 Potential energy profile for the isomerization and dissociation of $HCNH_2^{2+}$ computed at the CBS-APNO level of theory.

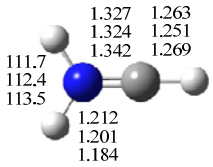

T-1, 0.0

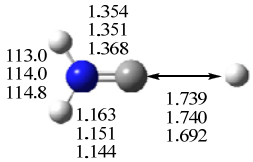

T-TS2, 3.5

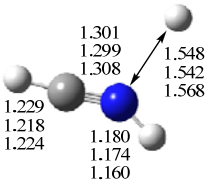

T-TS3, 1.9

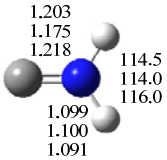

T-4, -231.2

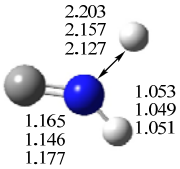

T-TS5, -199.3

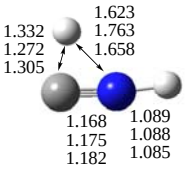

T-TS6, -205.3

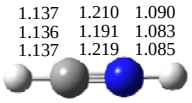

T-7, -244.4

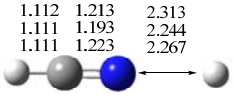

T-TS9, -203.5

Figure 5.7 Structures and selected geometric parameters of stationary points on the $HCNH_2^{3+}$ potential energy surface optimized at the B3LYP/6-311G(d,p), MP2/6-311G(d,p), and QCISD/6-311G(d,p) levels of theory (top, middle and bottom rows, respectively). Bond distances are in Å, and angles are in degree. Relative energies are calculated at the CBS-APNO level of theory.

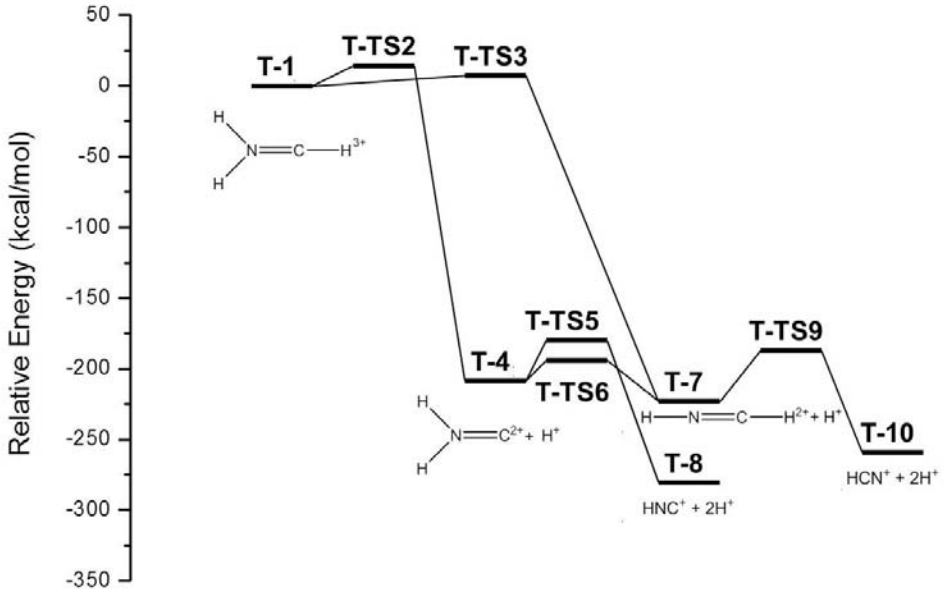

Figure 5.8 Potential energy profile for the isomerization and dissociation of $HCNH_2^{3+}$ computed at the CBS-APNO level of theory.

Table 5.1 Relative energies (in kcal/mol) of the various points on the H_2CNH, $H_2CNH^{+\cdot}$, $HCNH_2^{2+}$, and $HCNH_2^{3+}$ potential energy surfaces

	B3LYP/6-311G(d,p)	MP2/6-311G(d,p)	CBS-APNO
Neutral			
N-1	0.0	0.0	0.0
N-TS2	88.9	91.6	88.9
N-TS3	80.5	83.2	81.8
N-4[a]	80.7	86.1	86.0
N-TS5	84.0	90.0	85.8
N-TS6	83.6	90.8	84.6
N-7	34.6	38.4	35.6
N-TS8	103.0	118.2	106.7
N-TS9	97.8	107.6	100.5
N-TS10	92.9	108.9	95.7
N-11	113.1	113.6	117.6
N-12	95.6	98.7	99.1
N-13	91.5	93.7	94.4
N-TS14	129.5	129.7	131.1
N-15	82.8	90.1	86.7
N-16	22.7	19.5	22.5
N-17	8.4	0.8	8.2
N-TS18	135.6	138.7	140.3
N-TS19	126.7	120.9	128.7

N-TS20	117.3	120.9	121.2
N-TS21	115.8	119.4	117.5
N-22	126.4	113.8	126.3
N-23	112.0	95.1	111.9
N-TS24	135.4	145.3	136.6
N-25	134.8	141.5	133.2
MAD	2.1	5.1	
Monocation			
C-1	0.0	0.0	0.0
C-TS2	100.2	94.4	98.7
C-TS3	55.7	52.4	54.7
C-TS4	47.2	41.2	42.2
C-T5	34.2	29.1	31.2
C-6	-2.8	-9.2	-3.8
C-7	83.1	69.3	78.7
C-TS8	39.9	39.7	39.0
C-TS9	103.8	87.1	97.8
C-10	33.5	12.1	26.9
C-11	94.4	90.5	93.6
C-12	77.6	70.7	70.9
MAD	3.1	4.5	

Dication			
D-1	0.0	0.0	0.0
D-TS2	76.9	78.5	73.1
D-TS3	63.6	66.6	64.5
D-4	53.7	54.7	50.6
D-TS5	41.5	39.4	41.5
D-6	-5.7	-4.5	-7.9
D-TS7	111.0	118.6	99.2
D-TS8	15.0	13.2	11.2
D-9	6.0	1.2	2.0
D-10	-55.3	-61.7	-59.7
MAD	3.4	4.1	
Trication			
T-1	0.0	0.0	0.0
T-TS2	3.2	4.3	3.5
T-TS3	0.7	0.9	1.9
T-4	-225.2	-225.0	-231.2
T-TS5	-193.0	-194.8	-199.3
T-TS6	-198.1	-199.7	-205.3
T-7	-239.1	-238.8	-244.4
T-8	-297.3	-300.2	-307.9
T-TS9	-200.2	-198.9	-203.5

T-10	-280.4	-280.4	-285.2
MAD	4.5	4.1	
MAD Overall	3.0	4.7	

[a] Because singlet CH_3N requires a multi-reference treatment, its energy was estimated by adding the singlet-triplet energy difference calculated at the CASPT2/cc-pVTZ level of theory[25] to the energy calculated for the triplet.

Table 5.2 Adibatic ionization potentials (eV)

	B3LYP/6-311G(d,p)	MP2/6-311G(d,p)	CBS-APNO
H_2CNH	9.73	9.90	9.94
$HCNH_2$	8.11	7.84	8.23
$HCNH_2^+$	17.64	17.20	17.52
$HCNH_2^{++}$	30.56	30.57	30.78
HCNH	7.21	6.36	7.01
$HCNH^+$	22.59	22.90	22.76
CNH_2	8.43	7.98	8.25
CNH_2^+	21.04	21.01	21.09
HCN	13.46	13.79	13.64
HNC	12.11	12.12	12.04

Neutral H_2CNH

The key equilibrium structures and transition states on the potential energy surface for H_2CNH isomerization and dissociation are collected in Figure 5.1. The relative energies of these structures at the CBS-APNO level of theory are plotted in Figure 5.2. $HCNH_2$ (structure **N-7**) lies ca. 35 kcal/mol higher in energy than H_2CNH (**N-1**), in good accord with previous results.[16-25] Isomerization from H_2CNH to $HCNH_2$ occurs more readily via **N-TS3** with the H migrating in the plane of *cis*-HCNH than via **N-TS2** with the H migrating across the bond of *trans*-HCNH. Dissociation of $HCNH_2$ to HCN + H_2 (**N-17**) can occur by a transition state with H_2 *cis* or *trans* to the CH bond (**N-TS9** and **N-TS8**, resp.). The HCN + H_2 products can also be reached from H_2CNH via singlet CH_3N (**N-4**). There is little or no barrier for $^1A'$ CH_3N isomerizing back to CH_2NH.[16-19,21-25] The transition state for $CH_3N \rightarrow$ HCN + H_2 (**N-TS10**) is ca 10 kcal/mol lower than for $HCNH_2 \rightarrow$ HCN + H_2. The lowest energy molecular dissociation pathway for H_2CNH leads to the higher energy HNC + H_2 product (**N-16**), and can occur with the H_2 either *cis* or *trans* to the NH bond (**N-TS-6** and **N-TS5**, resp.)

Aside from the thermodynamically favorable H_2 molecule elimination channels, there are also several H atom dissociation channels to consider. Hydrogen atom dissociations from H_2CNH and $HCNH_2$ to form H_2CN (**N-15**), *cis*-HCNH (**N-12**), *trans*-HCNH (**N-13**) and H_2NC (**N-11**) radicals are expected to occur without a reverse barrier. If the hydrogen atom does not depart promptly, it can abstract another hydrogen to form H_2 plus HCN or HNC. This process has

been well documented in formaldehyde and acetaldehyde dissociation, and has been termed the “roaming atom” mechanism.[62-68] Isomerization and dissociations of H_2CN, HCNH and H_2NC have been studied previously.[18,28-30] Dissociations of H atom from these species to form HCN or HNC involves barriers of 22 - 34 kcal/mol at the CBS-APNO level of theory and occur via transition states **N-TS18** – **N-TS21**. A final hydrogen atom dissociation from HCN and HNC leads to CN radical. Alternatively, a free H atom could abstract a hydrogen to yield H_2 + CN. The latter has been studied comprehensively in previous theoretical work.[69,70]

Monocation

Figures 5.3 and 5.4 summarize the structures and energetics for $H_2CNH^{+\cdot}$ radical cation. $H_2CNH^{+\cdot}$ (**C-1**) lies 4 kcal/mol higher in energy than the $HCNH_2^{+\cdot}$ isomer (**C-6**), in good accord with the previous results.[35] Like the neutral case, the barrier for isomerization from $H_2CNH^{+\cdot}$ to $HCNH_2^{+\cdot}$ is lower for the proton migrating in the plane of *cis*-HCNH (**C-TS4**, 42 kcal/mol) than across the bond in *trans*-HCNH (**C-TS3**, 55 kcal/mol). Barriers for loss of hydrogen atom from $HCNH_2^{+\cdot}$ and $H_2CNH^{+\cdot}$ to form $HCNH^+$ + H (**C-10**) are 43 and 31 kcal/mol via **C-TS8** and **C-TS5**, respectively. $HCNH_2^{+\cdot}$ can also dissociate to produce CNH_2^+ + H, **C-7**, but this requires 82 kcal/mol. Isomerization of CNH_2^+ to $HCNH^+$ has a barrier of 19 kcal/mol (**C-TS9**). H_2CN^+ (**C-TS2**) is a saddle point and 72 kcal/mol above $HCNH^+$. Dissociation of molecular hydrogen from $HCNH_2^{+\cdot}$ and $H_2CNH^{+\cdot}$ could occur by 1,1-H_2 or 1,2-H_2 elimination to produce HNC^+ + H_2 (**C-12**) or HCN^+ + H_2 (**C-11**). Since these H_2 eliminations are rather endothermic (e.g. 75 and 97 kcal/mol from $HCNH_2^{+\cdot}$), H atom loss is the preferred channel for the

dissociation of $HCNH_2^{+\cdot}$ and $H_2CNH^{+\cdot}$. Hydrogen abstraction by a "roaming atom" mechanism[62-68] is also unlikely because these reactions are quite endothermic (44 and 67 kcal/mol for $HCNH^+ + H \rightarrow HNC^+ + H_2$ and $HCN^+ + H_2$, resp.). The HNC^+ is found to be 23 kcal/mol more stable than HCN^+, in agreement with earlier work.[42-46]

Dication

The structures and energetics for the singlet dication potential energy surface are collected in Figures 5.5 and 5.6. Similar to the monocation, $HCNH_2^{2+}$ (**D-1**) is the most stable structure. Even though the dication is isoelectronic with protonated acetylene, $C_2H_3^+$, there is no indication of a stable bridged structure.[71-79] In previous calculations, H_2CNH^{2+} was found to be a higher lying minimum at the HF and MP2 levels of theory.[47,48] We also find it to be a minimum at MP2, but with a barrier of less than 5 kcal/mol for conversion to H_2CNH^{2+}. More highly correlated methods (CCSD, CCSD(T) and BD with 6-311+G(d,p) and 6-311+G(3df,2pd) basis sets) show that H_2CNH^{2+} is a saddle point (See Figure 5.9 and Table 5.3). The small magnitude of the imaginary frequency (170*i* - 273*i*) indicates the potential energy surface is rather flat. A few density functionals (BMK, M052X, mPW1PW91, and PBE1PBE) find H_2CNH^{2+} to be a saddle point, while other functionals (BLYP, PBE, PW91, and TPSS) find it to be a shallow local minimum (Table 5.3). For B3LYP and TPSSh, H_2CNH^{2+} is a saddle point with the 6-311+G(3df,2pd) basis set, but a shallow minimum with the 6-311+G(d,p) basis set. In agreement with earlier calculations, CNH_3^{2+} (**D-4**) is a stable minimum, 51 kcal/mol above $HCNH_2^{2+}$ and separated from it by a barrier of 22 kcal/mol.

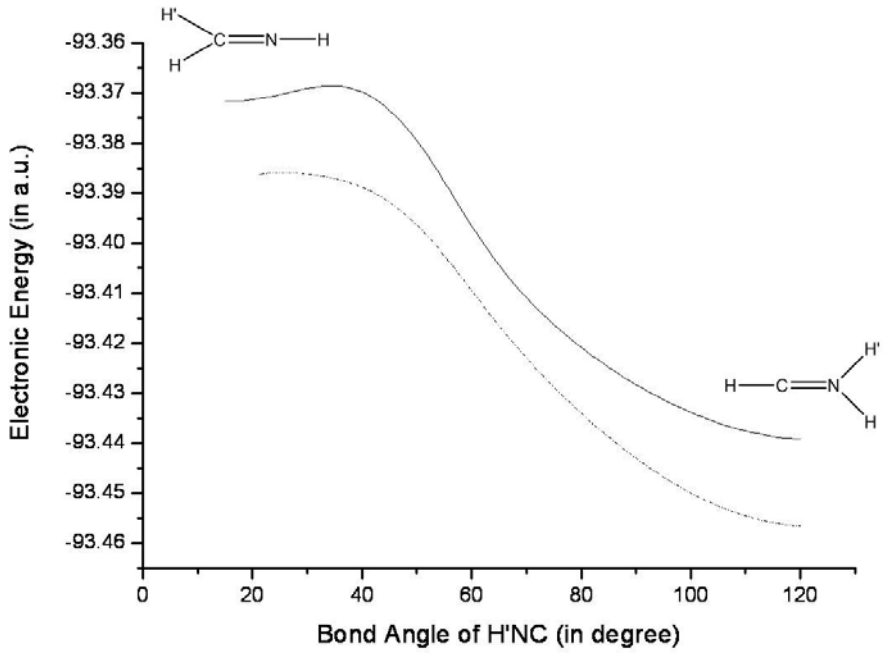

Figure 5.9 Relax scan of energies versus H'-N-C bond angle at the CCSD (dashed) and MP2 (solid) level of theory with 6-311+G(3df,2pd) basis set for $HCNH_2^{2+}$.

Table 5.3 Relative energies and lowest vibrational frequencies of H_2CNH^{2+} at various levels of theory[a]

	6-311+G(d,p)		6-311+G(3df,2pd)	
	E	Freq.	E	Freq.
B3LYP	37.5 (0)	43	37.3 (1)	115*i*
BLYP	33.2 (0)	210	33.0 (0)	185
PBEPBE	32.8 (0)	196	32.6 (0)	160
PW91PW91	32.9 (0)	201	32.7 (0)	165
TPSSTPSS	34.8 (0)	166	34.6 (0)	118
TPSSh	36.8 (0)	79	36.5 (1)	99*i*
BMK	38.8 (1)	210*i*	38.8 (1)	250*i*
M052X	44.0 (1)	284*i*	43.7 (1)	309*i*
mPW1PW91	38.6 (1)	125*i*	38.4 (1)	188*i*
PBE1PBE	38.3 (1)	130*i*	38.2 (1)	191*i*
MP2	40.4 (0)	401	39.9 (0)	381
BD	40.8 (1)	159*i*	40.8 (1)	169*i*
CCSD	40.5 (1)	197*i*	40.6 (1)	273*i*
CCSD(T)	37.8 (1)	60*i*	37.8 (1)	177*i*
CASSCF(4,4)			36.0 (1)	111*i*

[a] $E(H_2CNH^{2+})$-$E(HCNH_2^{2+})$ in kcal/mol; number of imaginary frequencies in parenthesis.

The lowest energy channel for dissociation of $HCNH_2^{2+}$ is loss of a proton to give $HCNH^+$ (**D-10**, -60 kcal/mol) with a barrier of 41 kcal/mol (**D-TS5**). Loss of a proton from $HCNH_2^{2+}$ to form CNH_2^+ (**D-6**) is less exothermic (-8 kcal/mol) and has a higher barrier (**D-TS3**, 65 kcal/mol). For the deprotonation of dications, $AH^{2+} \rightarrow A^+ + H^+$, careful attention must be paid to RHF/UHF instabilities[80]. If the second ionization potential of A ($A^+ \rightarrow A^{2+} + e^-$) is comparable to the ionization potential of hydrogen (13.6 eV), then spin unrestricted methods must be used. Since the ionization potentials of $HCNH^+$ and CNH_2^+ are 21 – 23 eV (see Table 5.2), spin restricted calculations are satisfactory for the deprotonation of $HCNH_2^{2+}$, as confirmed by SCF stability calculations on transition states **D-TS3** and **D-TS5** (see Table 5.5).

Trication

Figures 5.7 and 5.8 summarize the structures and energetics for the trication. Surprisingly, $HCNH_2^{3+}$ (**T-1**) is a local minimum. Dissociation to $HCNH^{2+} + H^+$ (**T-7**) is very exothermic (-244 kcal/mol) and has a barrier of only 2 kcal/mol (**T-TS3**). Dissociation to $CNH_2^{2+} + H^+$ (**T-4**) is a little less exothermic (-231 kcal/mol) and has a slightly higher barrier (**T-TS2**, 4 kcal/mol). $HCNH^{2+}$ and CNH_2^{2+} can lose another proton to form HNC^+ and HCN^+.

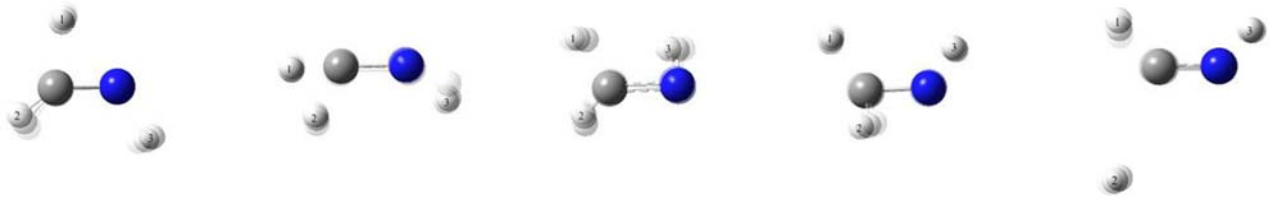

(a)

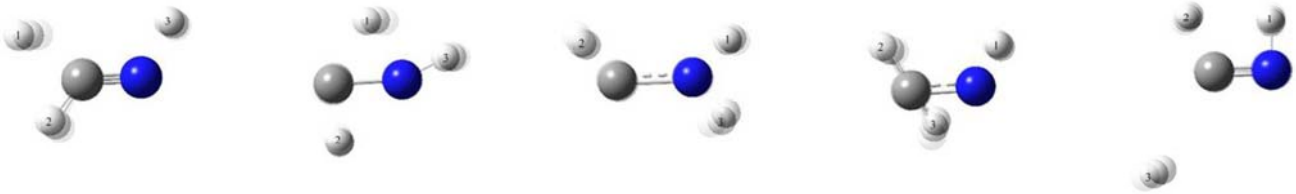

(b)

Figure 5.10 Snapshots along typical trajectories for $H_2CNH \rightarrow HCNH + H$ (a) direct dissociation, (b) indirect dissociation.

Dynamics

Comparison of the data in Table 5.1 indicates that the B3LYP/6-311G(d,p) level of theory that should be suitable for simulating the molecular dynamics of neutral and charged H_2CNH. The trajectories were started at local minima, namely H_2CNH for the neutral, $H_2CNH^{+\cdot}$ for the monocation, and $HCNH_2^{2+}$ for the singlet dication. Because of the low barriers for the trication, no trajectories were calculated for $HCNH_2^{3+}$. Approximately 200 trajectories were initiated for each case. The initial energies were chosen so that most trajectories would finish within 400 *fs* (200, 150 and 120 kcal/mol for the neutral, monocation and dication, resp.). For these conditions, only dissociations involving H^+, H atom and molecular H_2 were seen. Trajectories are termed direct if H^+ or H atom dissociate promptly. For indirect trajectories, hydrogen migrates within the molecule for some time before dissociation occurs. Figure 5.10 shows two examples of indirect trajectories (the corresponding movies are available on the ACS website). Because of the relatively high initial energy, H_2 dissociation by the "roaming" mechanism was not observed. The results of the trajectory calculations are summarized in Table 5.4.

Table 5.4 Branching ratios for H_2CNH, $H_2CNH^{+\cdot}$, and $HCNH_2^{2+}$ dissociation obtained from molecular dynamics at the B3LYP/6-311G(d,p) level of theory[a]

Product Structure	Description	Branching ratio
Neutral		
HCNH + H	Direct dissociation	28.26
HCN + H + H	Triple dissociation	21.74
H_2CN + H	Direct dissociation	12.50
CNH + H_2	Molecular elimination	10.33
HCN + H_2	Molecular elimination	9.24
CNH + H + H	Triple dissociation	8.70
HCNH + H	Indirect dissociation	3.80
H_2CN + H	Indirect dissociation	2.72
HCNH + H	H_2CN converts to HCNH	1.63
H_2CN + H	HCNH converts to H_2CN	0.54
CN + H_2 + H	Triple dissociation	0.54
Monocation		
$HCNH^+$ + H	Direct dissociation	67.80
$HCNH^+$ + H	Indirect dissociation	12.68
$HCNH^+$ + H	H_2CN^+ converts to $HCNH^+$	9.76
H_2CN^+ + H	Direct dissociation	3.41
CNH^+ + H_2	Molecular elimination	2.93
HCN^+ + H_2	Molecular elimination	2.44
CNH_2^+ + H	Direct dissociation	0.98
Dication		

$HCNH^+ + H^+$	Direct dissociation	51.01
$HCNH^+ + H^+$	Indirect dissociation	23.89
$HCNH_2^{2+}$	No dissociation	12.55
$CNH_2^+ + H^+$	Direct dissociation	10.12
$HCNH^+ + H^+$	CNH_2^+ converts to $HCNH^+$	2.02
$CNH_2^+ + H^+$	Indirect dissociation	0.41

[a] Microcanonical ensemble with quasiclassical normal mode sampling with 200, 150 and 120 kcal/mol excess energy above the H_2CNH, $H_2CNH^{+\cdot}$, and $HCNH_2^{2+}$ minima, respectively.

For the neutral H_2CNH, 17 trajectories resulted in HCN + H_2 (8 by 1,2 elimination, 5 by 1,1 elimination followed by isomerization, 3 by isomerization to H_3CN followed by 1,1 elimination and 1 by isomerization to $HCNH_2$ followed by 1,1 elimination), while 19 produced HNC + H_2 (primarily by 1,1 elimination). Even though HCN is more stable, the lower barrier for the direct dissociation of H_2CNH to HNC + H_2 leads to more trajectories yielding HNC as a product. Atomic H dissociation is more favorable than molecular H_2 elimination: 52 trajectories went to HCNH + H directly and 7 indirectly, while 23 went to H_2CN + H directly and 5 indirectly (because of the large amplitude vibrations, it is not possible to distinguish *cis*-HCNH and *trans*-HCNH products the trajectory calculations). During the course of the simulations, an additional 3 trajectories lost H atom directly to form H_2CN and then converted to HCNH, while 1 trajectory lost H atom directly to form HCNH and then converted to H_2CN. Because CNH_2 is much higher in energy, none of the trajectories produced this product. After the dissociation of the first H atom, a second H atom can be lost. Forty trajectories resulted in HCN + H + H, while 16 yielded CNH + H + H. The pathway leading to CN + H_2 + H has the highest barrier of the reactions observed, and only 1 trajectory out of 231 was seen for this channel.

In trajectories of the monocation, $HCNH^+$ accounts for 90% of the dissociation products. Of the 205 trajectories started from the $H_2CNH^{+\cdot}$ minimum, 139 trajectories produce $HCNH^+$ directly, and 26 indirectly. Another 20 trajectories lost H atom first to produce H_2CN^+ which then isomerized to the more stable species, $HCNH^+$. Seven more trajectories stopped at H_2CN^+ + H product

within the 400 *fs* simulation time. Since H_2CN^+ is a transition state, further propagation of these trajectories would yield $HCNH^+$. Two additional trajectories produced CNH_2^+ + H, which is separated from $HCNH^+$ + H by a barrier of ca 20 kcal/mol. Two H_2 molecule elimination channels were also observed: 5 trajectories resulted in HCN^+ + H_2 and 6 trajectories produced CNH^+ + H_2, each occurring by both 1,1 and 1,2-H_2 elimination.

For the dication, total 247 trajectories were integrated starting from $HCNH_2^{2+}$ with an initial energy of 120 kcal/mol. The major product is $HCNH^+$ + H^+, with 126 trajectories resulting in direct dissociation and 59 trajectories indirect. Only few trajectories produced CNH_2^+ + H^+: 25 direct and 1 indirect. Additionally, 5 trajectories first formed CNH_2^+ + H^+ and then converted to the more stable species, $HCNH^+$. There were also 31 trajectories that did not dissociated completely in the 400 *fs* simulation time.

5.4 Conclusions:

The energetics of neutral and positively charged H_2CNH dissociations has been studied by electronic calculations at a variety of levels of theory up to CBS-APNO. The results are in very good agreement with the best previous calculations. For H_2CNH^{2+}, higher correlated methods, such as CCSD and BD, reveal that it is a saddle point rather than a shallow local minimum. The dissociations of neutral and charged H_2CNH dissociation have been simulated by *ab initio* classical trajectories at the B3LYP/6-311G(d,p) level of theory. For the initial energies selected, many of the trajectories dissociate directly to produce H^+, H atom or H_2. However, in a sizeable fraction of the trajectories, there was

substantial migration of the hydrogen within the molecule before dissociation occurred. Hydrogen atom was the preferred dissociation product for the neutral and the monocation. Elimination of H_2 was seen in 20% of the trajectories for the neutral and in 5% of the trajectories for the monocation. The dication and trication produced only H^+. For the monocation and dication, $HCNH^+$ was formed in 85 – 90% of the dissociating trajectories.

Table 5.5 Relative energies (in kcal/mol), SCF stabilities and $<S^2>$ of various points on the H_2CNH, $H_2CNH^{+\cdot}$, $HCNH_2^{2+}$, and $HCNH_2^{3+}$ potential energy surfaces

	B3LYP/6-311G(d,p)	MP2/6-311G(d,p)	CBS-APNO
Neutral	singlet		
N-1, H_2CNH	0.0 (stable)	0.0 (RHF→UHF) 0.0025 (S^2=0)	0.0
N-TS2	88.9 (stable)	91.6 (RHF→UHF) 94.9 (S^2=0.21)	88.9 (restricted) 89.1 (unrestricted, S^2~0.22)
N-TS3	80.5 (stable)	83.2 (stable)	81.8
N-4[a]	80.7	86.1	86.0
N-TS5	84.0 (stable)	90.0 (RHF→UHF) 90.0 (S^2=0)	85.8
N-TS6	83.6 (stable)	90.8 (RHF→UHF) 90.8 (S^2=0)	84.6
N-7, H_2NCH	34.6 (stable)	38.4 (stable)	35.6
N-TS8	107.5 (RHF→UHF) 103.0 (S^2=0.63)	118.2 (RHF→UHF) 104.8 (S^2=1.01)	112.9 (restricted) 106.7 (unrestricted, S^2=0.0)
N-TS9	99.1 (RHF→UHF) 97.8 (S^2=0.27)	107.6 (RHF→UHF) 104.8 (S^2=1.01)	100.5 (restricted) 103.8 (unrestricted,

			S^2~0.88)
N-TS10	92.9 (RHF→UHF) 92.9 (S^2=0.0)	104.6 (RHF→UHF) 108.9 (S^2=0.70)	95.9 (restricted) 95.7 (unrestricted, S^2~0.75)
N-11, H_2NC + H	113.1 (stable, S^2=0.75)	113.6 (stable, S^2=0.77	117.6
N-12, *cis*HCNH + H	95.6 (stable, S^2=0.75)	98.7 (stable, S^2=0.81)	99.1
N-13, *trans*HCNH + H	91.5 (stable, S^2=0.75)	93.7 (stable, S^2=0.80)	94.4
N-TS14	129.5 (stable, S^2=0.76)	129.7 (stable, S^2=0.81)	131.1
N-15, H_2CN + H	82.8 (stable, S^2=0.76)	90.1 (stable, S^2=0.90)	86.7
N-16, HNC + H_2	22.7 (stable)	19.5 (stable)	22.5
N-17, HCN + H_2	8.4 (stable)	0.8 (stable)	8.2
N-TS18	135.6 (stable, S^2=0.76)	138.7 (stable, S^2=0.87)	140.3
N-TS19	126.7 (stable, S^2=0.75)	120.9 (stable, S^2=0.80)	128.7
N-TS20	117.3 (stable, S^2=0.76)	120.9 (stable, S^2=0.88)	121.2
N-TS21	115.8 (stable, S^2=0.76)	119.4 (stable, S^2=0.94)	117.5
N-22, HNC + H + H	126.4 (stable)	113.8 (stable)	126.3
N-23, HCN + H + H	112.0 (stable)	95.1 (stable)	111.9
N-TS24	135.4 (stable, S^2=0.76)	145.3 (stable, S^2=1.02)	136.6

N-25, CN + H_2 + H	156.0 (instable) 134.8 (S^2=0.76)	156.1 (instable) 141.5 (S^2=1.02)	159.8 (instable) 133.2 (S^2~1.1)
Monocation	doublet		
C-1, $H_2CNH^{+\cdot}$	0.0 (stable, S^2=0.76)	0.0 (stable, S^2=0.84)	0.0
C-TS3	55.7 (stable, S^2=0.76)	52.4 (stable, S^2=0.81)	54.7
C-TS4	47.2 (stable, S^2=0.76)	41.2 (stable, S^2=0.79)	42.2
C-TS5	34.2 (stable, S^2=0.75)	29.1 (stable, S^2=0.89)	31.2
C-6, $H_2NCH^{+\cdot}$	-2.8 (stable, S^2=0.76)	-9.2 (stable, S^2=0.81)	-3.8
C-7, H_2NC^+ + $H^\cdot$	83.1 (stable)	69.3 (RHF→UHF) 71.9 (S^2=0.17)	78.7
C-TS8	39.9 (stable, S^2=0.77)	39.7 (stable, S^2=0.95)	39.0
C-TS9	103.8 (stable)	87.1 (stable)	97.8
C-10, $HNCH^+$ + $H^\cdot$	33.5 (stable)	12.1 (stable)	26.9
C-11, HCN^+ + H_2	94.4 (stable, S^2=0.75)	90.5 (stable, S^2=0.77)	93.6
C-12, HNC^+ + H_2	77.6 (stable, S^2=0.77)	70.7 (stable, S^2=0.98)	70.9
Dication	Singlet		
D-1, H_2NCH^{2+}	0.0 (stable)	0.0 (stable)	0.0
D-TS2	76.9 (stable)	78.5 (stable)	73.1
D-TS3	63.6 (RHF→UHF) 63.6 (S^2=0.00)	66.6 (stable)	64.5

D-4, H_3NC^{2+}	53.7 (stable)	54.7 (stable)	50.6
D-TS5	41.5 (stable)	39.4 (stable)	41.5
D-6, $H_2NC^+ + H^+$	-5.7 (stable)	-4.5 (RHF→UHF) -1.9 (S^2=0.17)	-7.9
D-TS7	140.3 (RHF→UHF) 111.0 (S^2=0.62)	128.2 (RHF→UHF) 118.6 (S^2=0.79)	99.2
D-TS8	15.0 (stable)	13.3 (stable)	11.2
D-9, $NH_3^+ + C^+$	6.0 (stable, S^2=0.75)	1.2 (stable, S^2=0.76)	2.0
D-10, $HNCH^+ + H^+$	-55.3 (stable)	-61.7 (stable)	-59.7
Trication	double		
T-1, H_2NCH^{3+}	0.0 (stable, S^2=0.75)	0.0 (stable, S^2=0.76)	0.0
T-TS2	3.2 (stable, S^2=0.75)	4.3 (stable, S^2=0.76)	3.5
T-TS3	0.7 (stable, S^2=0.75)	0.9 (stable, S^2=0.76)	1.9
T-4, $H_2NC^{2+} + H^+$	-225.2 (stable, S^2=0.77)	-225.0(stable, S^2=0.93)	-231.2
T-TS5	-193.0 (stable, S^2=0.77)	-194.8 (stable, S^2=0.95)	-199.3
T-TS6	-198.1 (stable, S^2=0.76)	-199.7 (stable, S^2=0.82)	-205.3
T-7, $HNCH^{2+} + H^+$	-239.1 (stable, S^2=0.75)	-238.8 (stable, S^2=0.80)	-244.4
T-8, $HNC^+ + 2H^+$	-297.3 (stable, S^2=0.77)	-300.2 (stable, S^2=0.98)	-307.9
T-TS9	-200.2 (stable, S^2=0.75)	-198.9 (stable, S^2=0.79)	-203.5
T-10, $HCN^+ + 2H^+$	-280.4 (stable, S^2=0.75)	-280.4 (stable, S^2=0.77)	-285.2

[a] Because singlet CH_3N requires a multi-reference treatment, its energy was estimated by adding the singlet-triplet energy difference calculated at the CASPT2/cc-pVTZ level of theory[25] to the energy calculated for the triplet.

5.5 References

(1) Pearson, R.; Lovas, F. J. Microwave Spectrum and Molecular Structure of Methyleneimine (CH_2NH). *J. Chem. Phys.* **1977**, *66*, 4149-4156.

(2) Peel, J. B.; Willett, G. D. Photoelectron Spectrum of Methyleneimine by Spectrum Stripping. *J. Chem. Soc. Farad. Trans. II* **1975**, *71*, 1799-1804.

(3) Hamada, Y.; Hashiguchi, K.; Tsuboi, M.; Koga, Y.; Kondo, S. Pyrolysis of Amines - Infrared-Spectrum of Methyleneimine. *J. Mol. Spectrosc.* **1984**, *105*, 70-80.

(4) Bock, H.; Dammel, R. Molecular-Properties and Models .15. The Pyrolysis of Azides in the Gas-Phase. *Angew. Chem. -Int. Edit. Engl.* **1987**, *26*, 504-526.

(5) Bock, H.; Dammel, R. Gas-Phase Pyrolyses of Alkyl Azides - Gas-Phase Reaction .68. Experimental-Evidence for Chemical Activation. *J. Am. Chem. Soc.* **1988**, *110*, 5261-5269.

(6) Dickens, J. E.; Irvine, W. M.; DeVries, C. H.; Ohishi, M. Hydrogenation of Interstellar Molecules: A Survey for Methylenimine (CH_2NH). *Astrophys. J.* **1997**, *479*, 307-312.

(7) Milligan, D. E. Infrared Spectroscopic Study of the Photolysis of Methyl Azide and Methyl-D3 Azide in Solid Argon and Carbon Dioxide. *J. Chem. Phys.* **1961**, *35*, 1491-1497.

(8) Jacox, M. E.; Milligan, D. E. Infrared Spectrum of Methylenimine. *J. Mol. Spectrosc.* **1975**, *56*, 333-336.

(9) Duxbury, G.; Kato, H. Laser Stark and Interferometric Studies of Thioformaldehyde and Methyleneimine. *Faraday Discuss.* **1981**, *71*, 97-110.

(10) Halonen, L.; Duxbury, G. The Fourier-Transform Infrared-Spectrum of Methyleneimine in the 10 μm Region. *J. Chem. Phys.* **1985**, *83*, 2078-2090.

(11) Halonen, L.; Duxbury, G. High-Resolution Infrared-Spectrum of Methyleneimine, CH_2NH, in the 3μm Region. *J. Chem. Phys.* **1985**, *83*, 2091-2096.

(12) Halonen, L.; Duxbury, G. Fourier-Transform Infrared-Spectrum of CH_2NH - the Nu-Band. *Chem. Phys. Lett.* **1985**, *118*, 246-251.

(13) Teslja, A.; Nizamov, B.; Dagdigian, P. J. The Electronic Spectrum of Methyleneimine. *J. Phys. Chem. A* **2004**, *108*, 4433-4439.

(14) Holmes, J. L.; Lossing, F. P.; Mayer, P. M. Concerning the Heats of Formation of CH_2NH and CH_2NH^+. *Chem. Phys. Lett.* **1992**, *198*, 211-213.

(15) De Oliveira, G.; Martin, J. M. L.; Silwal, I. K. C.; Liebman, J. F. Definitive Heat of Formation of Methylenimine, CH_2=NH, and of Methylenimmonium Ion, $CH_2NH_2^+$, by Means of W2 Theory. *J. Comput. Chem.* **2001**, *22*, 1297-1305.

(16) Pople, J. A.; Raghavachari, K.; Frisch, M. J.; Binkley, J. S.; Schleyer, P. v. R. Comprehensive Theoretical-Study of Isomers and Rearrangement Barriers of Even-Electron Polyatomic-Molecules H_mABH_n (A, B = C, N, O, and F). *J. Am. Chem. Soc.* **1983**, *105*, 6389-6398.

(17) Nguyen, M. T.; Rademakers, J.; Martin, J. M. L. Concerning the Heats of Formation of the $[C,H3,N]^{+\cdot}$ Radical Cations. *Chem. Phys. Lett.* **1994**, *221*, 149-155.

(18) Nguyen, M. T.; Sengupta, D.; Ha, T. K. Another Look at the Decomposition of Methyl Azide and Methanimine: How is HCN Formed? *J. Phys. Chem.* **1996**, *100*, 6499-6503.

(19) Sumathi, R. Dissociation and Isomerization Reactions of Formaldimine on the Ground and Excited State Surface. *J. Mol. Struct. (THEOCHEM)* **1996**, *364*, 97-106.

(20) Roithova, J.; Schroder, D.; Schwarz, H. Unimolecular Fragmentation of CH_3NH_2: Towards a Mechanistic Description of HCN Formation. *Eur. J. Org. Chem.* **2005**, 3304-3313.

(21) Demuynck, J.; Fox, D. J.; Yamaguchi, Y.; Schaefer, H. F. Triplet Methylnitrene - an Indefinitely Stable Species in the Absence of Collisions. *J. Am. Chem. Soc.* **1980**, *102*, 6204-6207.

(22) Gonzalez, C.; Schlegel, H. B. Atmospheric Chemistry of Titan - Ab Initio Study of the Reaction between Nitrogen-Atoms and Methyl Radicals. *J. Am. Chem. Soc.* **1992**, *114*, 9118-9122.

(23) Richards, C.; Meredith, C.; Kim, S. J.; Quelch, G. E.; Schaefer, H. F. Is There a Potential Minimum Corresponding to Singlet Methylnitrene - a Study of the CH_3N to CH_2NH Rearrangement on the Lowest Singlet-State Potential-Energy Hypersurface. *J. Chem. Phys.* **1994**, *100*, 481-489.

(24) Arenas, J. F.; Marcos, J. I.; Otero, J. C.; Sanchez-Galvez, A.; Soto, J. A Multiconfigurational Self-Consistent Field Study of the Thermal Decomposition of Methyl Azide. *J. Chem. Phys.* **1999**, *111*, 551-561.

(25) Kemnitz, C. R.; Ellison, G. B.; Karney, W. L.; Borden, W. T. CASSCF and CASPT2 Ab Initio Electronic Structure Calculations Find Singlet Methylnitrene is an Energy Minimum. *J. Am. Chem. Soc.* **2000**, *122*, 1098-1101.

(26) Polce, M. J.; Kim, Y. J.; Wesdemiotis, C. First Experimental Characterization of Aminocarbene. *Int. J. Mass Spectrom.* **1997**, *167*, 309-315.

(27) Larson, C.; Ji, Y. Y.; Samartzis, P.; Wodtke, A. M.; Lee, S. H.; Lin, J. J. M.; Chaudhuri, C.; Ching, T. T. Collision-Free Photochemistry of Methylazide: Observation of Unimolecular Decomposition of Singlet Methylnitrene. *J. Chem. Phys.* **2006**, *125*, 133302.

(28) Sumathi, R.; Nguyen, M. T. A Theoretical Study of the CH_2N System: Reactions in Both Lowest Lying Doublet and Quartet States. *J. Phys. Chem. A* **1998**, *102*, 8013-8020.

(29) Tachikawa, H.; Iyama, T.; Fukuzumi, T. Decomposition Dynamics of Interstellar HCNH: Ab-initio MO and RRKM Studies. *Astron. Astrophys.* **2003**, *397*, 1-6.

(30) Metropoulos, A.; Thompson, D. L. A Quantum Chemistry Study of the Dissociation and Isomerization Reactions of Methylene Amidogene. *J. Mol. Struct. (THEOCHEM)* **2007**, *822*, 125-132.

(31) Burgers, P. C.; Holmes, J. L.; Terlouw, J. K. Gaseous [H-2, C, N]$^+$ and [H-3, C, N]$^{+\cdot}$ Ions - Generation, Heat of Formation, and Dissociation Characteristics of [H_2CN]+, [HCNH]$^+$, [CNH_2]$^+$, [H_2CNH]$^{+\cdot}$, and [$HCNH_2$]$^{+\cdot}$. *J. Am. Chem. Soc.* **1984**, *106*, 2762-2764.

(32) Flammang, R.; Nguyen, M. T.; Bouchoux, G.; Gerbaux, P. Characterization of Ionized Carbenes in the Gas Phase. *Int. J. Mass Spectrom.* **2000**, *202*, A8-A26.

(33) Curtis, R. A.; Farrar, J. M. C-N Bond Formation in the Gas-Phase Reaction of C^+ with NH_3. *J. Chem. Phys.* **1986**, *84*, 127-134.

(34) Frisch, M. J.; Raghavachari, K.; Pople, J. A.; Bouma, W. J.; Radom, L. Unusual Low-Energy Isomers for Simple Radical Cations. *Chem. Phys.* **1983**, *75*, 323-329.

(35) Uggerud, E.; Schwarz, H. An Ab Initio Molecular-Orbital Study on Rearrangement Fragmentation Processes of Isomeric $CH_3N^{+\cdot}$ Ions. *J. Am. Chem. Soc.* **1985**, *107*, 5046-5048.

(36) Sana, M.; Leroy, G.; Hilali, M.; Nguyen, M. T.; Vanquickenborne, L. G. Heats of Formation of Isomeric [C, H4, O]$^{+\cdot}$, [C, H3, N]$^{+\cdot}$ and [C, H5, N]$^{+\cdot}$ Radical Cations. *Chem. Phys. Lett.* **1992**, *190*, 551-556.

(37) Pearson, P. K.; Schaefer III, H. F. Some Properties of H_2CN^+ - Potentially Important Interstellar Species. *Astrophys. J.* **1974**, *192*, 33-36.

(38) Conrad, M. P.; Schaefer III, H. F. Role of Different Isomers of the H_2CN^+ Ion in the Formation of Interstellar Hydrogen Cyanide and Hydrogen Isocyanide. *Nature* **1978**, *274*, 456-457.

(39) Allen, T. L.; Goddard, J. D.; Schaefer, H. F. A Possible Role for Triplet H_2CN^+ Isomers in the Formation of HCN and HNC in Inter-Stellar Clouds. *J. Chem. Phys.* **1980**, *73*, 3255-3263.

(40) Defrees, D. J.; McLean, A. D. Does Carbon-Protonated Hydrogen-Cyanide, H_2CN^+, Exist. *J. Am. Chem. Soc.* **1985**, *107*, 4350-4351.

(41) Defrees, D. J.; Binkley, J. S.; Frisch, M. J.; McLean, A. D. Is N-Protonated Hydrogen Isocyanide, H_2NC^+, an Observable Interstellar Species. *J. Chem. Phys.* **1986**, *85*, 5194-5199.

(42) Hansel, A.; Scheiring, C.; Glantschnig, M.; Lindinger, W.; Ferguson, E. E. Thermochemistry of HNC, HNC^+, and CF_3^+. *J. Chem. Phys.* **1998**, *109*, 1748-1750.

(43) Peterson, K. A.; Mayrhofer, R. C.; Woods, R. C. Configuration-Interaction Spectroscopic Properties of X-2-Sigma+ HNC^+ and X-2-Pi HCN^+. *J. Chem. Phys.* **1990**, *93*, 4946-4953.

(44) Koch, W.; Frenking, G.; Schwarz, H. On the Barrier and Nature of [1.2]-Hydrogen Migrations in HCN / HNC and Their Cation Radicals. *Naturwissenschaften* **1984**, *71*, 473-474.

(45) Murrell, J. N.; Derzi, A. A. Calculations on the Ground-States of HCN^+ and HNC^+. *J. Chem. Soc. Farad. Trans. II* **1980**, *76*, 319-323.

(46) von Niessen, W.; Cederbaum, L. S.; Domcke, W.; Diercksen, G. H. F. Ionization Potentials of HCN and HNC by a Greens Function Method. *Mol. Phys.* **1976**, *32*, 1057-1061.

(47) Koch, W.; Heinrich, N.; Schwarz, H. Ab Initio Molecular-Orbital Study of the CH_3N^{2+} Potential-Energy Surface. *J. Am. Chem. Soc.* **1986**, *108*, 5400-5403.

(48) Wong, M. W.; Yates, B. F.; Nobes, R. H.; Radom, L. Substituted Methylene Dications (HCN^{2+}) - Some Remarkably Short Bonds to Carbon. *J. Am. Chem. Soc.* **1987**, *109*, 3181-3187.

(49) Frisch, M. J.; Trucks, G. W.; Schlegel, H. B.; et al. Gaussian Development Version, Revision F.02; Gaussian, Inc.; Wallingford, CT, 2007.

(50) Becke, A. D. A New Mixing of Hartree-Fock and Local Density-Functional Theories. *J. Chem. Phys.* **1993**, *98*, 1372-1377.

(51) Becke, A. D. Density Functional Theory. III. The Role of Exact Exchange. *J. Chem. Phys.* **1993**, *98*, 5648-5652.

(52) Lee, C.; Yang, W.; Parr, R. D. Development of the Colle-Salvetti Correlation Energy Formula into a Functional of the Electron Density. *Phys. Rev. B* **1988**, *37*, 785-789.

(53) Moller, C.; Plesset, M. S. Note on an Approximation Treatment for Many-Electron Systems. *Phys. Rev.* **1934**, *46*, 618-622.

(54) Pople, J. A.; Head-Gordon, M.; Raghavachari, K. Quadratic Configuration Interaction. A General Technique for Determining Electron Correlation Energies. *J. Chem. Phys.* **1987**, *87*, 5968-5975.

(55) Seeger, R.; Pople, J. A. Self-Consistent Molecular Orbital Methods. XVIII. Constraints and Stability in Hartree-Fock Theory. *J. Chem. Phys.* **1977**, *66*, 3045-3050.

(56) Montgomery, J. A.; Ochterski, J. W.; Peterson, G. A. A Complete Basis Set Model Chemistry. IV. An Improved Atomic Pair Natural Orbital Method. *J. Chem. Phys.* **1994**, *101*, 5900-5909.

(57) Bakken, V.; Millam, J. M.; Schlegel, H. B. Ab Initio Classical Trajectories on the Born-Oppenheimer Surface: Updating Methods for Hessian-Based Integrators. *J. Chem. Phys.* **1999**, *111*, 8773-8777.

(58) Millam, J. M.; Bakken, V.; Chen, W.; Hase, W. L.; Schlegel, H. B. Ab Initio Classical Trajectories on the Born-Oppenheimer Surface: Hessian-Based Integrators Using Fifth-Order Polynomial and Rational Function Fits. *J. Chem. Phys.* **1999**, *111*, 3800-3805.

(59) Stoer, J.; Bulirsch, R. *Introduction to Numerical Analysis*; Springer-Verlag: New York, 1980.

(60) Hase, W. L. In *Encyclopedia of Computational Chemistry*; Schleyer, P. v. R., Allinger, N. L., Clark, T., Gasteiger, J., Kollman, P. A., Schaefer III, H. F., Schreiner, P. R., Eds.; Wiley: Chichester, 1998, p 402-407.

(61) Peslherbe, G. H.; Wang, H.; Hase, W. L. Monte Carlo Sampling for Classical Trajectory Simulations. *Advances in Chemical Physics* **1999**, *105*, 171-201.

(62) Suits, A. G. Roaming Atoms and Radicals: A New Mechanism in Molecular Dissociation. *Accounts Chem. Res.* **2008**, *41*, 873-881.

(63) Rubio-Lago, L.; Amaral, G. A.; Arregui, A.; Izquierdo, J. G.; Wang, F.; Zaouris, D.; Kitsopoulos, T. N.; Banares, L. Slice Imaging of the Photodissociation of Acetaldehyde at 248 nm. Evidence of a Roaming Mechanism. *Phys. Chem. Chem. Phys.* **2007**, *9*, 6123-6127.

(64) Lahankar, S. A.; Chambreau, S. D.; Zhang, X. B.; Bowman, J. M.; Suits, A. G. Energy Dependence of the Roaming Atom Pathway in Formaldehyde Decomposition. *J. Chem. Phys.* **2007**, *126*, 044314.

(65) Lahankar, S. A.; Chambreau, S. D.; Townsend, D.; Suits, F.; Farnum, J.; Zhang, X. B.; Bowman, J. M.; Suits, A. G. The Roaming Atom Pathway in Formaldehyde Decomposition. *J. Chem. Phys.* **2006**, *125*, 044303.

(66) Houston, P. L.; Kable, S. H. Photodissociation of Acetaldehyde as a Second Example of the Roaming Mechanism. *Proc. Natl. Acad. Sci.* **2006**, *103*, 16079-16082.

(67) Chambreau, S. D.; Townsend, D.; Lahankar, S. A.; Lee, S. K.; Suits, A. G.; Royal Swedish Acad. Sciences: 2006, p C89-C93.

(68) Townsend, D.; Lahankar, S. A.; Lee, S. K.; Chambreau, S. D.; Suits, A. G.; Zhang, X.; Rheinecker, J.; Harding, L. B.; Bowman, J. M. The Roaming Atom: Straying from the Reaction Path in Formaldehyde Decomposition. *Science* **2004**, *306*, 1158-1161.

(69) Bair, R. A.; Dunning, T. H. Theoretical-Studies of the Reactions of HCN with Atomic-Hydrogen. *J. Chem. Phys.* **1985**, *82*, 2280-2294.

(70) ter Horst, M. A.; Schatz, G. C.; Harding, L. B. Potential Energy Surface and Quasiclassical Trajectory Studies of the CN + H_2 Reaction. *J. Chem. Phys.* **1996**, *105*, 558-571.

(71) Sharma, A. R.; Wu, J. Y.; Braams, B. J.; Carter, S.; Schneider, R.; Shepler, B.; Bowman, J. M. Potential Energy Surface and Multimode Vibrational Analysis of $C_2H_3^+$. *J. Chem. Phys.* **2006**, *125*, 224306.

(72) Psciuk, B. T.; Benderskii, V. A.; Schlegel, H. B. Protonated Acetylene Revisited. *Theor. Chem. Acc.* **2007**, *118*, 75-80.

(73) Glukhovtsev, M. N.; Bach, R. D. Ab Initio Study on the Thermochemistry of Vinyl Radical and Cation. *Chem. Phys. Lett.* **1998**, *286*, 51-55.

(74) Lindh, R.; Rice, J. E.; Lee, T. J. The Energy Separation between the Classical and Nonclassical Isomers of Protonated Acetylene - an Extensive Study in One-Particle and N-Particle Space Saturation. *J. Chem. Phys.* **1991**, *94*, 8008-8014.

(75) Liang, C.; Hamilton, T. P.; Schaefer, H. F. Classical and Nonclassical Forms of the Vinyl Cation - a Coupled Cluster Study. *J. Chem. Phys.* **1990**, *92*, 3653-3658.

(76) Curtiss, L. A.; Pople, J. A. Theoretical-Study of Structures and Energies of Acetylene, Ethylene, and Vinyl Radical and Cation. *J. Chem. Phys.* **1988**, *88*, 7405-7409.

(77) Pople, J. A. The Structure of the Vinyl Cation. *Chem. Phys. Lett.* **1987**, *137*, 10-12.

(78) Lindh, R.; Roos, B. O.; Kraemer, W. P. A CASSCF CI Study of the Hydrogen Migration Potential in Protonated Acetylene, $C_2H_3^+$. *Chem. Phys. Lett.* **1987**, *139*, 407-416.

(79) Lee, T. J.; Schaefer, H. F. The Classical and Nonclassical Forms of Protonated Acetylene, $C_2H_3^+$ - Structures, Vibrational Frequencies, and Infrared Intensities from Explicitly Correlated Wave-Functions. *J. Chem. Phys.* **1986**, *85*, 3437-3443.

(80) Gill, P. M. W.; Radom, L. How Does a Dication Lose a Proton. *J. Am. Chem. Soc.* **1988**, *110*, 5311-5314.

CHAPTER 6

AB INITIO MOLECULAR DYNAMICS STUDY OF THE REACTION BETWEEN Th^+ AND H_2O

6.1 Introduction:

Within the last decades, reactions of actinide cations with small molecules in the gas phase have attracted significant attention.[1-21] In these reactions, the distinctive electronic structures and chemical properties of the f-block elements can be studied in the absence of perturbing factors such as solvation or lattice neighbors. The actinides are the 5f homologs of the lanthanides, with the 5f valence orbitals being filled between Ac and Lr, but they are notably different from the lanthanides, in which the 4f electrons do not participate in bond formation. Potential contribution of the 5f electrons to the reactivity is of great interest, particularly for early actinides, because the 5f electrons are relatively high in energy and are spatially extended. Consequently, numerous studies have then been carried out on the reactions of actinide cations with small molecules both experimentally[1-17] and theoretically.[18-21] The experimental studies have already been comprehensively reviewed.[1-3] One of the techniques used in the study of the reactivity of actinides is laser ablation with prompt reaction and detection (LAPRD).[3] Gibson and Haire reported the reactions of Pa^+ and PaO^+ with neutral molecules, showing that Pa^+ is very reactive with the reagents as diverse as alkenes, ethylene oxide, and sulfur hexafluoride.[4] Further

investigations by the same group also include, the reactions of Es^+ with dimethylether, 1,2-ethanedithiol, and 1,2,3,4,5-pentamethylcyclopentadiene.[5,6] LAPRD studies have established a following ordering of reactivities: $Th^+ \geq Pa^+ \geq U^+ \approx Np^+ > Cm^+ \geq Pu^+ > Bk^+ > Am^+ \approx Cf^+ \geq Es^+$. Fourier transform ion cyclotron resonance mass spectrometry (FTICR/MS) has been used extensively to study actinide ion reactivity and can be used to measure reaction kinetics, which cannot be accomplished by LAPRD. Reactions of An^+ and AnO^+ (An=Th, U, Np, Pu, Am) with a number of oxidants were studied with the aid of FTICR/MS and reaction efficiencies were obtained.[7-9] Additional investigations examined the reactivity of dications,[10] and studied the activation of hydrocarbons[11-14]. Quadruple ion trap mass spectrometry (QIT/MS) has also been used to examine the reactivity of actinide ions, and the differences between QIT/MS and FTICR/MS were explored by Jackson et al.[15-17] in a study of the reactivity of Th^+, U^+, ThO^+, UO^+, and UO_2^+ with HCp^*.

The experimental techniques discussed above unquestionably provide novel information on the gas-phase reactivity of actinide ions. However, limitations do still exist in terms of detailed information about the reaction mechanisms. Therefore theoretical studies can be particularly valuable in providing additional information. Uranium is one of the most well-studied actinides, and in particular, the reactions of $U^{+/2+}$ and $UO^{+/2+}$ with H_2O and N_2O were first investigated by density functional theory (DFT) to examine O-H and N-O bond activation by uranium ions.[18-20]

In addition to uranium and its oxides, thorium cations are able to activate

the O-H bonds in water. Reactions of Th^+ and Th^{2+} with water have been detected by the FTICR/MS experiments, and the products included ThO^+ and $ThOH^+$.[8-10] Further analyses indicate that ThO^+ is the major product (branching ratio 65%) over $ThOH^+$ (branching ratio 35%) for Th^+,[8,9] whereas $ThOH^+$ dominates with a branching ratio of 90% for Th^{2+}.[10] Furthermore, the potential energy surfaces of Th^+ and Th^{2+} with water have been mapped by several DFT methods.[21]

The present work focuses on the dynamics of the reaction of Th^+ with water. A range of theoretical methods are used to obtain better estimates of the structure and thermodynamics. The dynamics of the reaction are investigated by means of ab initio molecular classical trajectory calculations.

6.2 Computational Methods:

Three different levels of theory were used to optimize the geometries of the minima and the transition states on the potential energy surface of the dissociation of $ThOH_2^+$. First, the B3LYP[22-24], PW91PW91[25,26], TPSSTPSS[27], BHandHLYP, and BMK[28] functionals were used, along with the Stuttgart relativistic effective core potential (SDD)[29] for Th (30 valence electrons), and the 6-311++G(d,p) basis set for O and H atoms (designated as SDD). These calculations were carried out using the Gaussian suite of programs[30]. Secondly, calculations employing the relativistic two-component zero-order regular approximation (ZORA) with both scalar relativistic (SR) and spin-orbit (SO) effects were performed with the ADF code.[31-33] The PW91 exchange correlation energy functional and the TZP basis set for Th (frozen core, 12 valence

electrons) and the TZ2P basis set for H_2O (O 1s frozen) were used for geometry optimization and frequency calculations (designated as PW91/ZORA-SR and PW91/ZORA-SO). Finally, coupled cluster (CCSD(T))[34] calculations with the SDD basis for Th and 6-311++G(d,p) for O and H atoms were carried out using the MOLPRO package[35].

Similar to G2(MP2)[36] and G3(MP2)[37] treatment, we estimated CCSD(T) energies for all the species with a even larger basis set (designated SDD+, SDD plus two additional g functions for Th atom and 6-311++G(3df,2p) for O and H atoms) by using a composite approach:

$$E(est.CCSD(T)/SDD+) = E(CCSD(T)/SDD) + (E(MP2/SDD+) - E(MP2/SDD)) \quad (1)$$

Ab initio classical trajectories were computed at the PW91/SDD level of theory using a Hessian-based predictor-corrector method[38,39] with the Gaussian suite of program. A predictor step is taken on the quadratic surface obtained from the energy, gradient and Hessian from the beginning point. A fifth order polynomial is then fitted to the energies, gradients and Hessians at the beginning and end points of the predictor step, and the Bulirsch-Stoer algorithm[40] is used to take a corrector step on this fitted surface with the angular forces projected out. The Hessians are updated for 5 steps before being recalculated analytically. The trajectories were terminated when the centers of mass of the fragments were 10 bohr apart and the gradient between the fragments was less than 1×10^{-5} hartree/bohr. A step size of 0.25 $amu^{1/2}$ bohr was used for integrating the trajectories. The energy was conserved to better than 1×10^{-5} hartree and the angular momentum was conserved to 1×10^{-8} ħ.

Trajectories were initiated at the transition state for the Th^+ insertion into the O-H bond of water. A microcanonical ensemble of initial states was constructed using the quasi-classical normal mode sampling.[41,42] Since **TS1** is estimated to be at least 20 kcal/mol below the $Th^+ + H_2O$ reactants,[21] a total energy of 20 kcal/mol above the zero point energy of the transition state was distributed among the 5 vibrational modes and translation along the transition vector toward the product. The total angular momentum was set to zero (corresponding to a rotationally cold distribution) and the phases of the vibrational modes were chosen randomly. The momentum and displacement were scaled so that the desired total energy was the sum of the vibrational kinetic energy and the potential energy obtained from the ab initio surface. The initial conditions are similar to those used in previous trajectory calculations.[43,44] A total of 200 trajectories were integrated for up to 400 *fs* starting from the transition state. Of these, 36 were unsuccessful because of SCF convergence failure or lack of conservation of energy and had to be discarded. About half of the remaining trajectories did not react within 400 *fs*. A number of these initially unreactive trajectories were integrated for an additional 800 *fs* and showed roughly the same branching ratio.

6.3 Results and Discussion

Structures and Energetics

The optimized geometries of the $ThOH_2^+$ and various intermediates, transition states (TS), and products are shown in Figure 6.1 for a number of levels of theory. The relative energies of these stationary structures at the

PW91/SDD level of theory are summarized in Figure 6.2. The study by Russo and co-workers[21] has shown that for the reaction of Th^+ with water, the reaction path evolves along the doublet surface from the formation of the initial Th^+-OH_2 complex to the $HThO^+$ + H and ThO^+ + H_2 products. The present calculations confirm that doublet transition state, **TS1**, is lower than the quartet **TS1'**. Although, the doublet Th^+-OH_2 complex shows extensive spin contamination, the doublet transition state **TS1** has much less spin contamination and the quartet **TS1'** has even less (See Table 6.1). Spin projection would result in further lowering of the doublet **TS1** relative to the quartet. Beyond the transition state, the doublet surface is much lower in energy than the quartet spin surface (see Figure 6.2 and ref 21), and has very little spin contamination. Thus, we will focus our study on the doublet spin surface, and start at the doublet Th^+-OH_2 transition state. In addition to the B3LYP/SDD and PW91/ZORA-SR levels of theory used in the study by Russo and co-workers,[21] we also investigated the potential energy surface at several other levels of theory, including the PW91/SDD, TPSS/SDD, PW91/ZORA-SO, CCSD(T)/SDD and est.CCSD(T)/SDD+ in order to assess the quality of these results (Table 6.1). These calculations cover pure GGA functionals, meta-GGAs, GGA with spin-orbit effect, and couple-cluster calculations with effective core potentials (ECP). This range of methods should provide a broad survey of the structures and energetics associated with the dissociation reaction of $ThOH_2^+$.

The calculations by Russo and co-workers[21] have shown that $ThOH_2^+$, **1**, is in a deep potential minimum, ca 30 kcal/mol below reactants. At all levels of

theory, they find Th^+ and H_2O form a strong bond, with R(Th-O) around 2.4 Å. The reaction proceeds through **TS1**, which is 4.1 kcal/mol higher than $ThOH_2^+$ at the PW91/SDD level. In **TS1**, one of the two H atoms migrates from O to Th leading to $HThOH^+$, **2**. For the H_2 molecular elimination channel calculated at the PW91/SDD level, a barrier of 21.6 kcal/mol needs to be overcome first to reach H_2ThO^+, **3**, and then H_2 molecule dissociates. For the H atom elimination channel, the barrier to break the O-H bond is much higher, 47.1 kcal/mol at the PW91/SDD level. This transition state, **TS3,** cannot be located by CCSD(T)/SDD, suggesting that there is no reverse barrier for the O-H bond dissociation at this level of theory.

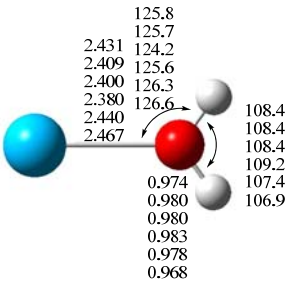

1

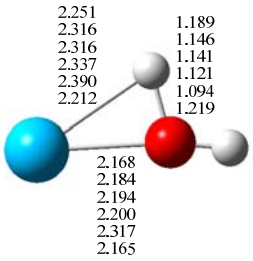

TS1

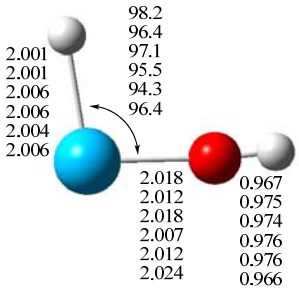

2

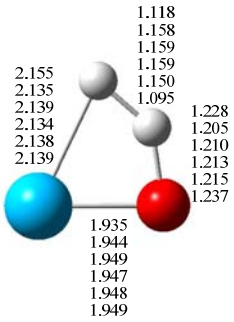

TS2

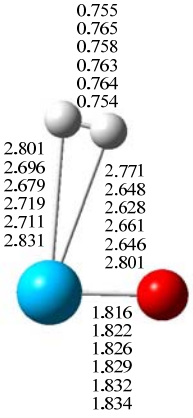

3

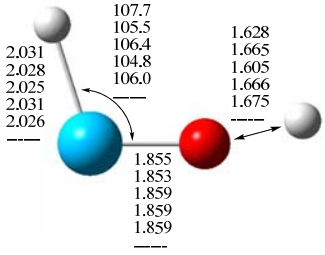

TS3

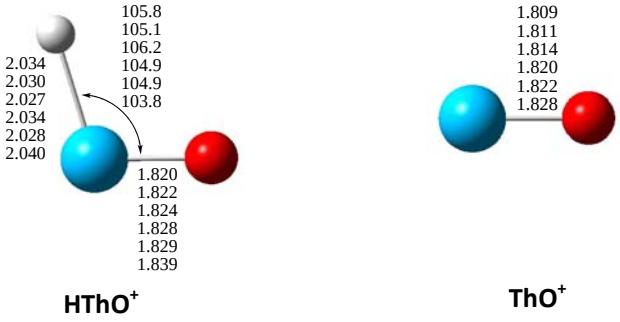

Figure 6.1 Structures and selected geometric parameters of stationary points on the $ThOH_2^+$ potential energy surface optimized at the B3LYP/SDD, PW91/SDD, TPSS/SDD, PW91/ZORA-SR, PW91/ZORA-SO, and CCSD(T)/SDD levels of theory (from top to bottom rows, respectively). Bond distances are in Å, and angles are in degrees.

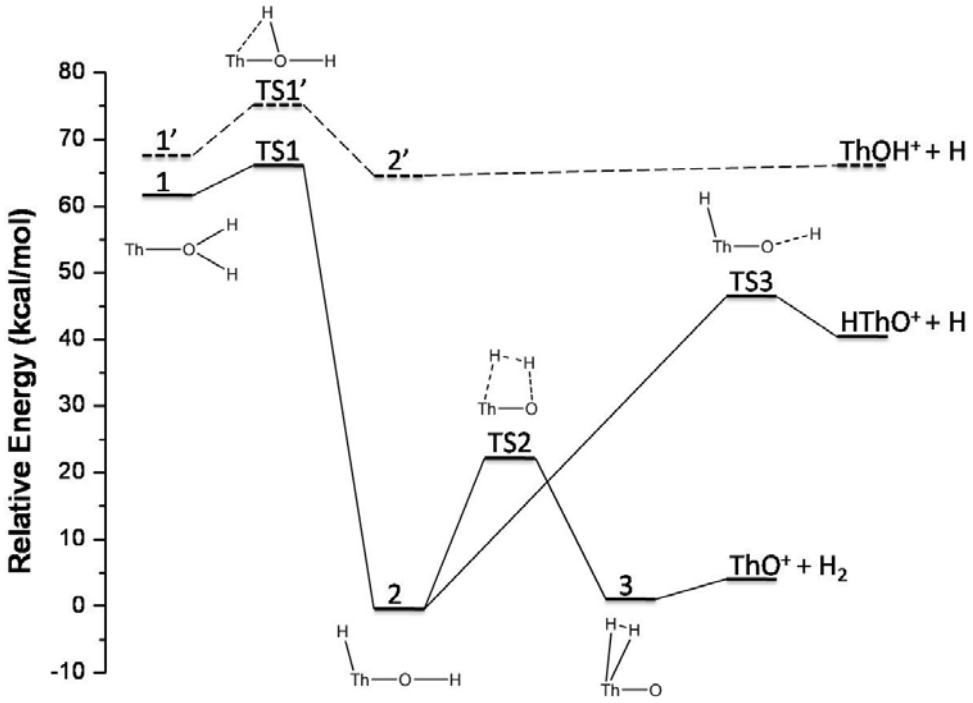

Figure 6.2 Potential energy profile for the isomerization and dissociation of the $ThOH_2^+$ computed at the PW91/SDD level of theory.

The relative energies of selected stationary points on the potential energy surface have been computed at a number of levels of theory and are compared in Table 6.1. It is well-known that some DFT methods perform well in predicting energies, but the results can be sensitive to the functional. Therefore, a variety of DFT functionals have been employed to investigate the potential energy surface. Except for **1** and **TS1**, spin contamination is minimal. For the CCSD(T) calculation, the T1 diagnostic values for all the species are within the trust range[45,46], less than 0.023, indicating single reference coupled cluster calculations should provide good results. The two methods that ought to be most reliable are PW91/ZORA-SO and est.CCSD(T)/SDD+. The latter uses a composite approach similar to G2(MP2) and G3(MP2) which are often employed in benchmark calculations. Spin-orbit effects are important in actinide compounds, and ZORA-SO calculations are an efficient way to take this into account. The est.CCSD(T)/SDD+ energies generally agree well with PW91/ZORA-SO with only one exception, **TS2**, which differs by approximately 10 kcal/mol. B3LYP/SDD agrees well with est.CCSD(T)/SDD+. BMK/SDD and BHandHLYP/SDD provide results that are similar to each other, but when compared to est.CCSD(T)/SDD+ both underestimate all the relative energies except for **TS2**. TPSS/SDD shows better agreement in the dissociation energies of two products, but gives a higher relative energy for $ThOH_2^+$, **1**. PW91/SDD is generally an improvement over TPSS/SDD. For PW91 with the frozen core TZ2P basis set, the ZORA-SR and ZORA-SO calculations agree well with each other

(MAD less than 1.0 kcal/mol). Without ZORA-SR or ZORA-SO, some of the relative energies decrease by 5 – 20 kcal/mol. The PW91/SDD calculations are in good agreement with PW91/ZORA-SO (MAD 1.2 kcal/mol) and CCSD(T)/SDD+ (MAD 3.1 kcal/mol). Therefore, PW91/SDD has been chosen for the trajectory calculations as a satisfactory yet practical compromise between the most trusted results.

Table 6.1 Relative energies (in kcal/mol) of the various points on the doublet ThH_2O^+ potential energy surface

	1	**TS1**	**2**	**TS2**	**3**	**TS3**	**$ThO^+ + H_2$**	**$HThO^+ + H$**
B3LYP[a]	61.8	69.4	0.0	29.1	3.2	54.9	3.9	46.1
PW91[a]	62.3	66.4	0.0	21.6	0.3	47.1	3.2	40.1
TPSS[a]	73.1	72.5	0.0	23.3	-0.8	46.2	2.6	40.4
BMK[a]	50.1	61.1	0.0	29.7	-4.5	51.4	-4.9	36.4
BH&HLYP[a]	52.9	64.3	0.0	32.8	-1.6	54.5	-0.8	40.6
PW91[b]	67.6	68.3	0.0	12.8	-19.5	40.1	-11.7	33.6
PW91[c]	69.8	69.0	0.0	19.6	-0.7	46.0	2.9	38.8
PW91[d]	66.1	68.1	0.0	19.8	0.0	46.5	4.0	39.6
CCSD(T)[a]	49.3	67.3	0.0	29.7	2.0	----[f]	2.9	46.4
CCSD(T)[e]	60.4	72.4	0.0	29.7	0.4	----[f]	2.3	44.5
$<S^2>$ [g]	1.3714	0.9457	0.7517	0.7516	0.7516	0.7588	0.7511	
PW91[h]	67.0	75.3	64.7					65.3
$<S^2>$ [i]	3.7525	3.7524	3.7527					2.0028+0.75

[a] SDD for Th and 6-311++G(d,p) for H & O atoms
[b] frozen core TZP for Th and TZ2P for H & O atoms
[c] frozen core TZP for Th and TZ2P for H & O atoms, ZORA-SR results
[d] frozen core TZP for Th and TZ2P for H & O atoms, ZORA-SO results
[e] estimated CCSD(T)/SDD+ energies using (1) formula
[f] Cannot be located; the bond dissociation appears to proceed without a reverse barrier
[g] Expectation value of S^2 for the doublet surface at the PW91/SDD level of theory
[h] Quartet surface at the PW91/SDD level of theory
[i] Expectation value of S^2 for the quartet surface at the PW91/SDD level of theory

The optimized geometries for the various stationary points are compared in Figure 6.1, and show relatively little dependence on the level of theory. For the minima, most bond lengths agree to within 0.01 Å and angles agree to ±1°. One exception is the Th-O bond length in complex **1**. Among the transition states, **TS1** shows some dependence on the level of theory, with the CCSD(T)/SDD calculations yielding a structure that is a bit later along the path toward $HThOH^+$. The transition state for H atom loss, **TS3**, could not be located at the CCSD(T)/SDD level, suggesting that O-H dissociation in $HThOH^+$ occurs without a reverse barrier. The vibrational frequencies for the stationary points calculated at the PW91/SDD level are listed in Table 6.2. Similar values are obtained with other levels of theory.

Table 6.2 Vibrational frequencies (cm^{-1}) of the stationary points at the PW91/SDD level[a]

1	TS1	2	TS2	3	TS3	$HThO^+$
326.1	939.7*i*	319.4	1296.4*i*	163.7	1275.8*i*	366.2
370.2	322.4	471.0	804.2	344.6	211.5	910.4
458.0	531.7	484.5	1024.3	419.5	264.1	1598.5
1577.0	984.0	700.2	1145.0	689.4	349.5	
3572.3	1597.5	1629.1	1489.2	902.5	814.6	
3658.9	3662.5	3723.1	1880.9	4113.9	1596.1	

[a] ThO^+ 930.7; H_2 4330.0

Dynamics

The formation of the initial Th-OH_2^+ complex is quite exothermic, and a conservative estimate is that **TS1** lies at least 20 kcal/mol below the reactants, $Th^+ + H_2O$.[21] Since an additional 66.4 kcal/mol is released in the formation of the $HThOH^+$ intermediate from **TS1**, at least 86.4 kcal/mol is available for the dissociation of the $HThOH^+$. The branching ratio for the $ThO^+ + H_2$ and $HThO^+ + H$ products can be estimated by RRKM theory.[47,48] Using the vibrational data in Table 6.2 and an initial energy of 86.4 kcal/mol, a branching ratio of 8:1 is calculated in favor of $HThO^+ + H$. At first this may seem at odds with the energetics in Figure 6.2, since the barrier for the $HThO^+ + H$ channel is about twice as high as the barrier for the $ThO^+ + H_2$ channel. However, **TS3** has three low frequency vibrations whereas **TS2** has none, resulting in a much higher density of states at the available energy. The branching ratio predicted by RRKM is contrary to the observed branching ratio, which favors $ThO^+ + H_2$. With the large excess energy and the small number of vibrational modes, the reaction may occur more rapidly than the energy redistribution, and a statistical treatment may no longer be valid.

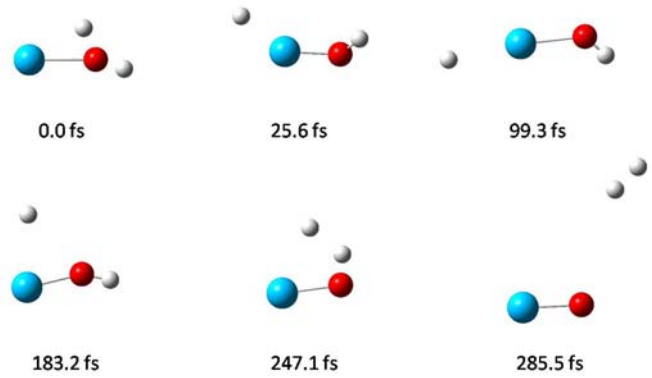

(a)

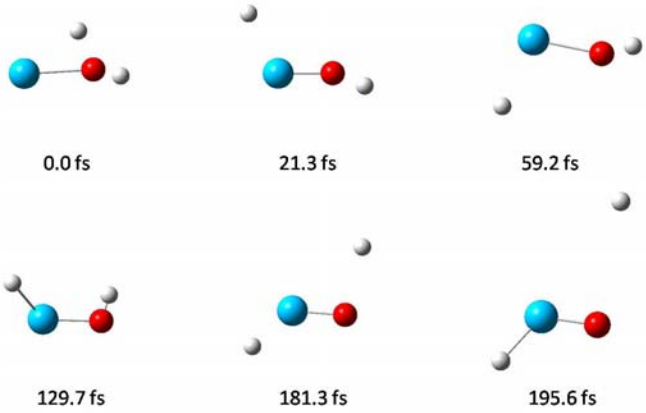

(b)

Figure 6.3 Snapshots of typical trajectories from the MD simulations. (a) $ThOH_2^+ \rightarrow ThO^+ + H_2$, (b) $ThOH_2^+ \rightarrow HThO^+ + H$.

To obtain a better description of the branching ratio, the molecular dynamics of the $Th^+ + H_2O$ reaction were simulated using ab initio classical trajectory calculations. The foregoing discussion of the energetics showed that the PW91/SDD level of theory is suitable and practical for simulating the molecular dynamics (MD) of the $ThOH_2^+$ dissociation. Because the $Th^+ + H_2O$ reactants are at least 20 kcal/mol above **TS1**, the trajectories were started at the **TS1** with 20 kcal/mol extra energy distributed microcanonically among the vibration modes along with the transition vector. A total of 164 trajectories were integrated for up to 400 *fs*. The H_2 molecular elimination channel is dominant with a branching ratio of 41.5% compared to 6.7% for the H atom elimination channel. However, 51.8% trajectories do not dissociate in a simulation time of ca. 400 *fs*, and stayed in isomer **2**. Isomer **2** is a deep well on the potential energy surface and longer simulation times are needed for these trajectories to dissociate. We chose 16 of these unreactive trajectories and integrated them for an additional 800 *fs*; 11 produced $ThO^+ + H_2$, 4 yielded $HThO^+ + H$ and 1 still did not dissociate. If the remaining trajectories dissociate with a similar ratio, the average branching ratio is ca 80% for $ThO^+ + H_2$ and ca 20% for $HThO^+ + H$.

Two representative snapshots for H_2 molecular and H atomic elimination processes are shown in Figure 6.3 (the corresponding movies are available on the ACS website). The time to reach isomer **2** from **TS1** is relatively short but dissociation of isomer **2** takes a longer time because it is in a fairly deep well. Both of the dissociation channels are exothermic compared to $Th^+ + H_2O$, but **TS3** lies considerably higher in energy than **TS2**. Insertion of Th^+ into H_2O to

form $HThOH^+$ does not directly activate the OH bond that dissociates to form $HThO^+$ + H. However, the H bending modes are activated by the insertion, facilitating the two H atoms to come together to form an H-H bond.

6.4 Conclusions:

The energetics of dissociation have been studied by a number of DFT and CCSD(T) levels of theory. Although the various theoretical methods show some differences in the relative energies, the PW91/SDD level of theory provides a good compromise between accuracy and practicality. Both the H_2 molecular and H atom elimination channels are thermodynamically accessible, with a lower barrier for the former channel. The ab initio molecular dynamics study finds a branching ratio of ca 80% for the H_2 molecular elimination reaction versus ca 20% for the H atomic elimination reaction, compared with a branching ratio of 65% to 35%, respectively, observed in FTICR/MS experiments.

6.5 References

(1) Gibson, J. K.; Haire, R. G.; Marçalo, J.; Santos, M.; Leal, J. P.; Pires de Matos, A.; Tyagi, R.; Mrozik, M. K.; Pitzer, R. M.; Bursten, B. E. *Eur. Phys. J. D* **2007**, *45*, 133-138.

(2) Gibson, J. K.; Marçalo, J. *Coord. Chem. Rev.* **2006**, *250*, 776-783.

(3) Gibson, J. K. *Int. J. Mass Spectrom.* **2002**, *214*, 1-21.

(4) Gibson, J. K.; Haire, R. G. *Inorg. Chem.* **2002**, *41*, 5897-5906.

(5) Gibson, J. K.; Haire, R. G. *Radiochimica Acta* **2003**, *91*, 441-448.

(6) Gibson, J. K.; Haire, R. G. *Organometallics* **2005**, *24*, 119-126.

(7) Santos, M.; Marçalo, J.; Leal, J. P.; Pires de Matos, A.; Gibson, J. K.; Haire, R. G. *Int. J. Mass Spectrom.* **2003**, *228*, 457-465.

(8) Santos, M.; Marçalo, J.; Pires de Matos, A.; Gibson, J. K.; Haire, R. G. *J. Phys. Chem. A* **2002**, *106*, 7190-7194.

(9) Cornehl, H. H.; Wesendrup, R.; Diefenbach, M.; Schwarz, H. *Chem. Eur. J.* **1997**, *3*, 1083-1090.

(10) Gibson, J. K.; Haire, R. G.; Santos, M.; Marçalo, J.; Pires de Matos, A. *J. Phys. Chem. A* **2005**, *109*, 2768-2781.

(11) Gibson, J. K.; Haire, R. G.; Marçalo, J.; Santos, M.; Pires de Matos, A.; Mrozik, M. K.; Pitzer, R. M.; Bursten, B. E. *Organometallics* **2007**, *26*, 3947-3956.

(12) Heinemann, C.; Cornehl, H. H.; Schwarz, H. *J. Organomet. Chem.* **1995**, *501*, 201-209.

(13) Marçalo, J.; Leal, J. P.; Pires de Matos, A. *Int. J. Mass Spectrom.* **1996**, *157*, 265-274.

(14) Marçalo, J.; Leal, J. P.; Pires de Matos, A.; Marshall, A. G. *Organometallics* **1997**, *16*, 4581-4588.

(15) Jackson, G. P.; King, F. L.; Goeringer, D. E.; Duckworth, D. C. *J. Phys. Chem. A* **2002**, *106*, 7788-7794; *108*, 2139.

(16) Jackson, G. P.; Gibson, J. K.; Duckworth, D. C. *Int. J. Mass Spectrom.* **2002**, *220*, 419-441.

(17) Jackson, G. P.; Gibson, J. K.; Duckworth, D. C. *J. Phys. Chem. A* **2004**, *108*, 1042-1051.

(18) Michelini, M. C.; Russo, N.; Sicilia, E. *Angew. Chem. Int. Ed.* **2006**, *45*, 1095-1099.

(19) Michelini, M. C.; Russo, N.; Sicilia, E. *J. Am. Chem. Soc.* **2007**, *129*, 4229-4239.

(20) Alikhani, M. E.; Michelini, M. C.; Russo, N.; Silvi, B. *J. Phys. Chem. A* **2008**, *112*, 12966-12974.

(21) Mazzone, G.; Michelini, M. C.; Russo, N.; Sicilia, E. *Inorg. Chem.* **2008**, *47*, 2083-2088.

(22) Becke, A. D. *J. Chem. Phys.* **1993**, *98*, 1372-1377.

(23) Becke, A. D. *J. Chem. Phys.* **1993**, *98*, 5648-5652.

(24) Lee, C.; Yang, W.; Parr, R. G. *Phys. Rev. B* **1988**, *37*, 785.

(25) Perdew, J. P.; Chevary, J. A.; Vosko, S. H.; Jackson, K. A.; Pederson, M. R.; Singh, D. J.; Fiolhais, C. *Phys. Rev. B* **1992**, *46*, 6671-6687.

(26) Perdew, J. P.; Burke, K.; Wang, Y. *Phys. Rev. B* **1996**, *54*, 16533-16539.

(27) Tao, J.; Perdew, J. P.; Staroverov, V. N.; Scuseria, G. E. *Phys. Rev. Lett.* **2003**, *91*, 146401.

(28) Boese, A. D.; Jan, M. L. M. *J. Chem. Phys.* **2004**, *121*, 3405-3416.

(29) Kuchle, W.; Dolg, M.; Stoll, H.; Preuss, H. *J. Chem. Phys.* **1994**, *100*, 7535-7542.

(30) Frisch, M. J.; Trucks, G. W.; Schlegel, H. B.; et al. Gaussian DV; Revision F.02 ed.; Gaussian, Inc.: Wallingford, CT, 2007.

(31) Velde, G. T.; Bickelhaupt, F. M.; Baerends, E. J.; Guerra, C. F.; Van Gisbergen, S. J. A.; Snijders, J. G.; Ziegler, T. *J. Comput. Chem.* **2001**, *22*, 931-967.

(32) Guerra, C. F.; Snijders, J. G.; te Velde, G.; Baerends, E. J. *Theor. Chem. Acc.* **1998**, *99*, 391-403.

(33) ADF; ADF2007.01 ed.; SCM, Theoretical Chemistry, Vrije Universiteit,: Amsterdam, The Netherlands, http://www.scm.com.

(34) Pople, J. A.; Head-Gordon, M.; Raghavachari, K. *J. Chem. Phys.* **1987**, *87*, 5968-5975.

(35) Werner, H.-J.; Knowles, P. J.; Lindh, R.; et al. MOLPRO version 2006.1. A package of ab initio programs.

(36) Curtiss, L. A.; Raghavachari, K.; Pople, J. A. *J. Chem. Phys.* **1993**, *98*, 1293-1298.

(37) Curtiss, L. A.; Redfern, P. C.; Raghavachari, K.; Rassolov, V.; Pople, J. A. *J. Chem. Phys.* **1999**, *110*, 4703-4709.

(38) Bakken, V.; Millam, J. M.; Schlegel, H. B. *J. Chem. Phys.* **1999**, *111*, 8773-8777.

(39) Millam, J. M.; Bakken, V.; Chen, W.; Hase, W. L.; Schlegel, H. B. *J. Chem. Phys.* **1999**, *111*, 3800-3805.

(40) Stoer, J.; Bulirsch, R. *Introduction to Numerical Analysis*; Springer-Verlag: New York, 1980.

(41) Hase, W. L. Classical Trajectory Simulations: Initial Conditions. In *Encyclopedia of Computational Chemistry*; Schleyer, P. v. R., Allinger, N. L., Clark, T., Gasteiger, J., Kollman, P. A., Schaefer III, H. F., Schreiner, P. R., Eds.; Wiley: Chichester, 1998; pp 402-407.

(42) Peslherbe, G. H.; Wang, H.; Hase, W. L. *Adv. Chem. Phys.* **1999**, *105*, 171-201.

(43) Anand, S.; Schlegel, H. B. *Phys. Chem. Chem. Phys.* **2004**, *6*, 5166-5171.

(44) Zhou, J.; Schlegel, H. B. *J. Phys. Chem. A* **2008**, *112*, 13121-13127.

(45) Lee, T. J.; Taylor, P. R. *Int. J. Quantum Chem.* **1989**, 199-207.

(46) Rienstra-Kiracofe, J. C.; Allen, W. D.; Schaefer, H. F. *J. Phys. Chem. A* **2000**, *104*, 9823-9840.

(47) Marcus, R. A.; Rice, O. K. *J. Phys. Chem.* **1951**, *55*, 894-908.

(48) Steinfeld, J. I.; Francisco, J. S.; Hase, W. L. *Chemical Kinetics and Dynamics*, 2nd ed.; Prentice Hall: Upper Saddle River, N.J., 1999.

CHAPTER 7

THEORETICAL STUDIES OF $An^{II}_2(C_8H_8)_2$ (An = Th, Pa, U, AND Np) COMPLEXES: THE SEARCH FOR DOUBLE-STUFFED ACTINIDE METALLOCENES

7.1 Introduction:

The subject of metal-metal multiple bonds has received a great deal of attention from both experimentalists and theoreticians since Cotton's 1964 discovery of the δ bond in $[Re_2Cl_8]^{2-}$.[1] Although metal-metal multiple bonds abound in the transition metals,[2,3] molecules containing unambiguous actinide-actinide bonds are limited. In 1974 uranium dimer, U_2, and U_2O_2 were detected in the gas phase via mass spectrometry, but were not isolated.[4] More recently, Andrews et al. have detected, but not crystallized, $U^I(\mu\text{-}H)_2U^I$ in both solid Ar and Ne.[5,6] Progress has been made in preparing and structurally characterizing U-M bonds for main group metals.[7-10] However, creating an isolatable molecule containing actinide-actinide bonds that can be crystallized is still a cutting edge problem requiring synergistic efforts between experiment and theory.

Bursten and co-workers were the first to theoretically investigate U_2 and found that six of the twelve valence electrons occupy the $7s\sigma_g$ and $6d\pi_u$ orbitals.[11-13] Gagliardi and Roos confirmed these results with state of the art calculations and predicted that U_2 forms a quintuple bond with a dissociation energy of 127 kJ/mol.[14] Roos and co-workers expanded their investigation and

showed that Ac_2, Th_2, and Pa_2 will form double, quadruple, and quintuple bonds, respectively.[15] They also predicted that $[U_2]^{2+}$ is a metastable species with a triple bond that could be stabilized by complexation with chloride, carboxylate or phenyl ligands.[16-18] Kaltsoyannis et al. studied the series M_2X_6 (M = U, W, Mo; X = Cl, F, OH, NH_2, CH_3) and $[M_2X_8]^{2-}$ (M = U, Np, Pu, Mo, Tc, Ru, W, Re, Os; X = Cl, Br, I) with density functional and multiconfigurational methods and found multiple metal-metal bonds exist in all species.[19,20] Straka and Pyykkö demonstrated that $HTh^{I}Th^{I}H$ is linear, unlike $U^{I}(\mu\text{-}H)_2U^{I}$ [5], and has a Th-Th triple bond.[21] They point out that $HTh^{I}Th^{I}H$ may already have been seen in a solid Ar matrix and that it is stabilized by ligands other than hydrogen.[21] Wu and Lu have calculated $U_2@C_{60}$, showing that U_2 forms multiple bonds when encased endohedrally in a small fullerene.[22] However, for larger fullerenes such as C_{70} and C_{84}, Infante, Gagliardi and Scuseria have demonstrated that the U-U bond no longer exists because the individual atoms bind preferentially to the inner walls of the fullerenes.[23] The binding of actinides in smaller organometallic complexes is somewhat different. Infante et al. predicted that $An_2(C_6H_6)_2$ complexes will be more stable than two isolated MC_6H_6 monomers for M = Th and U.[24] In spite of all these theoretical efforts, the best ligand set for stabilizing actinide-actinide multiple bonds is still elusive, but recent experimental advances are hinting at new alternatives.

The discovery of $Zn^{I}_2(\eta^5\text{-}C_5Me_5)_2$ and its derivatives has fundamentally changed the definition of metallocene by introducing bimetallic units to the center of the classic sandwich complex.[25-27] Although no other dimetallocenes are

experimentally known so far, a plethora of theoretical work has predicted that such molecules should exist for a variety of alkaline earth and transition metals.[26-42] Dimetallocenes may also exist for systems with rings that are not composed of carbon, such as hydrosilver, phosphorus, boron, and nitrogen.[43-46] Along with other recently synthesized $LM^{I}M^{I}L$ compounds, M = Cr[47] and Mg[48], these molecules demonstrate how this bonding motif can stabilize unusual, low-oxidation states of metals. Since metallocenes with D_{8h} symmetry employing COT (COT = $[C_8H_8]^{2-}$) rings have been synthesized for thorium, protactinium, uranium, neptunium, and plutonium,[49] actinide (An) dimers may be stabilized by two COT rings in a similar manner to $LM^{I}M^{I}L$ compounds thereby forming new dimetallocenes complexes that might be isolatable. In this work, density functional theory (DFT) methods are employed to study the possible sandwich compounds of $An_2(COT)_2$ (An = Th, Pa, U, Np). To the best of our knowledge, there is no other earlier work on this aspect.

7.2 Computational Methods:

All computations employed the hybrid B3LYP functional[50-52] and were carried out using the development version of Gaussian.[53] For the actinide atoms, scalar relativistic effects were taken into account via the relativistic effective core potential (RECP) of Küchle et al.[54] This RECP places 60 electrons in the actinide core leaving the 5*s*, 5*p*, 5*d*, 6*s*, 6*p*, 5*f*, 6*d*, and 7*s* electrons for explicit treatment. The most diffuse *s*, *p*, *d*, and *f* Gaussian functions of the associated actinide basis set were removed to generate the [*7s 6p 5d 3f*] basis that previously predicted accurate molecular structures.[55,56] Ligand atoms were described with

Dunning's cc-pVDZ basis set.[57] Pure *d* and *f* functions were used in all Gaussian basis sets. Harmonic vibrational frequencies were computed to confirm that each structure was a local minimum on the potential energy surface and to provide zero-point energy corrections. An integration grid with 400 radial shells and 770 angular points per shell was employed for all DFT calculations. The stability of each structure's density was tested using standard methods[58] and reoptimized if necessary. Natural population analysis[59] (NPA) was performed on each structure using a valence space composed of 5*f*, 6*d*, 7*s* and 7*p*.[60,61] GaussView was used to create all structure and molecular orbital pictures.[62] For diuranocene, calculations employing a frozen-core approximation[63] and the zero-order regular approximation[64-66] (ZORA) Hamiltonian to account for scalar relativistic effects were also run with the ADF code.[67] The BLYP[50,51] functional, a TZ2P ligand basis set along with a TZP uranium basis set were used for the ZORA calculations.

7.3 Results and Discussion

The formation of an actinocene, $An^{IV}(COT)_2$, is a well-known thermodynamic sink on the An plus COT potential energy surface. If the disproportionation channel converting $An^{II}_2(COT)_2$ to $An^{IV}(COT)_2$ can be cleverly disabled, then a rich field of actinide dimetallocene chemistry becomes accessible (*vide infra*). Because the uranium dimer has received more attention than other early An dimers, the discussion starts with $U_2(COT)_2$. Since proceeding to neptunium and beyond in the periodic table, places electrons in nonbonding *5f* φ orbitals, the maximum An-An bond order should be achieved in $U_2(COT)_2$ or $Np_2(COT)_2$. This is counterbalanced by contraction of the *5f* orbitals

with increasing atomic number, which diminishing the bond strength. Based upon the energetics of $U_2(COT)_2$ isomers, only coaxial structures for protactinium, neptunium and thorium are presented. The energy difference between the D_{8d} and D_{8h} coaxial conformers is very small ($\Delta G(0K)$ = 0.071 kJ/mol for Pa) as expected based on the actinocene crystal structures,[68-73] so only D_{8h} coaxial species were investigated. The thorium complex is unusual in comparison to the other early actinides and so is described last.

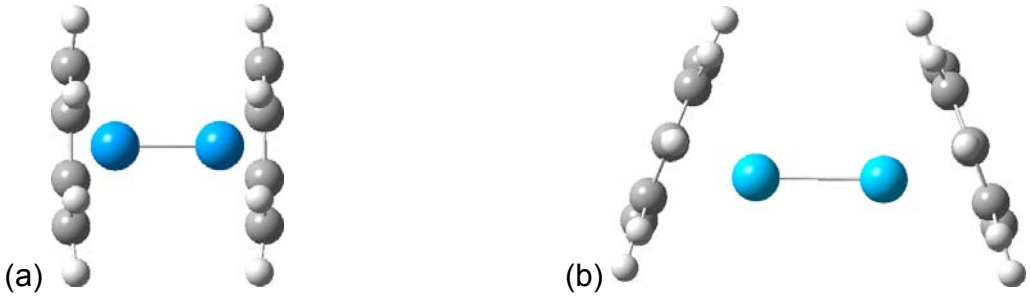

Figure 7.1 Optimized structures of (a) D_{8h} $An_2(COT)_2$ (An = Pa, U, and Np) and (b) C_{2v} $Th_2(COT)_2$ with C and H atoms denoted in black and white, respectively.

7.3.1 Uranium

Based upon Gagliardi's work[11,14] we expect the U_2 complexes to be stable. A coaxial arrangement, where the uranium atoms lie along the C_8 rotational axis of the COT rings, leads to a $^3A_{1g}$ predicted ground state (see Figure 7.1) with D_{8h} symmetry. The value of S^2 is 2.024 and orbital stability analysis indicates that the triplet wave function is stable (the quintet state is 63 kJ/mol higher). The U-U bond length of 2.240 Å (Table 7.1) is at least a U-U triple bond, based upon a U triple-bond covalent radius of 1.18 Å.[74] This bond length agrees rather well with the ZORA-BLYP result of 2.285 Å. With a U to ring centroid distance only 0.065 Å longer than in the crystal structure of uranocene,[70] and 0.021 Å longer than in uranocene (1.968 Å) at the same level of theory, $U_2(\eta^8\text{-COT})_2$ can be accurately described as a dimer of two UCOT half-sandwich complexes. The COT ring remains almost the same in diuranocene compared to that in uranocene: the C-C bond is 1.415 Å in diuranocene while the C-C bonds are 1.416 Å in uranocene, and C-H bond is 1.093 Å in both diuranocene and uranocene. Furthermore, the U-C distance is 2.715 Å in diuranocene, while it is only 0.015 Å shorter in uranocene. $U_2(COT)_2$ can be described equally well as $[U_2]^{4+}$ complexed with two COT ligands. The U-U bond in $U_2(COT)_2$ (2.240 Å) is nearly the same as in $[U_2]^{4+}$ (2.297 Å). This indicates that the strength of the U-U bond originates from the stability of $[U_2]^{4+}$ and not from its interactions with the COT ligands.

Table 7.1 Calculated Gas-phase Bond Lengths (Å), Bond Angles (º), Natural Charges (e) and Vibrational Frequencies (cm^{-1}) for $An_2(COT)_2$ Complexes with Vibrational Mode Symmetries in Parentheses

An	Symmetry	An-An	An-X[a]	HCX[a]	AnAnX[a]	An Natural Charge	An-An ν_{sym}
Th	$C_{2v}\ ^3B_1$	2.809	2.029	5.4	158.4	0.86	249(A_1)
Pa	$D_{8h}\ ^5A_{1g}$	2.537	1.998	4.8	180.0	0.93	270(A_{1g})
U	$D_{8h}\ ^3A_{1g}$	2.240	1.989	5.7	180.0	0.77	349(A_{1g})
Np	$D_{8h}\ ^5A_{1g}$	2.189	1.938	5.8	180.0	0.80	354(A_{1g})

[a] X is the centroid of the COT ring

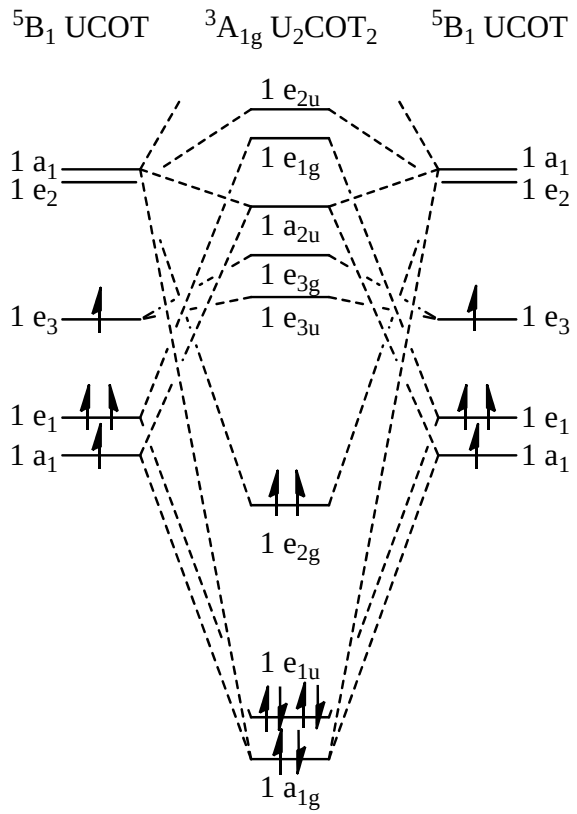

Figure 7.2 Qualitative canonical MO diagram showing the interaction of two $^5B_1$ UCOT monomers under single-group C_{8v} symmetry to form $^3A_{1g}$ $U_2(\eta^8\text{-COT})_2$ under single-group D_{8h} symmetry. Only the U 5*f* electron manifold of U_2COT_2 is shown for clarity (see text). Orbital energies are taken as the average of the α and β components. Since the UCOT density breaks symmetry, the closest C_{8v} symmetry labels are used.

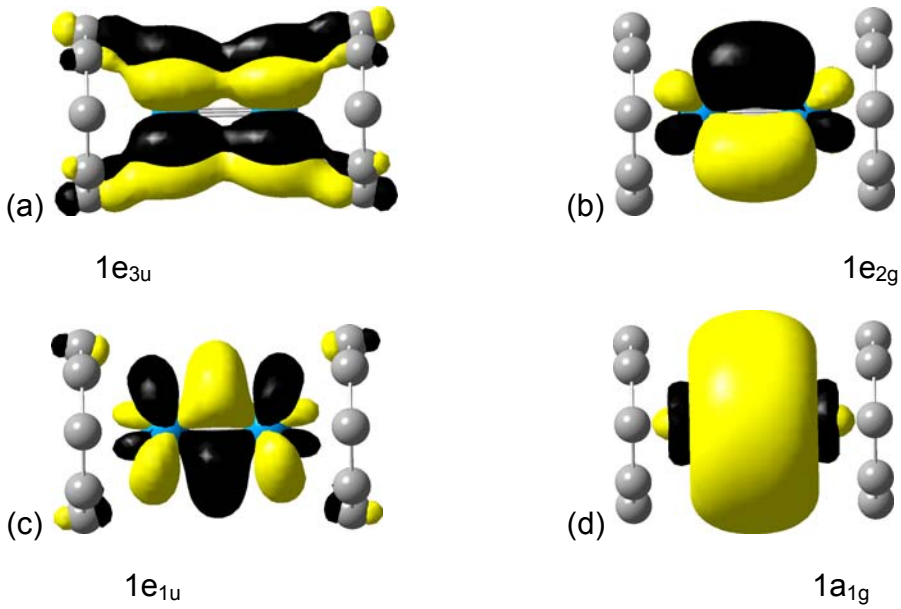

Figure 7.3 Selected D_{8h} $U_2(COT)_2$ α molecular orbitals (a) LUMO, (b) HOMO, (c) HOMO-1, and (d) HOMO-2 plotted at an isovalue of 0.02. Hydrogens were omitted for clarity.

Each UCOT monomer has four U valence electrons available for metal-metal bonding. The quintet state is the most stable and has one electron in an *s* plus *f* σ-type orbital and two unpaired electrons in the *f* π-type orbitals and one electron in an *f* φ-type orbital (See Figure 7.2). Under C_{8v} symmetry, these orbitals are $1a_1$, $1e_2$ and $1e_3$, respectively. When two UCOT monomers brought together to form a $U_2(COT)_2$ dimer, these eight U *f* electrons occupy five bonding molecular orbitals (MOs) for an electron configuration of $\sigma^2\pi^4\delta^2$ and a formal U-U bond order of 4. Natural Population Analysis yields a Wiberg bond order of 4.3 for this interaction. The U-U bonding MOs are shown in Figure 7.3 and it is interesting to compare them to those previously reported for U_2[11,14] and $[U_2]^{2+}$.[16] The $1a_{1g}$ MO is the U-U σ bond formed from the in-phase mixing of the UCOT $1a_1$ group orbitals. This same MO is seen in both U_2 and $[U_2]^{2+}$ where the authors' orbital assignment indicates that the *7s* contribution was perceived to be larger than the $5f_\sigma$ contribution.[14,16] The $1e_{1u}$ orbital in U_2COT_2 is a π-type metal-metal bonding MO formed from U $5f_\pi$ atomic orbitals. This U-U bonding MO was also found in U_2, $[U_2]^{2+}$ and diuranium tetraformate; since the *6d* contribution appeared to be larger than the $5f_\pi$, the orbital was designated $6d_\pi$.[16,17] It should be noted that MO pictures can be deceiving. For example, Figure 7.4 shows that the choice of isovalue can artificially suggest a larger *s* contribution than is borne out by the Mulliken percent character analysis (See Table 7.2). As indicated by the Mulliken percent character, the $1\sigma_g$ orbitals of $[U_2]^{4+}$ and the $1a_{1g}$ orbital in U_2COT_2 are better described as $5f_\sigma$; likewise the $1\pi_u$ and $1e_{1u}$ orbitals should be

designated $5f_{\pi}$. The $1e_{2g}$ MO is the U-U δ bond formed from the in-phase combination of $5f_{\delta}$ atomic orbitals and is also present in U_2 and $[U_2]^{2+}$. The gerade and ungerade combinations of the formally non-bonding U $5f_{\varphi}$ orbitals lead to the $1e_{3u}$ and $1e_{3g}$ MOs that are also seen in U_2 and $[U_2]^{2+}$. Although spin-orbit coupling should not significantly affect molecular geometries,[75] it will remove the degeneracy of the e_{iu} and e_{ig}, i = 1-3, MOs. Depending upon the energy difference between the $e_{3/2g}$ and $e_{5/2g}$ D_{8h}^{*} double-group MOs resulting from the single-group $1e_{2g}$ MO, the ground state may be singlet , but this is not expected based upon the high-spin nature of free U_2.[14]

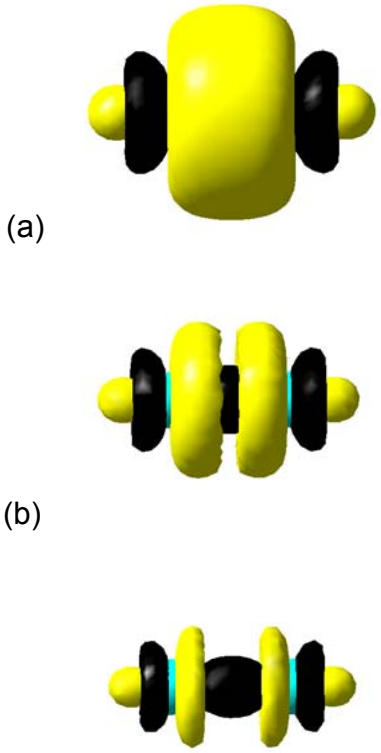

(a)

(b)

(c)

Figure 7.4 $1\sigma_g$ MO for triplet $[U_2]^{4+}$ plotted at an isovalue of (a) 0.02, (b) 0.04, and (c) 0.06.

Table 7.2 Actinide Mulliken % Character for Selected α MOs

MO	s	p	d	f	Assignment
$[U_2]^{4+}$ *$D_{\infty h}$ triplet*					
$1\pi_u$		1	40	59	$5f_\pi$
$1\sigma_g$	8	3	6	83	$5f_\sigma$
$1\delta_g$			5	95	$5f_\delta$
$Th^{II}{}_2(\eta^8\text{-COT})_2$ *D_{8h} triplet*					
$1a_{1g}$	50	0	24	16	$5f_\sigma$
$1e_{1u}$		4	56	32	$5f_\pi$
$1e_{2g}$			48	48	$5f_\delta$
$Pa^{II}{}_2(\eta^8\text{-COT})_2$ *D_{8h} quintet*					
$1a_{1g}$	34	4	6	56	$5f_\sigma$
$1e_{1u}$			20	76	$5f_\pi$
$1e_{2g}$			20	74	$5f_\delta$
$U^{II}{}_2(\eta^8\text{-COT})_2$ *D_{8h} triplet*					
$1a_{1g}$	34	6	14	46	$5f_\sigma$
$1e_{1u}$			24	70	$5f_\pi$
$1e_{2g}$			24	76	$5f_\delta$
$Np^{II}{}_2(\eta^8\text{-COT})_2$ *D_{8h} quintet*					
$1a_{1g}$	24	6	10	60	$5f_\sigma$
$1e_{1u}$			16	80	$5f_\pi$
$1e_{2g}$			22	76	$5f_\delta$

Based upon the work of Xie et al.[28] on Ni_2Cp_2 and Cu_2Cp_2 in which metal-metal bonds prefer to be perpendicular to the C_5 axis of the Cp rings and the work of Infante et al.[24] on $U_2(C_6H_6)_2$ and $Th_2(C_6H_6)_2$ where the An-An bonds are approximately perpendicular to the C_6 axis of the benzene rings, a second isomer of $U_2(COT)_2$ with the U-U bond perpendicular to the C_8 axis of the rings was also considered. Rotation of the U_2 unit in D_{8h} $U_2(\eta^8\text{-COT})_2$ by 90° generates a D_{2h} fifth-order saddle point (SP) 203 kJ/mol (ΔG(0K)) higher in energy than the D_{8h} isomer. The COT rings are slightly puckered in the D_{2h} isomer and the U-U bond has lengthened to 2.368 Å. Reducing the symmetry constraints to C_{2h} produces a lower energy (ΔG(0K) = 138 kJ/mol), third-order SP in which two of the eight C atoms in each ring bend out of plane by 44° and the U-U bond is 2.811Å. Further reduction of symmetry constraints increases the out-of-plane bending to 52° and forms a C_s structure 28.0 kJ/mol (ΔG(0K)) *higher* in energy than the coaxial isomer. This energetic ordering of coaxial diuranocene more stable than perpendicular diuranocene is the opposite of Cu and Ni M_2Cp_2 complexes where the perpendicular isomers are predicted to be more stable than the coaxial species. Diuranocene is more like Zn_2Cp_2, for which the coaxial structure is stable but perpendicular complex is not a stationary point.[28]

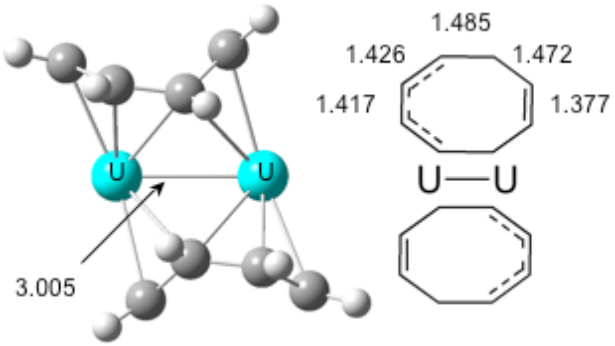

Figure 7.5 Perpendicular geometry for C_s $U_2(\mu\text{-}\eta^6,\eta^4\text{-}C_8H_8)_2$ that is 28 kJ/mol higher in energy than the coaxial isomer. Bond distances are in Angstroms. The U-C bonds range from 2.474 to 2.748 Å and the C-C bond values are averaged over the two rings.

As seen in Figure 7.5, the COT ring aromaticity is perturbed upon bending and the rings have slipped from η^8 to μ-η^6,η^4. This reduced hapticity is a slight perturbation of the more common μ-η^5,η^5 interaction seen in $M_2(\mu\text{-}\eta^5,\eta^5\text{-COT})R_n$ (M=Cr, Mo, W; R=COT, $OCH_2{}^tBu$, O^iPr, O^tBu) compounds.[76-78] In these compounds, X-ray crystallography showed the pair of closely bonded metal atoms lies over one sharply folded COT ring, and each metal atom symmetrically bonds to five carbon atoms of this COT ring. Each metal atom also is attached to the R group. However, in our C_s conformer each ring can still interact with both metals since six U-C distances are less than 2.72 Å to one of the U atoms and four U-C distances are less than 2.75 Å to the other, compared with 2.715 Å in D_{8h} $U_2(\eta^8\text{-COT})_2$. The COT ligand in the perpendicular species can be compared to similar calculations on the free C_8H_8 ring, a.k.a. neutral [8]annulene, which adopts a ground state D_{2d} geometry with alternating carbon single and double bonds of 1.475 and 1.345 Å respectively, and puckers to a boat-like structure, consistent with experiment values. Thus the C_8H_8 rings in the C_s isomer are best envisioned as the marriage of a delocalized butadiene unit and half of a slightly distorted [8]annulene ring. As expected for delocalized π systems, the COT rings in uranocene and diuranocene have C-C bond lengths of 1.416 and 1.415 Å, respectively. Due to the complex nature of the C_s isomer and its degree of spin-contamination, multi-reference methods may be required for more detailed studies.

In the D_{8h} isomer, the natural charge on each U, C, and H is 0.77, -0.35, and 0.25, respectively. In the C_s complex, the U charge increases to 1.04 and 1.16 indicating that 0.66 electrons from the two rings moved unequally to the U centers. The ligand to metal electron migration is also manifested in the 3.005 Å U-U bond, which is approximately a single bond as indicated by a Wiberg NPA bond order of 0.92. Such shifting of electron density reflects the drastic change in metal-ligand orbital overlap arising from rotation of the U_2 moiety. When the metals are coaxial, the uranium *d* and *f* electrons can interact with the COT ring group orbitals. After rotation these metal-based electrons are forced to interact with the individual π-electrons on the carbon atoms resulting in the movement of electron density, elongation of the U-U bond, and distortion of the COT ring.

In the gas-phase, the $U_2(C_8H_8)_2$ dimers are more stable than their separated monomers by 77.7 kJ/mol (ΔG(0K)) for the coaxial D_{8h} isomer, $^3A_{1g}$ $U_2(\eta^8\text{-COT})_2 \rightarrow 2\ ^5B_1$ UCOT, and 49.8 kJ/mol for the perpendicular C_s isomer, $^3A'$ $U_2(C_8H_8)_2 \rightarrow 2\ ^5B_1$ UCOT. However, preparation of $U_2(COT)_2$ from two UCOT fragments is not practical because UCOT could dimerize in alternate ways (e.g. U-COT-U-COT) or could disproportionate. The disproportionation reaction $^3A_{1g}$ $U_2(\eta^8\text{-COT})_2 \rightarrow {}^3B_{2g}$ $U(\eta^8\text{-COT})_2 + {}^5A_{2u}$ U is predicted to be *endothermic* by 55.6 kJ/mol (ΔG(0K)). Utilizing a U_2 dissociation energy of 127.6 kJ/mol[14] the disproportionation, $2\ ^3A_{1g}$ $U_2(\eta^8\text{-COT})_2 \rightarrow 2\ ^3B_{2g}$ $U(\eta^8\text{-COT})_2 + U_2$, reaction enthalpy becomes -16.4 kJ/mol when U_2 is produced. Therefore, if $U_2(COT)_2$ can be prepared by a route not involving UCOT and if the disproportionation channel can be disabled, a whole new class of U_2 complexes

become accessible. We are currently studying the stability of other $U_m(COT)_n$ complexes.

7.3.2 Protactinium & Neptunium

Both Pa_2COT_2 and Np_2COT_2 adopt D_{8h} structures similar to coaxial U_2COT_2 shown Figure 7.1a. The key geometric parameters are presented in Table 7.1. Pa_2COT_2 has a singlet state with orbital occupancy $1a_{1g}^2\ 1e_{1u}^4$ and S^2 = 0.794; the quintet ($1a_{1g}^2\ 1e_{1u}^2\ 1e_{2g}^2$) is 7 kJ/mol lower and has S^2 = 6.041. Quintet Np_2COT_2 ($1a_{1g}^2\ 1e_{1u}^4\ 1e_{2g}^2\ 1e_{3u}^2$, S^2 = 6.054) is ca 115 kJ/mol more stable than the singlet ($1a_{1g}^2\ 1e_{1u}^4\ 1e_{2g}^4$, S^2 = 0.569). As a consequence of the spin-unrestricted formalism, there is additional orbital mixing in both quintets resulting in artefactual symmetry breaking. Since these systems are too large to treat with CASSCF, the high symmetry D_{8h} calculations are used for further discussions. As the atomic number increases from Pa to Np, the An-An bond distances decrease from 2.54 Å to 2.19 Å. Although the metal to ring bond also decreases, the change is an order of magnitude smaller. The C-H bonds bend out of the ring plane toward the actinide atom by about 5º. This kind of C-H bending has been described previously.[75,79] For large rings, the carbon *2p* π orbitals tip inward for maximum overlap with the metal orbitals, causing the C-H bonds to bend toward the metal. Although there are no accurate experimental atomic radii for the actinides, they were estimated by Slater to be 1.80 Å, 1.75 Å and 1.75 Å for Pa, U, and Np respectively.[80] These values are very similar because electrons are being filled into compact *5f* orbitals. A recent theoretical study shows that the range of the triple-bond covalent radii of the early actinides

is between 1.36 Å and 1.16 Å.[74] The calculated An-An distances in $Pa_2(COT)_2$, $U_2(COT)_2$ and $Np_2(COT)_2$ (2.54 Å, 2.24 Å and 2.08 Å) are significantly shorter than single bonds and are closer to the length expected for triple bonds. The trend in bond lengths indicates that the actinide-actinide bond strength and bond order increases as the atomic number increases and more electrons are filled into *5f* bonding orbitals. A corresponding increase in the An-An vibrational frequency (270, 349 and 354 cm^{-1}) confirms the strengthening of the An-An bond.

7.3.3 Thorium

In the D_{8h} Th complex, the $1a_{1g}$ orbital is higher in energy than $1e_{1u}$ orbital. However, the singlet with four electrons in the $1e_{1u}$ orbital is higher in energy than the triplet, with two unpaired electrons in the $1e_{1u}$ orbital and a pair of electrons in the $1a_{1g}$ orbital. The triplet D_{8h} complex is a second order saddle point with two degenerate imaginary frequencies, ca 15*i* cm^{-1} for tilting the COT rings away from the C_8 axis. The corresponding frequencies for the Pa, U, and Np complexes are all real (26, 26, and 29 cm^{-1}, respectively), indicating these structures are stable in the coaxial configuration. By following one of the degenerate imaginary vibrational modes, the triplet $Th_2(COT)_2$ optimizes to the structure shown in Figure 7.1b with C_{2v} symmetry and a Th-Th-X angle of 158.4º (X is the centroid of the COT ring). The Th-Th bond length is 2.809 Å and the distance between Th and the COT ring is 2.029 Å, in line with the trends seen for the other An_2COT_2 structures.

The HOMO of D_{8h} $Th_2(COT)_2$ corresponds to $1e_{1u}$ *5f* π-type orbital of the other diactinide metallocenes, but bending the structure lifts the original degeneracy and distorts its shape. Since the coaxial D_{8h} structure is only 2.6 kJ/mol higher than the bent C_{2v} structure, the molecule may be very floppy at room temperature. By contrast, $Pa_2(COT)_2$, $U_2(COT)_2$ and $Np_2(COT)_2$ have partially filled δ and φ HOMOs and are not stabilized by bending. Both coaxial and bent structures are usual for actinide complexes depending upon the competition between the ligand repulsion, bond stabilization and electron repulsion.[81,82]

7.3.4 Orbital Analysis

The frontier molecular orbital diagram for An_2COT_2 is presented in Figure 7.6 using the energies of the orbitals with significant *f* character from the high spin, high symmetry structures. The shapes of the orbitals of U_2COT_2 (Figure 7.3) are representative of the corresponding orbitals of the other An_2COT_2 complexes. As expected, the orbital energies decrease markedly as empty orbitals are populated. The $1a_{1g}$ orbital is doubly occupied for the entire series. It is higher than the $1e_{1u}$ orbital for Th and Pa but lower for U and Np. The Mulliken %*f* character (Table 7.2) of the $1a_{1g}$ orbital increases significantly from Th to Np while the %*s* character decreases. The $1e_{1u}$ orbital is an An-An π bonding orbital and is half filled for Th and Pa, and filled for U and Np. The $1e_{2g}$ δ bonding orbital is half filled for Pa, U and Np. Like the $1a_{1g}$ and $1e_{1u}$ orbitals, the Mulliken %*f* character of the $1e_{2g}$ orbital increase from Th to Np. The $1e_{3u}$ orbital is a φ non-bonding orbital that is empty for Th, Pa and U, but half filled for Np. These orbital

occupancies yield formal bond orders of 2, 3, 4 and 4 for Th_2COT_2, Pa_2COT_2, U_2COT_2 and Np_2COT_2, respectively. This compares well with the trend in An-An bond lengths: 2.81 Å, 2.54 Å, 2.24 Å and 2.19 Å, respectively. Adding a pair of electrons to a bonding orbital decreases the bond length by ca. 0.3 Å, while adding a pair of electrons to the non-bonding $1e_{3u}$ orbital (going from U_2COT_2 to Np_2COT_2) decreases the bond length by only 0.05 Å.

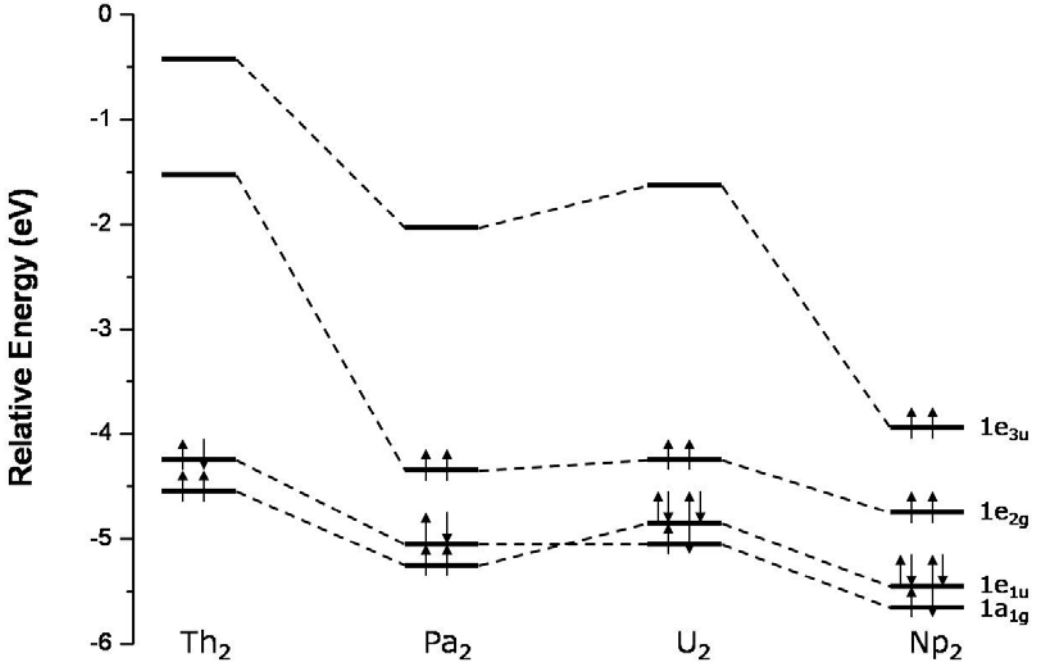

Figure 7.6 High spin D_{8h} An(II)$_2$(COT)$_2$ α frontier molecular orbital energy levels.

7.4 Conclusions:

The successful synthesis of decamethyldizincocene, supported by the robust theoretical investigations on its derivatives, suggests double-stuffed actinide metallocenes may be an interesting synthetic objective. Our studies show diuranocene is a D_{8h} coaxial minimum with a triplet ground state and a short U-U bond at the B3LYP level of theory while the perpendicular structure is higher in energy, has distorted COT rings and a longer U-U bond. Coaxial $U_2(COT)_2$ is stable with respect to dissociation into UCOT monomers. Disproportionation of $U_2(COT)_2$ is endothermic for uranocene plus U atom but slightly exothermic for uranocene plus 1/2 U_2. Similar coaxial diactinide structures have been obtained for Pa and Np, while the Th complex adopts a bent C_{2v} structure. Calculations show that as the atomic number increases, more electrons are filled into An-An *5f* π- and δ-type bonding orbitals. Consequently, the An-An distance decreases from 2.81 Å to 2.19 Å for $Th_2(COT)_2$ to $Np_2(COT)_2$, respectively, and the An-An stretching frequency increases from 249 cm^{-1} to 354 cm^{-1}. Without doubt, designing synthetic routes to complexes containing actinide-actinide bonds will require clever thinking. Hopefully the present computational study combined with recent low-oxidation state *f*-element chemistry advances in the Evans group[83] will stimulate experimental endeavors to prepare this new class of diactinide complexes.

7.5 References

(1) Cotton, F. A.; Curtis, N. F.; Harris, C. B.; Johnson, B. F. G.; Lippard, S. J.; Mague, J. T.; Robinson, W. R.; J., W. *Science* **1964**, *145*, 1305-1307.

(2) Chisholm, M. H.; Macintosh, A. M. *Chem. Rev.* **2005**, *105*, 2949-2976.

(3) Cotton, F. A.; Murillo, C. A.; Walton, R. A. *Multiple bonds between metal atoms*; 3rd ed.; Springer Science and Business Media, Inc.: New York, 2005.

(4) Gorokhov, L. N.; Emel'yanov, A. M.; Khodeev, Y. S. *Teplofiz. Vys. Temp.* **1974**, *12*, 1307-1309.

(5) Souter, P. F.; Kushto, G. P.; Andrews, L.; Neurock, M. *J. Am. Chem. Soc.* **1997**, *119*, 1682-1687.

(6) Raab, J.; Lindh, R. H.; Wang, X.; Andrews, L.; Gagliardi, L. *J. Phys. Chem. A* **2007**, *111*, 6383-6387.

(7) Porchia, M.; Casellato, U.; Ossola, F.; Rossetto, G.; Zanella, P.; Graziani, R. *J. Chem. Soc.-Chem. Commun.* **1986**, 1034-1035.

(8) Minasian, S. G.; Krinsky, J. L.; Williams, V. A.; Arnold, J. *J. Am. Chem. Soc.* **2008**, *130*, 10086-+.

(9) Minasian, S. G.; Krinsky, J. L.; Rinehart, J. D.; Copping, R.; Tyliszczak, T.; Janousch, M.; Shuh, D. K.; Arnold, J. *J. Am. Chem. Soc.* **2009**, *131*, 13767-13783.

(10) Liddle, S. T.; McMaster, J.; Mills, D. P.; Blake, A. J.; Jones, C.; Woodul, W. D. *Angew. Chem. Int. Ed.* **2009**, *48*, 1077-1080.

(11) Bursten, B. E.; Ozin, G. A. *Inorg. Chem.* **1984**, *23*, 2910-2911.

(12) Pepper, M.; Bursten, B. E. *J. Am. Chem. Soc.* **1990**, *112*, 7803-7804.

(13) Kaltsoyannis, N.; Hay, P. J.; Li, J.; Blaudeau, J.-P.; Bursten, B. E. Theoretical studies of the electronic structure of compounds of the actinide elements. In *The chemistry of the actinide and transactinide elements*; 3rd ed.; Morss, L. R., Edelstein, N. M., Fuger, J., Eds.; Springer: 2006; Vol. 3, p 1893-2012.

(14) Gagliardi, L.; Roos, B. O. *Nature* **2005**, *433*, 848-851.

(15) Roos, B. O.; Malmqvist, P.-Å.; Gagliardi, L. *J. Am. Chem. Soc.* **2006**, *128*, 17000-17006.

(16) Gagliardi, L.; Pyykkö, P.; Roos, B. O. *Phys. Chem. Chem. Phys.* **2005**, *7*, 2415-2417.

(17) Roos, B. O.; Gagliardi, L. *Inorg. Chem.* **2006**, *45*, 803-807.

(18) La Macchia, G.; Brynda, M.; Gagliardi, L. *Angew. Chem. Int. Ed.* **2006**, *45*, 6210-6213.

(19) Kaltsoyannis, N.; Cavigliasso, G. *Dalton Trans.* **2006**, 5476-5483.

(20) Kaltsoyannis, N.; Cavigliasso, G. *Inorg. Chem.* **2006**, *45*, 6828-6839.

(21) Straka, M.; Pyykkö, P. *J. Am. Chem. Soc.* **2005**, *127*, 13090-13091.

(22) Wu, X.; Lu, X. *J. Am. Chem. Soc.* **2007**, *129*, 2171-2177.

(23) Infante, I.; Gagliardi, L.; Scuseria, G. E. *J. Am. Chem. Soc.* **2008**, *130*, 7459-7465.

(24) Infante, I.; Raab, J.; Lyon, J. T.; Liang, B.; Andrews, L.; Gagliardi, L. *J. Phys. Chem. A* **2007**, *111*, 11996-12000.

(25) Resa, I.; Carmona, E.; Gutierrez-Puebla, E.; Monge, A. *Science* **2004**, *305*, 1136-1138.

(26) del Rio, D.; Galindo, A.; Resa, I.; Carmona, E. *Angew. Chem. Int. Ed.* **2005**, *44*, 1244-1247.

(27) Grirrane, A.; Resa, I.; Rodriguez, A.; Carmona, E.; Alvarez, E.; Gutierrez-Puebla, E.; Monge, A.; Galindo, A.; del Rio, D.; Andersen, R. A. *J. Am. Chem. Soc.* **2007**, *129*, 693-703.

(28) Xie, Y. M.; Schaefer, H. F.; King, R. B. *J. Am. Chem. Soc.* **2005**, *127*, 2818-2819.

(29) Pandey, K. K. *J. Organomet. Chem.* **2007**, *692*, 1058-1063.

(30) Kan, Y. H. *J. Mol. Struct.-Theochem* **2007**, *805*, 127-132.

(31) Zhou, J.; Wang, W. N.; Fan, K. N. *Chem. Phys. Lett.* **2006**, *424*, 247-251.

(32) Liu, Z. Z.; Tian, W. Q.; Feng, J. K.; Zhang, G.; Li, W. Q. *J. Mol. Struct.-Theochem* **2006**, *758*, 127-138.

(33) Kress, J. W. *J. Phys. Chem. A* **2005**, *109*, 7757-7763.

(34) Xie, Z. Z.; Fang, W. H. *Chem. Phys. Lett.* **2005**, *404*, 212-216.

(35) Philpott, M. R.; Kawazoe, Y. *J. Mol. Struct.-Theochem* **2006**, *776*, 113-123.

(36) Philpott, M. R.; Kawazoe, Y. *J. Mol. Struct.-Theochem* **2006**, *773*, 43-52.

(37) Philpott, M. R.; Kawazoe, Y. *Chem. Phys.* **2006**, *327*, 283-290.

(38) Philpott, M. R.; Kawazoe, Y. *Materials Transactions* **2007**, *48*, 693-699.

(39) Philpott, M. R.; Kawazoe, Y. *Chem. Phys.* **2007**, *333*, 201-207.

(40) Kua, J.; Tomlin, K. M. *J. Phys. Chem. A* **2006**, *110*, 11988-11994.

(41) Wang, H. M.; Yang, C. L.; Wan, B. S.; Han, K. L. *J. Theor. & Comput. Chem.* **2006**, *5*, 461-473.

(42) Xu, B.; Li, Q. S.; Xie, Y.; King, R. B.; Schaefer, H. F. *J. Chem. & Theory Comput.* **2010**, *6*, 735-746.

(43) Zhou, J.; Xiao, F.; Liu, Z. P.; Fan, K. N. *J. Mol. Struct.-Theochem* **2007**, *808*, 163-166.

(44) Liu, Z. Z.; Tian, W. Q.; Feng, J. K.; Li, W. Q.; Cui, Y. H. *J. Mol. Struct.-Theochem* **2007**, *809*, 171-179.

(45) Li, Q. S.; Xu, Y. *J. Phys. Chem. A* **2006**, *110*, 11898-11902.

(46) Zhang, X. H.; Li, S.; Li, Q. S. *J. Theor. & Comput. Chem.* **2006**, *5*, 475-487.

(47) Nguyen, T.; Sutton, A. D.; Brynda, M.; Fettinger, J. C.; Long, G. J.; Power, P. P. *Science* **2005**, *310*, 844-847.

(48) Green, S. P.; Jones, C.; Stasch, A. *Science* **2007**, *318*, 1754-1757.

(49) Seyferth, D. *Organometallics* **2004**, *23*, 3562-3583.

(50) Becke, A. D. *J. Chem. Phys.* **1993**, *98*, 5648-5652.

(51) Lee, C.; Yang, W.; Parr, R. D. *Phys. Rev. B* **1988**, *37*, 785-789.

(52) Stephens, P. J.; Devlin, F. J.; Chabalowski, C. F.; Frisch, M. J. *J. Phys. Chem.* **1994**, *98*, 11623-11627.

(53) Frisch, M. J.; Trucks, G. W.; Schlegel, H. B.; Scuseria, G. E.; Robb, M. A.; Cheeseman, J. R.; Montgomery, J. A., Jr.; Vreven, T.; Scalmani, G.; Mennucci, B.; Barone, V.; Petersson, G. A.; Caricato, M.; Nakatsuji, H.; Hada, M.; Ehara, M.; Toyota, K.; Fukuda, R.; Hasegawa, J.; Ishida, M.; Nakajima, T.; Honda, Y.; Kitao, O.; Nakai, H.; Li, X.; Hratchian, H. P.; Peralta, J. E.; Izmaylov, A. F.; Kudin, K. N.; Heyd, J. J.; Brothers, E.;

Staroverov, V.; Zheng, G.; Kobayashi, R.; Normand, J.; Sonnenberg, J. L.; Iyengar, S. S.; Tomasi, J.; Cossi, M.; Rega, N.; Burant, J. C.; Millam, J. M.; Klene, M.; Knox, J. E.; Cross, J. B.; Bakken, V.; Adamo, C.; Jaramillo, J.; Gomperts, R.; Stratmann, R. E.; Yazyev, O.; Austin, A. J.; Cammi, R.; Pomelli, C.; Ochterski, J. W.; Ayala, P. Y.; Morokuma, K.; Voth, G. A.; Salvador, P.; Dannenberg, J. J.; Zakrzewski, V. G.; Dapprich, S.; Daniels, A. D.; Strain, M. C.; Farkas, O.; Malick, D. K.; Rabuck, A. D.; Raghavachari, K.; Foresman, J. B.; Ortiz, J. V.; Cui, Q.; Baboul, A. G.; Clifford, S.; Cioslowski, J.; Stefanov, B. B.; Liu, G.; Liashenko, A.; Piskorz, P.; Komaromi, I.; Martin, R. L.; Fox, D. J.; Keith, T.; Al-Laham, M. A.; Peng, C. Y.; Nanayakkara, A.; Challacombe, M.; Chen, W.; Wong, M. W.; Pople, J. A.; Revision F.02 ed.; Gaussian, Inc.: Wallingford, CT, 2007.

(54) Küchle, W.; Dolg, M.; Stoll, H.; Preuss, H. *J. Chem. Phys.* **1994**, *100*, 7535-7542.

(55) Hratchian, H. P.; Sonnenberg, J. L.; Hay, P. J.; Martin, R. L.; Bursten, B. E.; Schlegel, H. B. *J. Phys. Chem. A* **2005**, *109*, 2255-2262.

(56) Sonnenberg, J. L.; Hay, P. J.; Martin, R. L.; Bursten, B. E. *Inorg. Chem.* **2005**, 2255-2262.

(57) Dunning, T. H. *J. Chem. Phys.* **1989**, *90*, 1007-1023.

(58) Seeger, R.; Pople, J. A. *J. Chem. Phys.* **1977**, *66*, 3045-3050.

(59) Glendening, E. D.; Badenhoop, J. K.; Reed, A. E.; Carpenter, J. E.; Bohmann, J. A.; Morales, C. M.; F., W.; Theoretical Chemistry Institute, University of Wisconsin: Madison, 2001.

(60) Clark, A. E.; Sonnenberg, J. L.; Hay, P. J.; Martin, R. L. *J. Chem. Phys.* **2004**, *121*, 2563-2570.

(61) Maseras, F.; Morokuma, K. *Chem. Phys. Lett.* **1992**, *195*, 500-504.

(62) Dennington II, R.; Keith, T.; Millam, J. M.; Eppinnett, K.; Hovell, W. L.; Gilliland, R.; 3.09 ed.; Semichem, Inc.: Shawnee Mission, Kansas, 2003.

(63) Baerends, E. J.; Ellis, D. E.; Ros, P. *Chem. Phys.* **1973**, *2*, 41-51.

(64) Lenthe, E. v.; Baerends, E. J.; Snijders, J. G. *J. Chem. Phys.* **1993**, *99*, 4597-4610.

(65) Lenthe, E. v.; Baerends, E. J.; Snijders, J. G. *J. Chem. Phys.* **1994**, *101*, 9783-9792.

(66) Lenthe, E. v.; Ehlers, A.; Baerends, E. J. *J. Chem. Phys.* **1999**, *110*, 8943-8953.

(67) Baerends, E. J.; Autschbach, J.; Bérces, A.; Bo, C.; Boerrigter, P. M.; Cavallo, L.; Chong, D. P.; Deng, L.; Dickson, R. M.; Ellis, D. E.; Fan, L.; Fischer, T. H.; Guerra, C. F.; Gisbergen, S. J. A. v.; Groeneveld, J. A.; Gritsenko, O. V.; Grüning, M.; Harris, F. E.; Hoek, P. v. d.; Jacobsen, H.; Kessel, G. v.; Kootstra, F.; Lenthe, E. v.; McCormack, D. A.; Osinga, V. P.; Patchkovskii, S.; Philipsen, P. H. T.; Post, D.; Pye, C. C.; Ravenek, W.; Ros, P.; Schipper, P. R. T.; Schreckenbach, G.; Snijders, J. G.; Sola, M.; Swart, M.; Swerhone, D.; Velde, G. t.; Vernooijs, P.; Versluis, L.; Visser, O.; Wezenbeek, E. v.; Wiesenekker, G.; Wolff, S. K.; Woo, T. K.; Ziegler, T.; ADF2007.01 ed.; SCM, Theoretical Chemistry, Vrije Universiteit, : Amsterdam, The Netherlands, http://www.scm.com.

(68) Streitwieser, A.; Mueller-Westerhoff, U. *J. Am. Chem. Soc.* **1968**, *90*, 7364-7364.

(69) Zalkin, A.; Raymond, K. N. *J. Am. Chem. Soc.* **1969**, *91*, 5667-5668.

(70) Avdeef, A.; Raymond, K. N.; Hodgson, K. O.; Zalkin, A. *Inorg. Chem.* **1972**, *11*, 1083-1088.

(71) Streitwieser, A.; Yoshida, N. *J. Am. Chem. Soc.* **1969**, *91*, 7528-7528.

(72) Karraker, D. G.; Stone, J. A.; Jones, E. R.; Edelstein, N. *J. Am. Chem. Soc.* **1970**, *92*, 4841-4845.

(73) Starks, D. F.; Parsons, T. C.; Streitwieser, A.; Edelstein, N. *Inorg. Chem.* **1974**, *13*, 1307-1308.

(74) Pyykkö, P.; Riedel, S.; Patzschke, M. *Chem. Eur. J.* **2005**, *11*, 3511-3520.

(75) Li, J.; Bursten, B. E. The Electronic Structure of Organoactinide Complexes via Relativistic Density Functional Theory: Applications to the Actinocene Complexes An(eta8-C8H8)2 (An=Th-Am). In *Computational Organometallic Chemistry*; Cundari, T. R., Ed.; Dekker: New York, 2001, p 345-379.

(76) Brauer, D. J.; Krüger, C. *Inorg. Chem.* **1976**, *15*, 2511-2514.

(77) Cotton, F. A.; Koch, S. A.; Schultz, A. J.; Williams, J. M. *Inorg. Chem.* **1978**, *17*, 2093-2098.

(78) Bursten, B. E.; Chisholm, M. H.; Drummond, M. L.; Gallucci, J. C.; Hollandsworth, C. B. *J. Chem. Soc., Dalton Trans.* **2002**, 4077-4083.

(79) Brett, C. M.; Bursten, B. E. *Polyhedron* **2004**, *23*, 2993-3002.

(80) Slater, J. C. *J. Chem. Phys.* **1964**, *41*, 3199-3204.

(81) Burns, C. J.; Clark, D. L.; Sattelberger, A. P. Actinides: Organometallic Chemistry. In *Encyclopedia of inorganic chemistry*; 3rd ed.; King, R. B., Ed.; Wiley: Chichester, West Sussex, England ; Hoboken, NJ, 2005.

(82) Berthet, J. C.; Thuery, P.; Ephritikhine, M. *Organometallics* **2008**, *27*, 1664-1666.

(83) Evans, W. J. *Inorg. Chem.* **2007**, *46*, 3435-3449.

CHAPTER 8

QM/MM STUDIES OF THE MATRIX METALLOPROTEINASE 2 (MMP2) INHIBITION MECHANISM OF (*S*)-SB-3CT AND ITS OXIRANE ANALOGUE

8.1 Introduction:

The matrix metalloproteinases (MMPs) are key proteolytic regulators of the integrity of the extracellular matrix. MMPs are implicated in embryonic development,[1-3] tissue remodeling and repair,[4-6] neurophathic pain processes,[7] cancer,[8-11] and other diseases.[12-15] MMP2 (Gelatinases A), one of these zinc-dependent proteolytic enzymes, digests type IV collagens.[16] The structure and function of this protein have been studied extensively for the purpose of selective inhibitor design.[17-29] One of these inhibitors, (4-phenoxyphenylsulfonyl)methylthiirane (SB-3CT), selectively inhibits MMP2 with high potency.[30,31] The inhibition mechanism of MMP2 by (*R*)-SB-3CT is coupled deprotonation of the methylene group juxtaposed between the sulfone and the thiirane, and the opening of the thiirane ring.[31,32] This reaction creates a thiolate anion which strongly coordinates with the zinc at the active site.

It is remarkable that the *R* and *S* enantiomers of SB-3CT display similar potency as inhibitors of MMP2, even though they are expected to have rather different binding modes in the active site.[33] The kinetic parameters for the *R* enantiomer are K_{on} = 2.2 ± 0.5 × 10^4 M^{-1} s^{-1}, K_{off} = 5.3 ± 0.5 × 10^{-4} s^{-1} and K_i = 24 ± 6 nM, and the corresponding values for the *S* enantiomer are K_{on} = 1.7 ± 0.4 ×

104 M^{-1} s^{-1}, K_{off} = 4.0 ± 0.3 × 10^{-4} s^{-1} and K_i = 23 ± 6 nM. Their similar potency suggests that both enantiomers have a similar inhibitory mechanism, despite this anticipated difference in their binding modes. In this study we used methods similar to our previous study of MMP2·(*R*)-SB-3CT[32] to investigate these binding modes, and to compare the inhibition mechanism of (*S*)-SB-3CT (**3**) and its oxirane analogue (**4**) (Scheme 8.1). The MMP2·(*S*)-SB-3CT complex was constructed by docking and molecular dynamics studies. The details of the deprotonation/ring opening mechanism for inhibition were examined by combined quantum mechanics and molecular mechanics (QM/MM) methods, and compared to (*R*)-SB-3CT. Vibrational frequencies, intrinsic reaction paths and kinetic isotope effects were calculated for both the *R* and *S* enantiomers of SB-3CT.

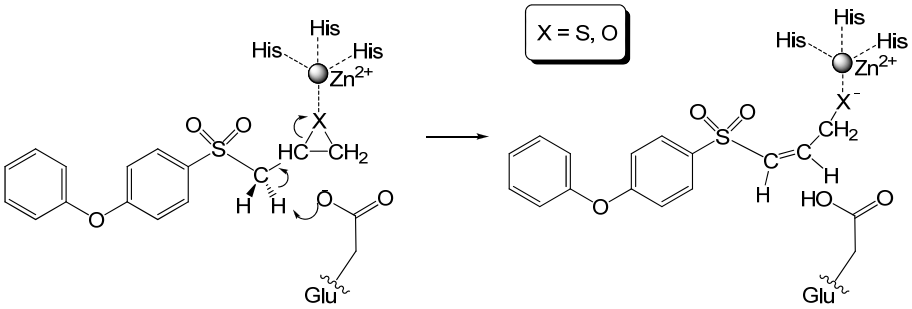

Scheme 8.1 MMP2 inhibition mechanisms by SB-3CT (**3**, X = S) and its oxirane analogue (**4**, X = O)

8.2 Computational Methods:

As in the previous study of the *R* isomer of SB-3CT, the initial structures of the MMP2 complex with (*S*)-SB-3CT and its oxirane analogue were built by docking and molecular dynamics (MD) methods.[32] A two-layer ONIOM method[34-41] was used for the QM/MM study of the inhibition mechanism of **3** and **4**. The QM region (46 atoms) consists of the zinc ion, the three imidazole rings from His403, His407 and His413, the $CH_2CO_2^-$ part of the Glu404 side chain, the thiirane and the SO_2CH_2 group of the inhibitor, and one water molecule. The B3LYP/6-31G(d) level of density functional theory (DFT) described the QM part of the system, and the AMBER force field[42] described the MM part of the system. QM/MM geometry optimization was carried out with a mechanical embedding scheme. The QM part and all residues and solvent molecules in the MM part within 6 Å of the QM part were fully optimized (936 atoms), while the remaining atoms were held fixed. Similar cut-offs have been used previously in QM/MM studies of enzymatic systems to avoid spurious changes in the energy due to remote fluctuation in the geometry.[43,44] Because the MMP2 active site is rather open to the solvent, a smaller cut-off of 6 Å was used. The partial charges for the reactive system were refined by alternating between QM/MM geometry optimization and RESP[45,46] charge fitting.[32] With mechanical embedding, the electrostatic interactions between the QM and MM regions are calculated using these partial charges. Single point calculations with electronic embedding[41] were used for the final QM/MM energies calculated at the ONIOM(B3LYP/6-311+G(d,p):AMBER) level of theory. When calculated with the

same basis set, the mean absolute difference in the relative energies with electronic embedding vs. mechanical embedding is 3 kcal/mol. All ONIOM calculations were performed with the development version of GAUSSIAN.[47] The ONIOM toolkit[48] facilitated the QM/MM calculations.

8.3 Results and Discussion

The MMP2·(R)-SB-3CT·and MMP2·(S)-SB-3CT complexes are compared in Figure 8.1. These complexes are obtained by docking, followed by MD simulation and QM/MM geometry optimization. Similar to (R)-SB-3CT in the MMP2 active site,[32] the phenoxyphenyl side chain of (S)-SB-3CT fits into the S1' pocket, and the hydrogen bond (1.83 Å) between the backbone NH of Leu191 to the pro-S oxygen of the sulfone is preserved. The second oxygen of the sulfone is exposed to solvent. In contrast to (R)-SB-3CT, the plane of the thiirane ring of (S)-SB-3CT points away from the zinc. The Zn-S distance in MMP2·(S)-SB-3CT (4.55 Å) is significantly longer than in MMP2·(R)-SB-3CT (2.91 Å). As a consequence, a water molecule coordinates with the zinc in the (S)-SB-3CT complex (Zn-O distance is 2.11 Å) but not in the (R)-SB-3CT complex (3.58 Å). The MMP2 complex of the oxirane analogue of (S)-SB-3CT is generated by replacement of the sulfur of the thiirane with oxygen. The QM part and adjacent regions were examined visually (see Figure 8.2 for a superposition of the reactants and transition states for **3** and **4**) to ensure that the reactant complex and the transition state have similar hydrogen-bonding patterns with the solvent water molecules, to avoid spurious differences in barrier heights caused by minor changes in the solvent.

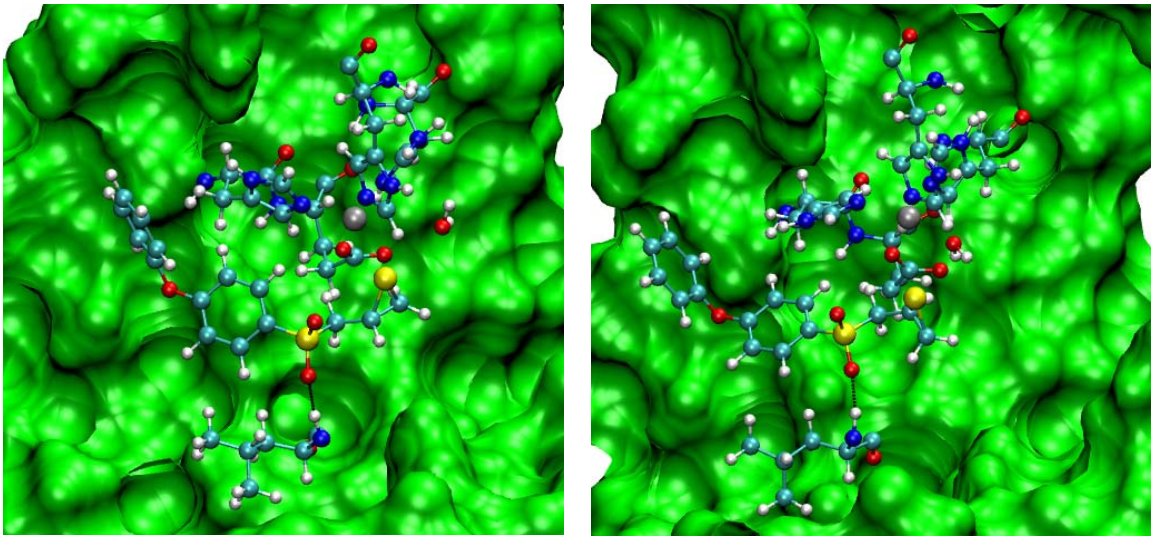

(*R*)-SB-3CT (*S*)-SB-3CT

Figure 8.1 Structures of (*R*)-SB-3CT and (*S*)-SB-3CT in the MMP2 active site optimized at the ONIOM(B3LYP/6-31G(d):AMBER) level of theory. Residues of MMP2·(*R*)-SB-3CT and MMP2·(*S*)-SB-3CT are shown in ball-and-stick representation with atom colored according to atom types (H, C, N, O, S, Zn, shown in white, cyan, blue, red, yellow, and grey, respectively). The same color scheme is used in all the figures.

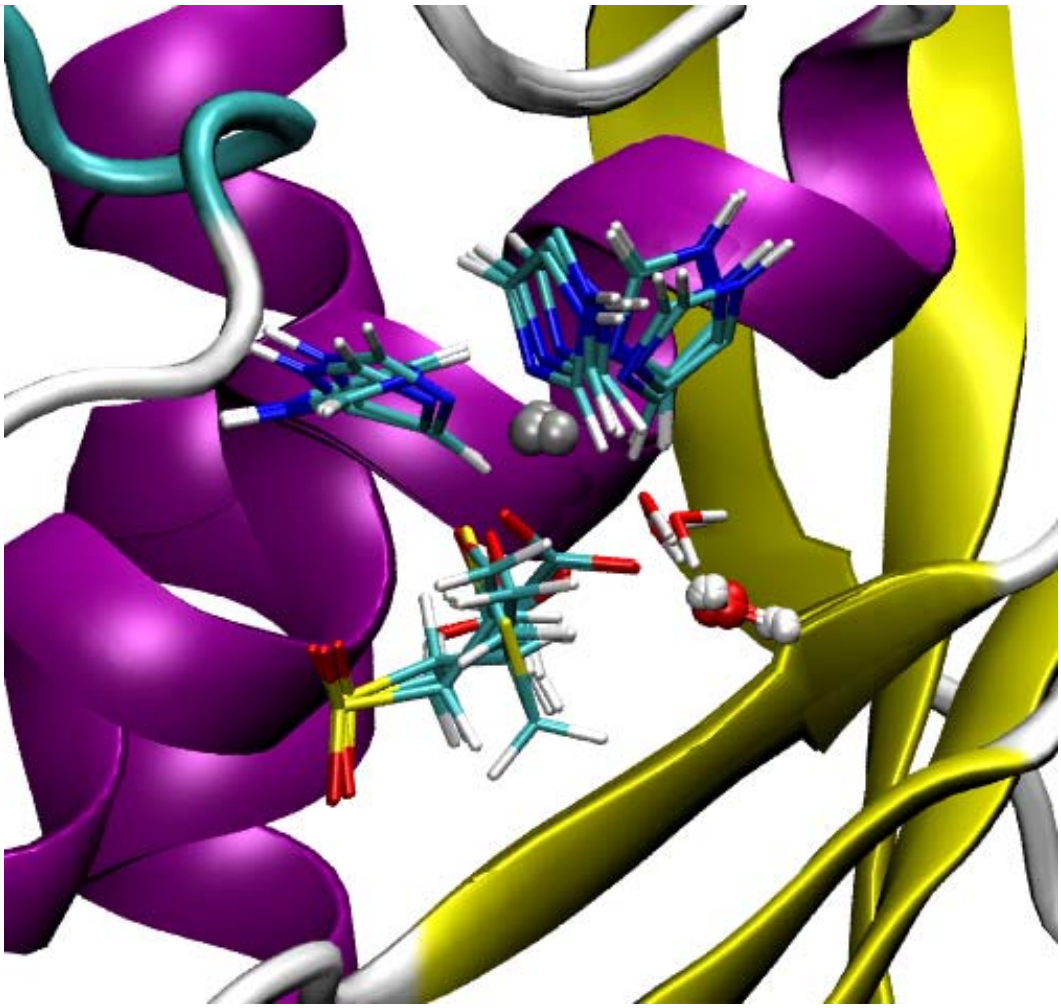

Figure 8.2 The comparison of the MM water (in ball-and-stick representation) that is close to QM region (in cylinder representation) in **3-R**, **3-TS**, **4-R**, and **4-TS**

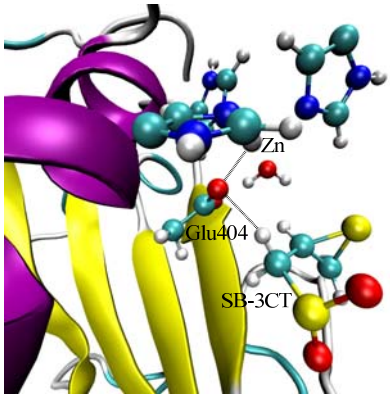

3-R 0.0

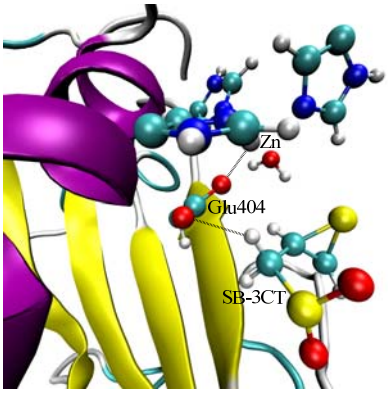

3-R' 2.6

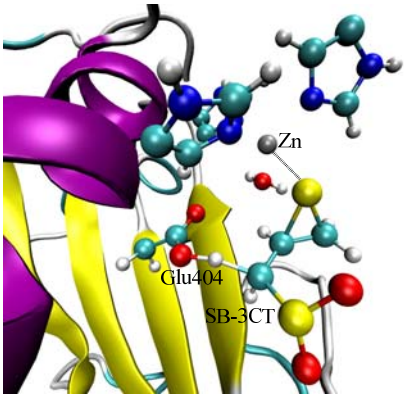

3-TS 16.1

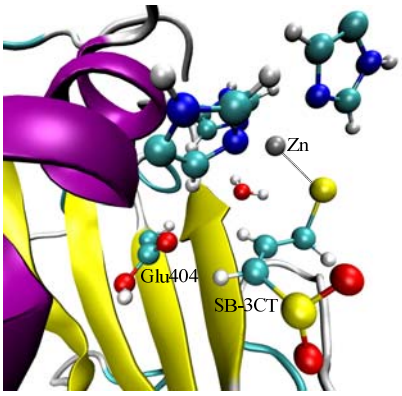

3-P1 -13.2

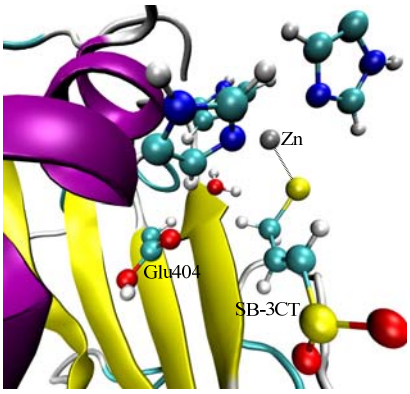

3-P1' -20.2

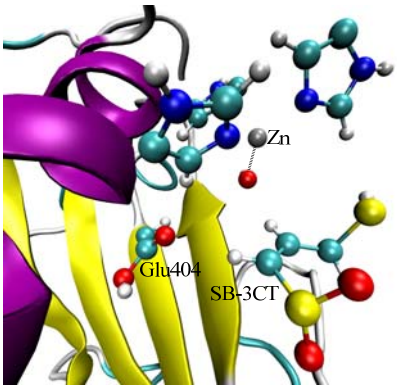

3-P2 8.7

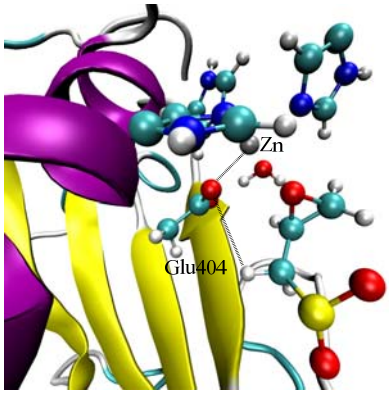

4-R 0.0

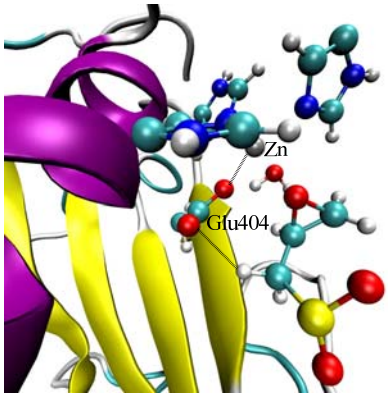

4-R' 3.9

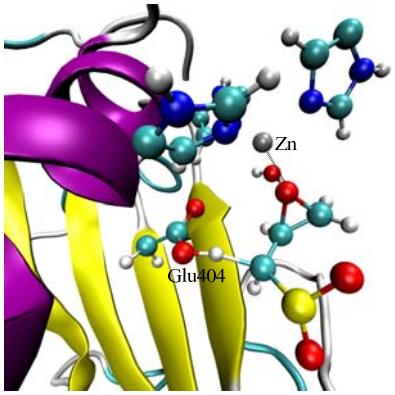

4-TS 20.5

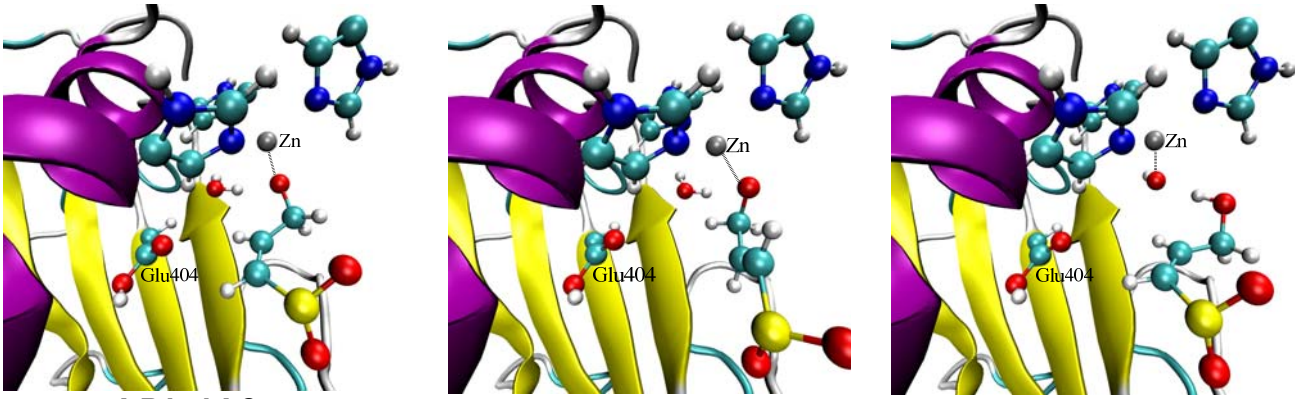

4-P1 -14.9 **4-P1' -20.3** **4-P2 -11.2**

Figure 8.3 Reactants, transition states and products for (*S*)-SB-3CT (**3**) and its oxirane analogue (**4**) in the MMP2 active site optimized at the ONIOM(B3LYP/6-31G(d):AMBER) level of theory. Energies (in kcal/mol) were calculated at the ONIOM(B3LYP/6-311+G(d,p):AMBER) using electronic embedding with the reactant complexes used as the reference states. **3-P1** and **4-P1** are the *cis* isomers of the unprotonated ring opening products. **3-P1'** and **4-P1'** are the *trans* isomers. In **3-P2** and **4-P2**, the *cis* ring opening products are protonated by the water molecule, and the resulting hydroxide anion coordinates with the zinc.

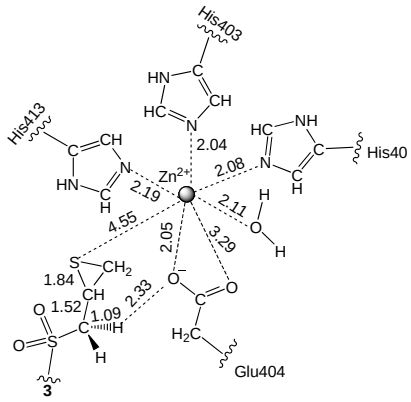

3-R 0.0

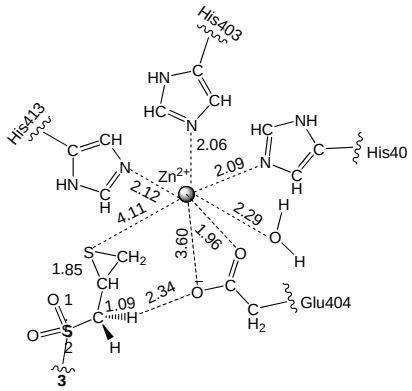

3-R’ 2.6

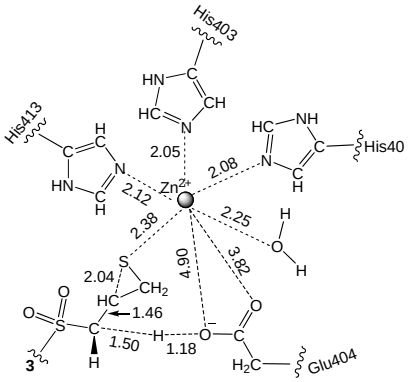

3-TS 16.1

!! EMBED

ChemDraw.Document.6.0

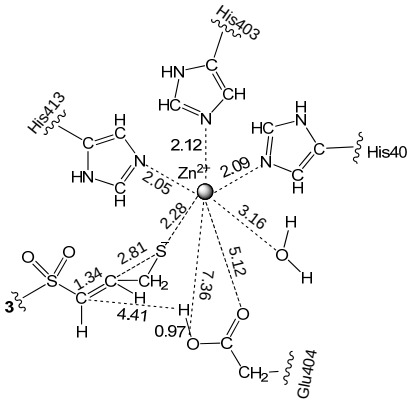

3-P1 -13.2

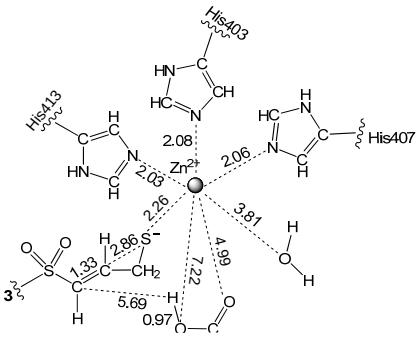

3-P2 -20.2

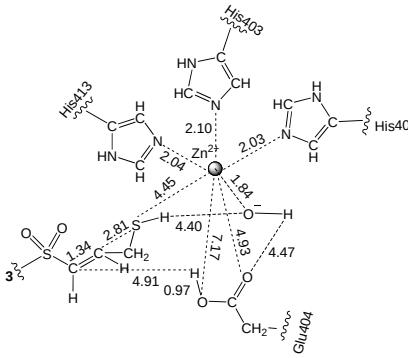

3-P3 8.7

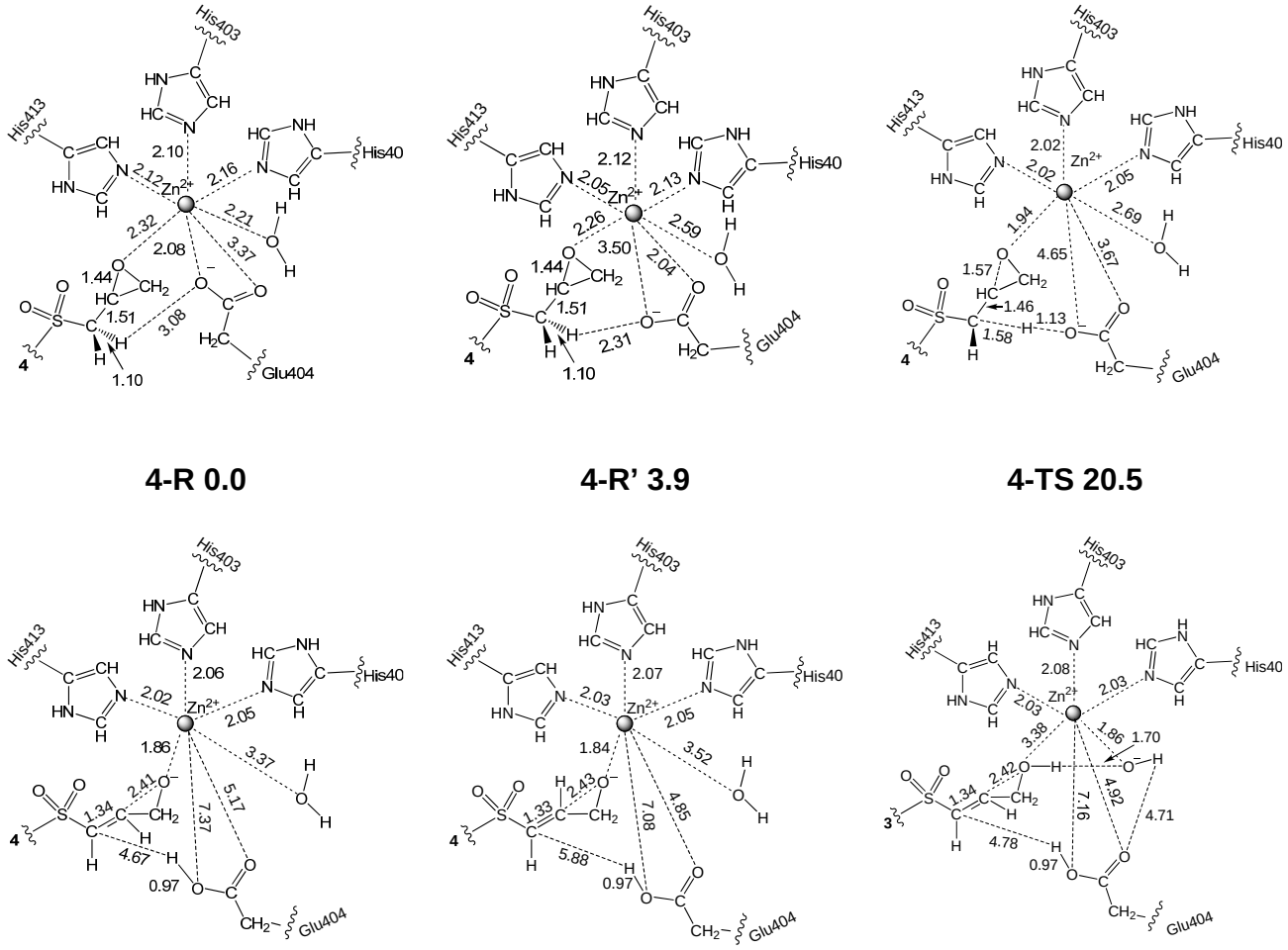

Figure 8.4 Reactants, transition states and products for (*S*)-SB-3CT (**3**) and its oxirane analogue (**4**) in the MMP2 active site optimized at the ONIOM(B3LYP/6-31G(d):AMBER) level of theory. Energies (in kcal/mol) were calculated at the ONIOM(B3LYP/6-311+G(d,p):AMBER) using electronic embedding with the reactant complexes used as reference states. Key bond lengths are in Angstroms. Ball-and-stick representation of QM region and cartoon representation of protein are shown in Figure 8.3.

(a) Deprotonation and Ring Opening of the Inhibitor

The reactant, transition state (TS), and product structures for the inhibition of MMP2 by (*S*)-SB-3CT are shown in the top two rows of Figure 8.3 and selected geometrical parameters are given in Figure 8.4. The respective structures for the oxirane analogue are shown at the bottom of these Figures. In both reactant structures, the zinc at the MMP2 active site is coordinated with Glu404, three histidines, and one water molecule. Depending on how the Glu404 coordinates with the zinc, two local minima are identified for the reactant complex of (*S*)-SB-3CT· MMP2 and of its oxirane analogue (**3-R** and **3-R'**; **4-R** and **4-R'** in Figure 8.3). In **3-R**, the oxygen of the Glu404 that will accept the transferring proton of (*S*)-SB-3CT is coordinated (2.05 Å) to the zinc, while the other Glu404 oxygen is not (3.29 Å). For **3-R'**, the $-CO_2^-$ group of Glu404 is shifted so that the acceptor oxygen is farther from the zinc (3.60 Å) and the other oxygen is coordinated to the zinc (1.96 Å). **3-R'** is only 2.6 kcal/mol higher in energy than **3-R**. Likewise, the oxirane analogue **4-R'** is 3.9 kcal/mol higher than **4-R**. In both **3-R** and **3-R'**, the sulfur of the thiirane is significantly further from the zinc (by 4.55 and 4.11 Å, respectively) than the distance between the oxygen of oxirane and the zinc in **4-R** and **4-R'** (2.32 and 2.26 Å, respectively). The energy of MMP2·(*S*)-SB-3CT increases by 4.9 kcal/mol if the sulfur is constrained to be closer to the zinc, similar to the distance in MMP2·(*R*)-SB-3CT (2.86 Å).

In the TS identified in the QM/MM calculations, **3-TS** (Figure 8.3 and Figure 8.4), the transferring proton is 1.50 Å from the donor carbon and 1.18 Å from the acceptor oxygen, indicating the TS is a little earlier compared to

MMP2·(*R*)-SB-3CT (C–H and H–O distances of 1.57 Å and 1.14 Å, respectively). The breaking C–S bond of the thiirane is elongated to 2.04 Å in **3-TS**. The Glu404 side chain moves away from the zinc in order to abstract the proton. The TS of the oxirane analogue (**4-TS**) is similar to the thiirane system (C–H and H–O distances are 1.58 Å and 1.13 Å), but a little later than the (*R*)-oxirane TS (C–H and H–O distances are 1.43 Å and 1.24 Å). In the transition states, the thiirane sulfur and oxirane oxygen are strongly coordinated to the zinc (Zn–S and Zn–O distances are 2.38 Å and 1.94 Å, respectively), but the glutamate is not.

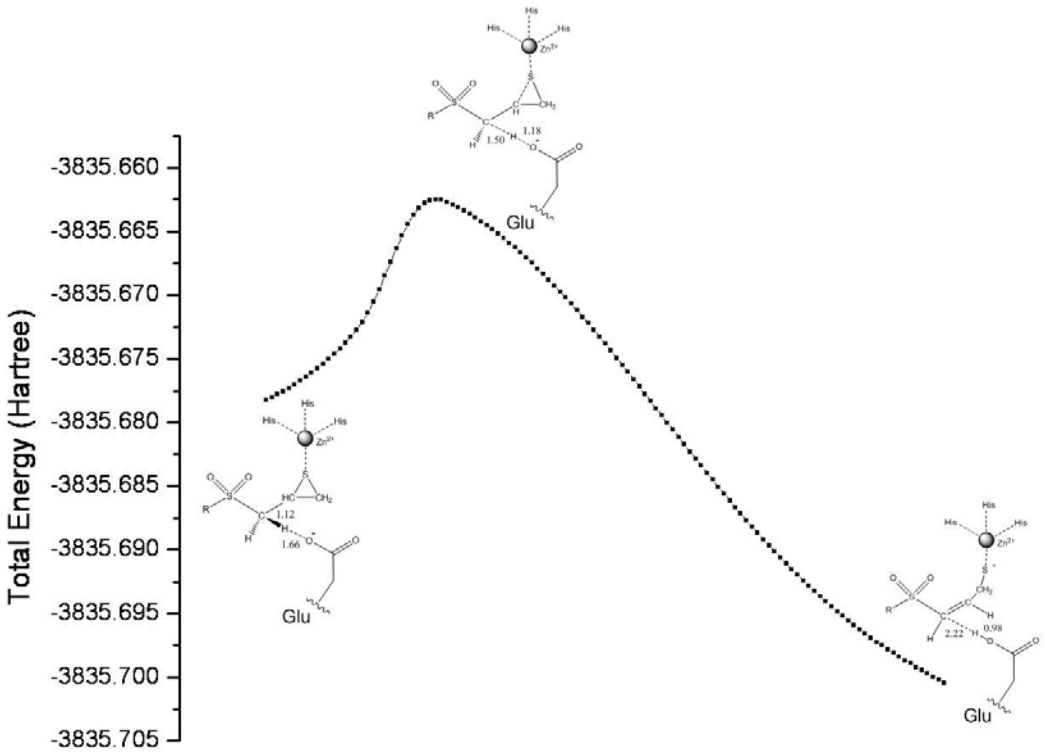
Total Energy (Hartree)
-3835.660
-3835.665
-3835.670
-3835.675
-3835.680
-3835.685
-3835.690
-3835.695
-3835.700
-3835.705
His
His
His
Zn2+
Glu
1.18
1.50
1.12
1.66
2.22
0.98

(a)

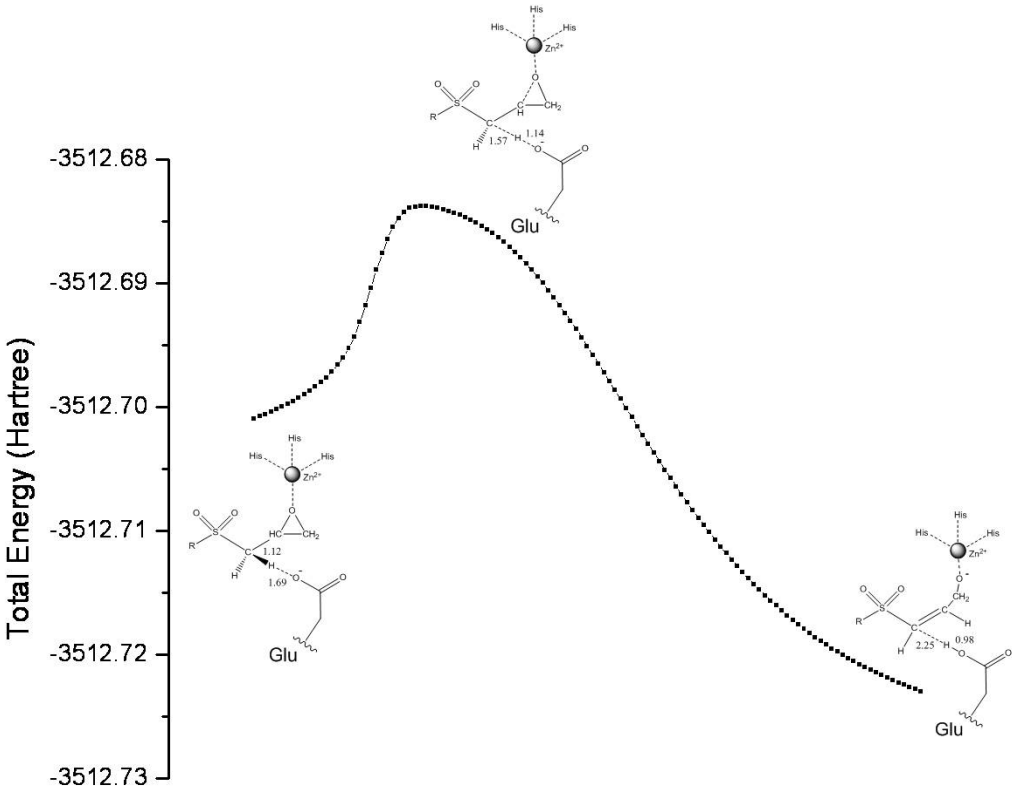

(b)

Figure 8.5 IRC profiles for (*S*)-SB-3CT (**a**) and its oxirane analogue (**b**) in the MMP2 active site using the partial model at the ONIOM(B3LYP/6-31G(d):AMBER) level of theory. Key bond lengths are in Angstroms.

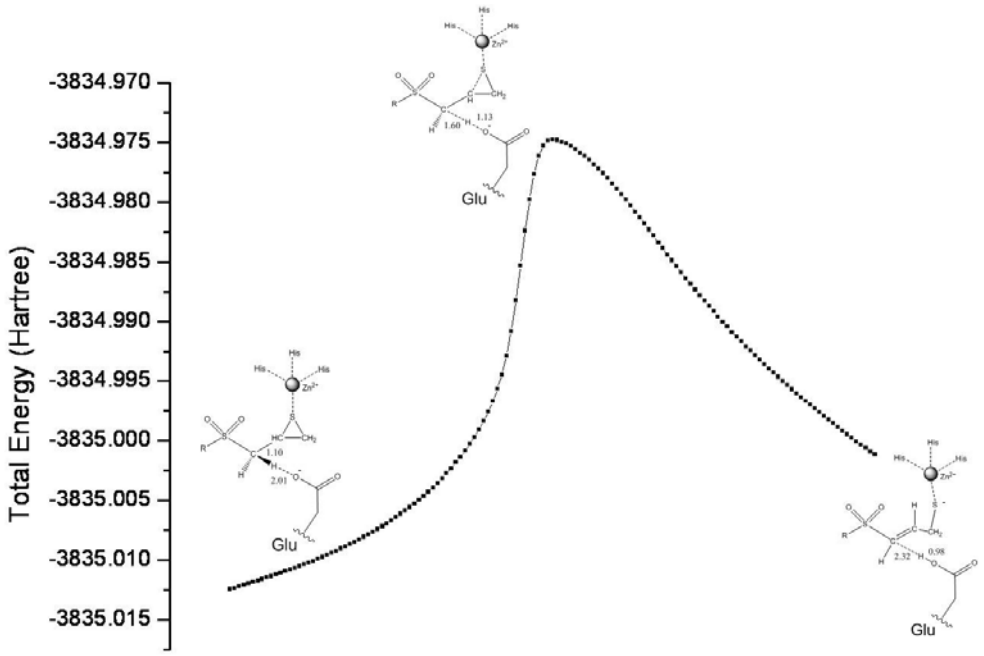
Total Energy (Hartree)
-3834.970
-3834.975
-3834.980
-3834.985
-3834.990
-3834.995
-3835.000
-3835.005
-3835.010
-3835.015
Glu
Glu
Glu

(a)

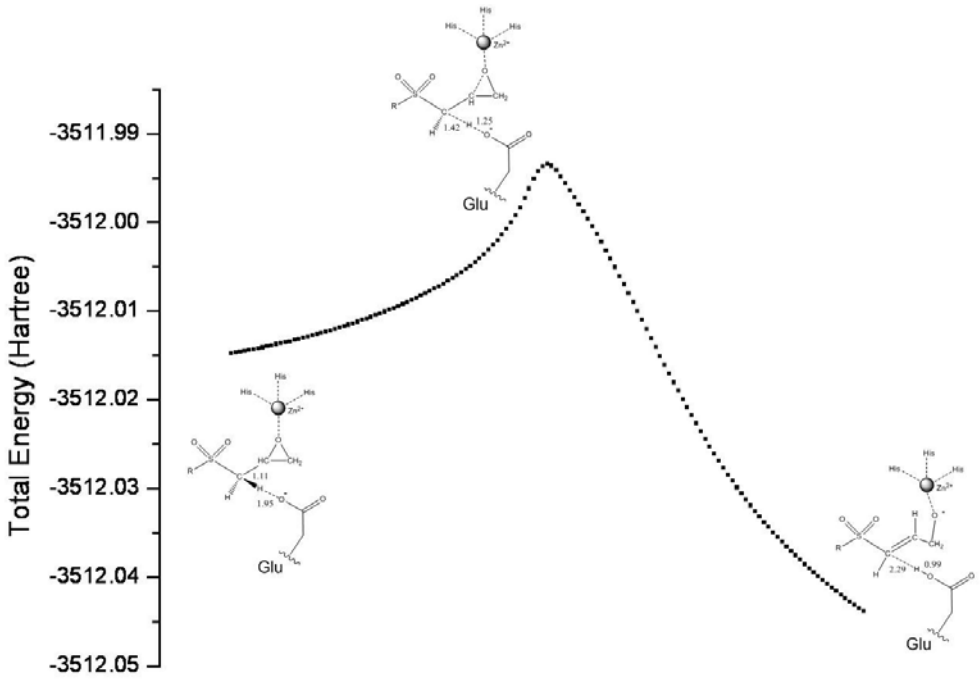

(b)

Figure 8.6 IRC profiles for (*R*)-SB-3CT (**a**) and its oxirane analogue (**b**) in the MMP2 active site using the partial model at the ONIOM(B3LYP/6-31G(d):AMBER) level of theory. Key bond lengths are in Angstroms.

(b) Vibrational Frequencies and Reaction Path Following

While the full frequency calculations at the current level of theory are not feasible for the whole system (9208 atoms), the two lowest vibrational modes can be calculated. Only one imaginary frequency is found for **3-TS** and **4-TS** (1018*i* and 540*i* cm^{-1}, respectively), verifying that these structures are transition states. Two reduced size (partial) models were built from the full thiirane and oxirane TS complexes by extracting all the QM atoms (46 atoms), the MM atoms which are allowed to move during geometry optimization (936 atoms) and enough frozen MM atoms to surround the first two parts, for a total of 2747 atoms. When the transition states of the reduced systems were re-optimized, the key parameters changed very little (RMSD = 0.04 Å, C-H and O-H distances involving the transferring proton changed by less than 0.01 Å). The fact that these changes are quite small suggests that the reduced systems are good models of the full protein-inhibitor complexes. Using the optimized transition states of these reduced size models, the full frequency analysis and calculation of the intrinsic reaction coordinate (IRC) are both practical with the latest version of the code.[49] The frequency analysis for the partial models of the TSs gives imaginary frequencies close to the full system for both the thiirane (1031*i* cm^{-1}) and oxirane (601*i* cm^{-1}). As a part of the present work, similar calculations were carried out for the TS structure for the inhibition of MMP2 by (*R*)-SB-3CT.[32] The imaginary frequencies are 767*i* and 642*i* for the full and reduced size thiirane systems, respectively. For its oxirane analogue, the imaginary frequencies are 1217*i* and 1234*i* for the full and reduced size systems, respectively.

The intrinsic reaction coordinate (IRC) was calculated using the reduced size model to generate the reaction path from the reactants to the products through the TSs. The profiles of the IRC paths, and the key structures, are shown in Figure 8.5 (see Figure 8.6 for *R* enantiomer). The reaction path calculations clearly demonstrate that there are no additional barriers between the TSs and the reactants, and TSs and the products, for both MMP2·(*S*)-SB-3CT and its oxirane analogue. The reaction path shows that the *R* enantiomer of SB-3CT and its oxirane analogue open to the *trans* products. The corresponding reaction paths for the *S* enantiomer of the thiirane and oxirane lead to the *cis* products, **3-P1** and **4-P1.** The *cis* products are 6.9 and 5.4 kcal/mol higherthan the *trans* products, **3-P1'** and **4-P1**', part because of less favorable interactions with the active site. The different stereochemical outcome for the two enantiomers demonstrates that stereoelectronic control exists in the transition state. Animations of the normal mode corresponding to the imaginary frequencies and the IRC paths for MMP2·(*S*)-SB-3CT and its oxirane analogue are provided on the ACS website.

Table 8.1 QM/MM calculations of the energetics for the ring-opening reactions of inhibitions in the active site of MMP2[a]

Inhibitor	Barrier Height	Reaction Enthalpy		
		P1 (unprotonated *cis* product)	**P1'** (unprotonated *trans* product)	**P2** (protonated *cis* product)
(*S*)-SB-3CT (**3**)[b]	16.1	–13.3	–20.2	8.7
(*S*)-Oxirane Analogue (**4**)[b]	20.5	–14.9	–20.3	–11.2

[a] ONIOM(B3LYP/6-311+G(d,p):AMBER)//ONIOM(B3LYP/6-31G(d):AMBER) with electronic embedding; energies in kcal/mol.

[b] See Figure 8.3.

(c) Thermodynamics

The energy profiles for (*S*)-SB-3CT (**3**) and its oxirane analogue (**4**) in the MMP2 active site are shown in Figure 8.7 and summarized in Table 8.1. The ring opening barriers for the *S*-thiirane and *S*-oxirane in the active site of MMP2 are 16.1 and 20.5 kcal/mol, respectively. The thiolate ring-opened product from the thiirane (**3-P1**), and the alkoxide ring-opened product from the oxirane (**4-P1**), both show tight coordination with the zinc in these product complexes. The protonated Glu404 moves significantly away from the zinc. The water molecule in both **3-P1** and **4-P1** moves away from the zinc to distances of 3.16 Å and 3.37 Å, respectively. The reaction energies for thiirane and oxirane are –13.3 and –14.9 kcal/mol, respectively.

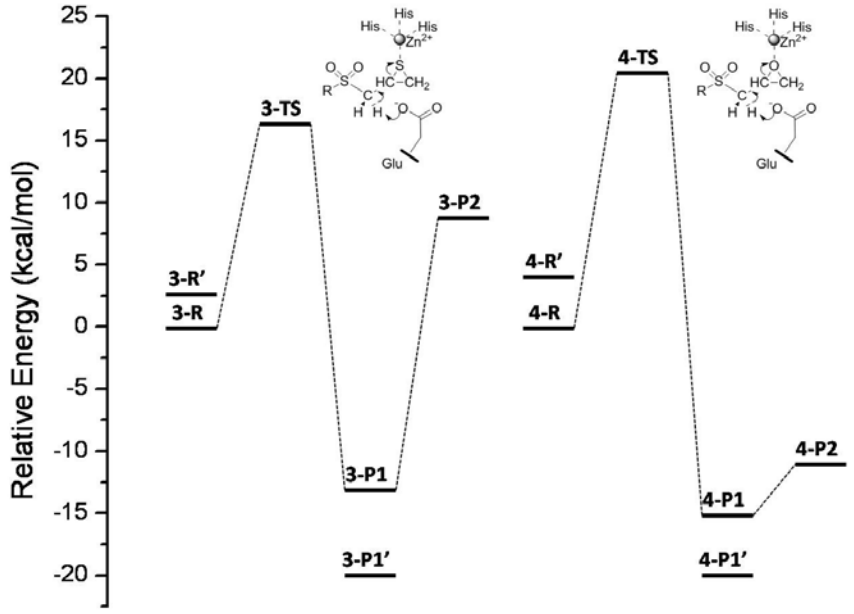

Figure 8.7 Energy profiles for (*S*)-SB-3CT (**3**) and its oxirane analogue (**4**) in the MMP2 active site. Relative energies (in kcal/mol) were calculated at the ONIOM(B3LYP/6-311+G(d,p):AMBER) using electronic embedding with the reactant complexes used as reference states.

(d) Product Protonation by Water

Since solvent has substantial access to the active site of MMP2, the ring-opened products can be protonated by solvent. Proton transfer from a nearby water to **3-P1** and **4-P1** gives structures **3-P2** and **4-P2**, respectively (Figure 8.3 and Figure 8.4). Proton transfer from the water molecule generates a hydroxide ion which coordinates with the zinc, replacing the thiolate and alkoxide as zinc ligands. For the thiirane system, the protonated product complex **3-P2** is 8.7 kcal/mol endothermic compared to the reactant complex **3-R**. For the oxirane system, by contrast, the protonated product complex **4-P2** is 11.2 kcal/mol exothermic compared to the reactant complex **4-R**. A similar result was observed in the study of the *R* enantiomer.[32] This difference between the thiirane and oxirane may explain why both the *R* and *S* enantiomers of SB-3CT are slow binding inhibitors of MMP2, while their oxirane analogues are linear competitive inhibitors.[30]

(e) Kinetic Isotope Effect (KIE) Calculations using the QM/MM model

In our earlier studies, the KIE calculation for the *R*-thiirane could only be carried out for the solution model.[32] However, recent improvements in computer code and resources have made it feasible to calculate the full set of frequencies for QM/MM systems. Using the frequency calculations for the 2747 atom QM/MM models, deuterium KIEs were calculated for both the MMP2·(*R*)-SB-3CT and MMP2·(*S*)-SB-3CT complexes. The Wigner tunneling correction[50] contributes a factor of 1.15 for *R*-thiirane and 1.27 for *S*-thiirane. The calculated KIE (k_H/k_D) is 5.9 for the inhibition of MMP2 by (*R*)-SB-3CT, and 6.7 for (*S*)-SB-3CT. These

numbers agree well with the experimental result for the racemic mixture (k_H/k_D = 5.0).[31]

8.4 Conclusions:

The inhibition of MMP2 by (*S*)-SB-3CT (**3**) and its oxirane analogue (**4**) involves the concurrent deprotonation of the inhibitor by the active-site glutamate, opening of the respective three-membered heterocycle, and coordination of the heteroatom anion product to the active-site zinc. For the present QM/MM calculations, the barrier for this ring-opening reaction of (*S*)-SB-3CT in the MMP2 active site is 16.1 kcal/mol, and is 4.4 kcal/mol lower than the barrier for the oxirane analogue. Abstraction of a proton from the inhibitor by glutamate is the key event in the inhibition reaction, as indicated by the kinetic isotope effects, and is directly coupled with the ring-opening. In the transition state, the heteroatom of the three-membered ring moves closer to the zinc, facilitating completion of the deprotonation and ring opening events for progress toward the product complexes. The reaction enthalpies are quite similar (–13.3 kcal/mol for **3** and –14.9 kcal/mol for **4**). Reaction path following calculations show that ring opening of (*S*)-SB-3CT by MMP2 yields the *cis* product, while ring opening of (*R*)-SB-3CT in the MMP2 produces the *trans* product. The calculations show that the protonation of the alkoxide product from the ring opening of **4** by a water molecule in the active site is exothermic, whereas protonation of the thiolate from ring opening of **3** is endothermic. The calculated KIEs of the reaction agree well with the experimental results, increasing the confidence in the present study. The

previous and present studies provide the solid theoretical support for the inhibition mechanism of MMP2.

8.5 References

(1) Lei, H.; Furth, E. E.; Kalluri, R.; Wakenell, P.; Kallen, C. B.; Jeffrey, J. J.; Leboy, P. S.; Strauss, J. F., 3rd *Biol. Reprod.* **1999**, *60*, 183-189.

(2) Liu, C.-H.; Wu, P.-S. *Biotechnol. Lett.* **2006**, *28*, 1725-1730.

(3) Shi, Y.-B.; Fu, L.; Hasebe, T.; Ishizuya-Oka, A. *Pharmacol. Ther.* **2007**, *116*, 391-400.

(4) Woessner, J. F., Jr. *FASEB J.* **1991**, *5*, 2145-2154.

(5) Smith, M. F.; Ricke, W. A.; Bakke, L. J.; Dow, M. P.; Smith, G. W. *Mol. Cell. Endocrinol.* **2002**, *191*, 45-56.

(6) Homandberg, G. A.; Ummadi, V.; Kang, H. *Inflammation Res.* **2004**, *53*, 534-543.

(7) Kawasaki, Y.; Xu, Z.-Z.; Wang, X.; Park, J. Y.; Zhuang, Z.-Y.; Tan, P.-H.; Gao, Y.-J.; Roy, K.; Corfas, G.; Lo, E. H.; Ji, R.-R. *Nat. Med.* **2008**, *14*, 331-336.

(8) Coussens, L. M.; Werb, Z. *Chem. Biol.* **1996**, *3*, 895-904.

(9) Vihinen, P.; Kähäri, V. M. *Int. J. Cancer* **2002**, *99*, 157-166.

(10) Egeblad, M.; Werb, Z. *Nat. Rev. Cancer* **2002**, *2*, 161-174.

(11) Noël, A.; Jost, M.; Maquoi, E. *Semin. Cell Dev. Biol.* **2008**, *19*, 52-60.

(12) Dollery, C. M.; McEwan, J. R.; Henney, A. M. *Circ. Res.* **1995**, *77*, 863-868.

(13) Luft, F. C. *J. Mol. Med.* **2004**, *82*, 781-783.

(14) Janssens, S.; Lijnen, H. R. *Cardiovasc. Res.* **2006**, *69*, 585-594.

(15) Chow, A. K.; Cena, J.; Schulz, R. *Br. J. Pharmacol.* **2007**, *152*, 189-205.

(16) Liotta, L. A.; Tryggvason, K.; Garbisa, S.; Robey, P. G.; Abe, S. *Biochemistry* **1981**, *20*, 100-104.

(17) Morgunova, E.; Tuuttila, A.; Bergmann, U.; Isupov, M.; Lindqvist, Y.; Schneider, G.; Tryggvason, K. *Science* **1999**, *284*, 1667-1670.

(18) Briknarova, K.; Gehrmann, M.; Banyai, L.; Tordai, H.; Patthy, L.; Llinas, M. *J. Biol. Chem.* **2001**, *276*, 27613-27621.

(19) Feng, Y.; Likos, J. J.; Zhu, L.; Woodward, H.; Munie, G.; McDonald, J. J.; Stevens, A. M.; Howard, C. P.; De Crescenzo, G. A.; Welsch, D.; Shieh, H.-S.; Stallings, W. C. *Biochim. Biophys. Acta, Proteins Proteomics* **2002**, *1598*, 10-23.

(20) Lukacova, V.; Zhang, Y.; Mackov, M.; Baricic, P.; Raha, S.; Calvo, J.; Balaz, S. *J. Biol. Chem.* **2004**, *279*, 14194-14200.

(21) Diaz, N.; Suarez, D.; Sordo, T. *J. Phys. Chem. B* **2006**, *110*, 24222-24230.

(22) Tochowicz, A.; Maskos, K.; Huber, R.; Oltenfreiter, R.; Dive, V.; Yiotakis, A.; Zanda, M.; Bode, W.; Goettig, P. *J. Mol. Biol.* **2007**, *371*, 989-1006.

(23) Diaz, N.; Suarez, D. *Proteins: Struct., Funct., Bioinf.* **2008**, *72*, 50-61.

(24) Ikejiri, M.; Bernardo, M. M.; Bonfil, R. D.; Toth, M.; Chang, M.; Fridman, R.; Mobashery, S. *J. Biol. Chem.* **2005**, *280*, 33992-34002.

(25) Fisher, J. F.; Mobashery, S. *Cancer Metastasis Rev.* **2006**, *25*, 115-136.

(26) Khandelwal, A.; Balaz, S. *J. Comput.-Aided Mol. Des.* **2007**, *21*, 131-137.

(27) Khandelwal, A.; Balaz, S. *Proteins: Struct., Funct., Bioinf.* **2007**, *69*, 326-339.

(28) Gupta, S. P. *Chem. Rev.* **2007**, *107*, 3042-3087.

(29) Zhang, Y.; Lukacova, V.; Bartus, V.; Nie, X.; Sun, G.; Manivannan, E.; Ghorpade, S.; Jin, X.; Manyem, S.; Sibi, M.; Cook, G.; Balaz, S. *Chem. Biol. Drug. Des.* **2008**, *72*, 237-248.

(30) Brown, S.; Bernardo, M. M.; Li, Z.-H.; Kotra, L. P.; Tanaka, Y.; Fridman, R.; Mobashery, S. *J. Am. Chem. Soc.* **2000**, *122*, 6799-6800.

(31) Forbes, C.; Shi, Q. C.; Fisher, J. F.; Lee, M.; Hesek, D.; Llarrull, L. I.; Toth, M.; Gossing, M.; Fridman, R.; Mobashery, S. *Chem. Biol. Drug. Des.* **2009**, *74*, 527-534.

(32) Tao, P.; Fisher, J. F.; Shi, Q. C.; Vroven, T.; Mobashery, S.; Schlegel, H. B. *Biochemistry* **2009**, *48*, 9839-9847.

(33) Lee, M.; Bernardo, M. M.; Meroueh, S. O.; Brown, S.; Fridman, R.; Mobashery, S. *Org. Lett.* **2005**, *7*, 4463-4465.

(34) Maseras, F.; Morokuma, K. *J. Comput. Chem.* **1995**, *16*, 1170-1179.

(35) Svensson, M.; Humbel, S.; Froese, R. D. J.; Matsubara, T.; Sieber, S.; Morokuma, K. *J. Phys. Chem.* **1996**, *100*, 19357-19363.

(36) Humbel, S.; Sieber, S.; Morokuma, K. *J. Chem. Phys.* **1996**, *105*, 1959-1967.

(37) Dapprich, S.; Komaromi, I.; Byun, K. S.; Morokuma, K.; Frisch, M. J. *J. Mol. Struc. -THEOCHEM* **1999**, *461-462*, 1-21.

(38) Vreven, T.; Morokuma, K. *J. Comput. Chem.* **2000**, *21*, 1419-1432.

(39) Vreven, T.; Morokuma, K.; Farkas, O.; Schlegel, H. B.; Frisch, M. J. *J. Comput. Chem.* **2003**, *24*, 760-769.

(40) Vreven, T.; Frisch, M. J.; Kudin, K. N.; Schlegel, H. B.; Morokuma, K. *Mol. Phys.* **2006**, *104*, 701-714.

(41) Vreven, T.; Byun, K. S.; Komaromi, I.; Dapprich, S.; Montgomery, J. A., Jr.; Morokuma, K.; Frisch, M. J. *J. Chem. Theory Comput.* **2006**, *2*, 815-826.

(42) Cornell, W. D.; Cieplak, P.; Bayly, C. I.; Gould, I. R.; Merz, K. M.; Ferguson, D. M.; Spellmeyer, D. C.; Fox, T.; Caldwell, J. W.; Kollman, P. A. *J. Am. Chem. Soc.* **1995**, *117*, 5179-5197.

(43) Lundberg, M.; Kawatsu, T.; Vreven, T.; Frisch, M. J.; Morokuma, K. *J. Chem. Theory Comput.* **2009**, *5*, 222-234.

(44) Meroueh, S. O.; Fisher, J. F.; Schlegel, H. B.; Mobashery, S. *J. Am. Chem. Soc.* **2005**, *127*, 15397-15407.

(45) Bayly, C. I.; Cieplak, P.; Cornell, W.; Kollman, P. A. *J. Phys. Chem.* **1993**, *97*, 10269-10280.

(46) Cornell, W. D.; Cieplak, P.; Bayly, C. I.; Kollmann, P. A. *J. Am. Chem. Soc.* **1993**, *115*, 9620-9631.

(47) Frisch, M. J.; Trucks, G. W.; Schlegel, H. B.; Scuseria, G. E.; Robb, M. A.; Cheeseman, J. R.; Montgomery, J. A., Jr.; Vreven, T.; Scalmani, G.; Mennucci, B.; Barone, V.; Petersson, G. A.; Caricato, M.; Nakatsuji, H.; Hada, M.; Ehara, M.; Toyota, K.; Fukuda, R.; Hasegawa, J.; Ishida, M.; Nakajima, T.; Honda, Y.; Kitao, O.; Nakai, H.; Li, X.; Hratchian, H. P.; Peralta, J. E.; Izmaylov, A. F.; Kudin, K. N.; Heyd, J. J.; Brothers, E.; Staroverov, V.; Zheng, G.; Kobayashi, R.; Normand, J.; Sonnenberg, J. L.;

Iyengar, S. S.; Tomasi, J.; Cossi, M.; Rega, N.; Burant, J. C.; Millam, J. M.; Klene, M.; Knox, J. E.; Cross, J. B.; Bakken, V.; Adamo, C.; Jaramillo, J.; Gomperts, R.; Stratmann, R. E.; Yazyev, O.; Austin, A. J.; Cammi, R.; Pomelli, C.; Ochterski, J. W.; Ayala, P. Y.; Morokuma, K.; Voth, G. A.; Salvador, P.; Dannenberg, J. J.; Zakrzewski, V. G.; Dapprich, S.; Daniels, A. D.; Strain, M. C.; Farkas, O.; Malick, D. K.; Rabuck, A. D.; Raghavachari, K.; Foresman, J. B.; Ortiz, J. V.; Cui, Q.; Baboul, A. G.; Clifford, S.; Cioslowski, J.; Stefanov, B. B.; Liu, G.; Liashenko, A.; Piskorz, P.; Komaromi, I.; Martin, R. L.; Fox, D. J.; Keith, T.; Al-Laham, M. A.; Peng, C. Y.; Nanayakkara, A.; Challacombe, M.; Chen, W.; Wong, M. W.; Pople, J. A.; Revision F.02 ed.; Gaussian, Inc.: Wallingford, CT, 2007.

(48) Tao, P.; Schlegel, H. B. *J. Comput. Chem.* **2010**, *31*, 2363-2369.

(49) Tao, P.; Fisher, J. F.; Shi, Q.; Mobashery, S.; Schlegel, H. B. *J. Phys. Chem. B* **2010**, *114*, 1030-1037.

(50) Wigner, E. *Z. Physik. Chem.* **1932**, *B19*, 203-216.

ABSTRACT

APPLICATIONS OF ELECTRONIC STRUCTURE THEORY TO PROBLEMS IN UNIMOLECULAR DISSOCIATION AND INORGANIC AND BIOCHEMICAL SYSTEMS

by

JIA ZHOU

May 2011

Advisor: Dr. H. Bernhard Schlegel

Major: Chemistry (Physical)

Degree: Doctor of Philosophy

In this dissertation, *ab initio* classical trajectory calculations have been carried out to study the dissociation of acetone radical cation, pentane-2,4-dione radical cation, and 1,3-cyclobutanedione radical cation. For acetone radical cation and pentane-2,4-dione radical cation, MP2 with bond additivity corrections generates a better potential energy surface at low cost and is thus used for molecular dynamics calculations. The dissociation of acetone radical cation is found to favor the loss of the newly formed methyl group in agreement with the experiments. The branching ratios of methyl loss were also calculated with different amount of excess energy and of specific mode excitation. Dissociation of pentane-2,4-dione radical cation and 1,3-cyclobutanedione radical cation has not been investigated experimentally, and the present trajectory calculations provide the first theoretical description of the dissociation dynamics.

The dissociations of the methanimine neutral, monocation and dication have been studied by *ab initio* classical trajectory calculations. Many of the trajectories dissociate directly to produce H^+, H atom or H_2. However, for a fraction of the cases, substantial migration of the hydrogen occurs within the molecule before dissociation. The preferred dissociation product for the neutral and the monocation is hydrogen atom. Dissociations of the dication and trication produced H^+ rather than H atom.

The gas phase reaction of Th^+ with H_2O to produce $HThO^+$ + H and ThO^+ + H_2 has been investigated using density functional theory and coupled cluster methods. *Ab initio* classical trajectory calculations have been carried out to obtain a better model of the molecular dynamics. The molecular dynamics simulations yield a branching ratio of ca 80% for the H_2 elimination channel to 20% for the H atomic elimination channel in qualitative agreement with the observed ratio of 65% to 35%.

Complexes of the form $An_2(C_8H_8)_2$ (An = Th, Pa, U and Np) have been studied using density functional theory with scalar-relativistic effective core potentials. For uranium, a coaxial isomer with D_{8h} symmetry is found to be more stable than a C_s isomer in which the dimetal unit is perpendicular to the C_8 ring axis. Similar coaxial structures are predicted for $Pa_2(C_8H_8)_2$ and $Np_2(C_8H_8)_2$, while in $Th_2(C_8H_8)_2$ the C_8H_8 rings tilt away from the An-An axis. Further thermodynamic calculations suggest that it may be possible to generate these new complexes experimentally.

SB-3CT, (4-phenoxyphenylsulfonyl)methylthiirane, is a potent, mechanism-based inhibitor of the gelatinase sub-class of the matrix metalloproteinase (MMP) family of zinc proteases. The gelatinase MMPs are unusual in that there are several examples where both enantiomers of a racemic inhibitor have comparable inhibitory abilities. SB-3CT is one such example. The inhibition mechanism of the MMP2 gelatinase by the (*S*)-SB-3CT enantiomer and its oxirane analogue is examined computationally by QM/MM method, and compared to the mechanism of (*R*)-SB-3CT.

AUTOBIOGRAPHICAL STATEMENT

JIA ZHOU

EDUCATION

Wayne State University, Doctor of Philosophy in Chemistry, 2011. Thesis Topic: "Applications of Electronic Structure Theory to Problems in Unimolecular Dissociation and Inorganic and Biochemical Systems".

Fudan University, Master of Science in Physical Chemistry, 2006. Graduate Research Topics: "Density Functional Study on the Interaction of Silver Clusters with Dual-Atom Molecules".

Shanghai Jiao Tong University, Bachelor of Engineering in Applied Chemistry, 2003. Undergraduate Research Topic: "Measurement of Trace Element Cadmium Using Spectrophotometer by the Aid of Membrane Filter".

SELECTED PUBLICATIONS

1) Zhou, Jia; Schlegel, H. B. Dissociation of Acetone Radical Cation ($CH_3COCH_3^{+\cdot} \rightarrow CH_3CO^+ + CH_3^{\cdot}$): An *Ab Initio* Direct Classical Trajectory Study of the Energy Dependence of the Branching Ratio. The Journal of Physical Chemistry A (2008), 112(50), 13121–13127.
2) Zhou, Jia; Schlegel, H. B. Large Non-statistical Branching Ratio in the Dissociation of Pentane-2,4-dione Radical Cation: An *Ab Initio* Direct Classical Trajectory Study. The Journal of Physical Chemistry A (2009), 113(8), 1453–1458.
3) Zhou, Jia; Schlegel, H. B. *Ab Initio* Classical Trajectory Study of the Dissociation of Neutral and Positively Charged Methanimine (CH_2NH^{n+} n = 0-2). The Journal of Physical Chemistry A (2009), 113(37), 9958–9964.
4) Singh, P. C.; Shen, L.; Zhou, Jia; Schlegel, H. B.; Suits, A. G. Photodissociation Dynamics of Methylamine Cation and Its Relevance to Titan's Ionosphere. The Astrophysical Journal (2010), 710(1), 112-116.
5) Zhou, Jia; Schlegel, H. B. *Ab Initio* Molecular Dynamics Study of the Reaction between Th^+ and H_2O. The Journal of Physical Chemistry A (2010), 114(33), 8613–8617.
6) Zhou, Jia; Sonnenberg, J. L.; Schlegel, H. B. Theoretical Studies of $An^{II}_2(C_8H_8)_2$ (An = Th, Pa, U, and Np) Complexes: The Search for Double-stuffed Actinide Metallocenes. Inorganic Chemistry (2010), 49(14), 6545-6551.
7) Zhou, Jia; Tao, P.; Fisher, J. F.; Shi, Q. Mobashery, S.; Schlegel, H. B. QM/MM Studies of the Matrix Metalloproteinase 2 (MMP2) Inhibition Mechanism of (*S*)-SB-3CT and its Oxirane Analogue. Journal of Chemical Theory and Computation (2010), 6(11), 3580-3587. (Cover)